RECLAMATION

Managing Water in the West

Technical Memorandum TM-86-68330-2013-12

The M_L 4.4 Earthquake of January 24, 2013, Near Paradox, Colorado, and Implications for Near-term Injection Operations

Colorado Basin Salinity Control Project,
Paradox Valley Unit, Colorado
Upper Colorado Region

U.S. Department of the Interior
Bureau of Reclamation

May 2016

Mission Statements

The mission of the Department of the Interior is to protect and provide access to our Nation's natural and cultural heritage and honor our trust responsibilities to Indian Tribes and our commitments to island communities.

The mission of the Bureau of Reclamation is to manage, develop, and protect water and related resources in an environmentally and economically sound manner in the interest of the American public.

BUREAU OF RECLAMATION
Technical Service Center, Denver, Colorado
Seismotectonics and Geophysics Group, 86-68330

Technical Memorandum TM-86-68330-2013-12

The M_L 4.4 Earthquake of January 24, 2013, Near Paradox, Colorado, and Implications for Near-term Injection Operations

Colorado Basin Salinity Control Project,
Paradox Valley Unit, Colorado
Upper Colorado Region

Prepared by:

Christopher K. Wood, Geophysicist	5/26/16 Date
Lisa V. Block, Geophysicist	5/26/16 Date
Vanessa M. King, Geophysicist	5/26/16 Date
William L. Yeck, Geophysicist	5/15/15 Date

Peer Review Certification
This report has been reviewed and is believed to be in accordance with the service agreement and standards of the profession.

Peer reviewed by:

Pengcheng Liu, Geophysicist	5/26/2016 Date

Contents

Tables

Page

Figures

Page

Executive Summary

A widely-felt earthquake occurred in the northern Paradox Valley area on January 24, 2013, at 4:46:39 UTC time (January 23, 2013, at 9:46:39 pm local time). The earthquake had an estimated local magnitude of M_L 4.4. Using data from a local 20-station seismic network, we determined the epicenter was 8.2 km (5.1 mi) northwest of the Paradox Valley Unit (PVU) injection well and 5.6 km (3.5 mi) southwest of the town of Paradox, Colorado (Figure 1-1). The focal depth was found to be 4.4 km below local ground surface, which is equivalent to a depth of 4.1 km below the PVU injection wellhead.

Our analysis indicates that this earthquake was induced by long-term fluid injection into the PVU injection well. This event was slightly larger than the M_L 4.3 earthquake of May 27, 2000, making it the largest PVU-induced event to date. However, it was located nearly four times farther away from the injection well than any previous PVU-induced earthquake of comparable magnitude. The occurrence of a strongly-felt earthquake several kilometers from the injection well is cause for greater concern than for an earthquake of similar size, but located nearer to the well. That is because the triggering mechanisms for events occurring far from the well are poorly understood, the time required to affect seismicity changes in this area by varying injection operations is potentially long (e.g., several years), and the effectiveness of changes in injection operations to reduce the seismic hazard from induced earthquakes at these distances may not be apparent for several years.

Many local residents experienced strong ground shaking partly because the January 24th, 2013 earthquake occurred much closer to northern Paradox Valley than previous $M \geq 3.5$ induced earthquakes. At the town of Paradox, a Reclamation strong motion instrument recorded a peak horizontal acceleration of 0.29 g. Even accounting for the close distance to the January earthquake, ground motions were unusually large. For frequencies above 2.5 Hz, the horizontal accelerations recorded in the town of Paradox were nearly two standard deviations higher than the mean value estimated by standard ground motion prediction equations for an earthquake of this magnitude and distance.

This technical memorandum (TM) presents an analysis of the January 24th, 2013 earthquake, its relation to previously-induced seismicity, and an evaluation of the ground shaking that it produced (Section 2). Factors that influence the seismic risk associated with deep-well injection at PVU are then reviewed (Section 3). Results from analysis of PVU injection pressure-flow data, and suggestions for operational changes in injection operations are presented (Section 4). Discussion and conclusions are presented in Sections 5 and 6.

Results presented in this TM are primarily from analyses in progress before the January 24, 3013 earthquake, or that were done in the weeks immediately following it. The purpose of these analyses was to fulfill requirements of the Emergency Action Plan for operation of the PVU injection well, and to develop alternatives for operations to minimize the potential for additional felt earthquakes. Hence, this TM mostly contains analyses that could be completed quickly after the earthquake. Following completion of the initial draft of this report in April, 2013, more detailed analyses were conducted and submitted for publication in peer-reviewed scientific journals (Block and others, 2014; King and others, 2014; Yeck and others, 2014; Block and others, 2015), and results have been incorporated into the current draft of this TM where appropriate. Detailed analysis of a few remaining topics are in progress, including pressure-flow modeling and seismic hazard analysis, and are expected to be documented in peer-reviewed journal articles.

1 Introduction

An M_L 4.4 earthquake occurred in the Paradox Valley area on January 24, 2013, at 4:46:39 UTC time (January 23, 2013, at 9:46:39 pm local time). The earthquake occurred near the northwest end of the valley (Figure 1-1), and was felt strongly by local residents.

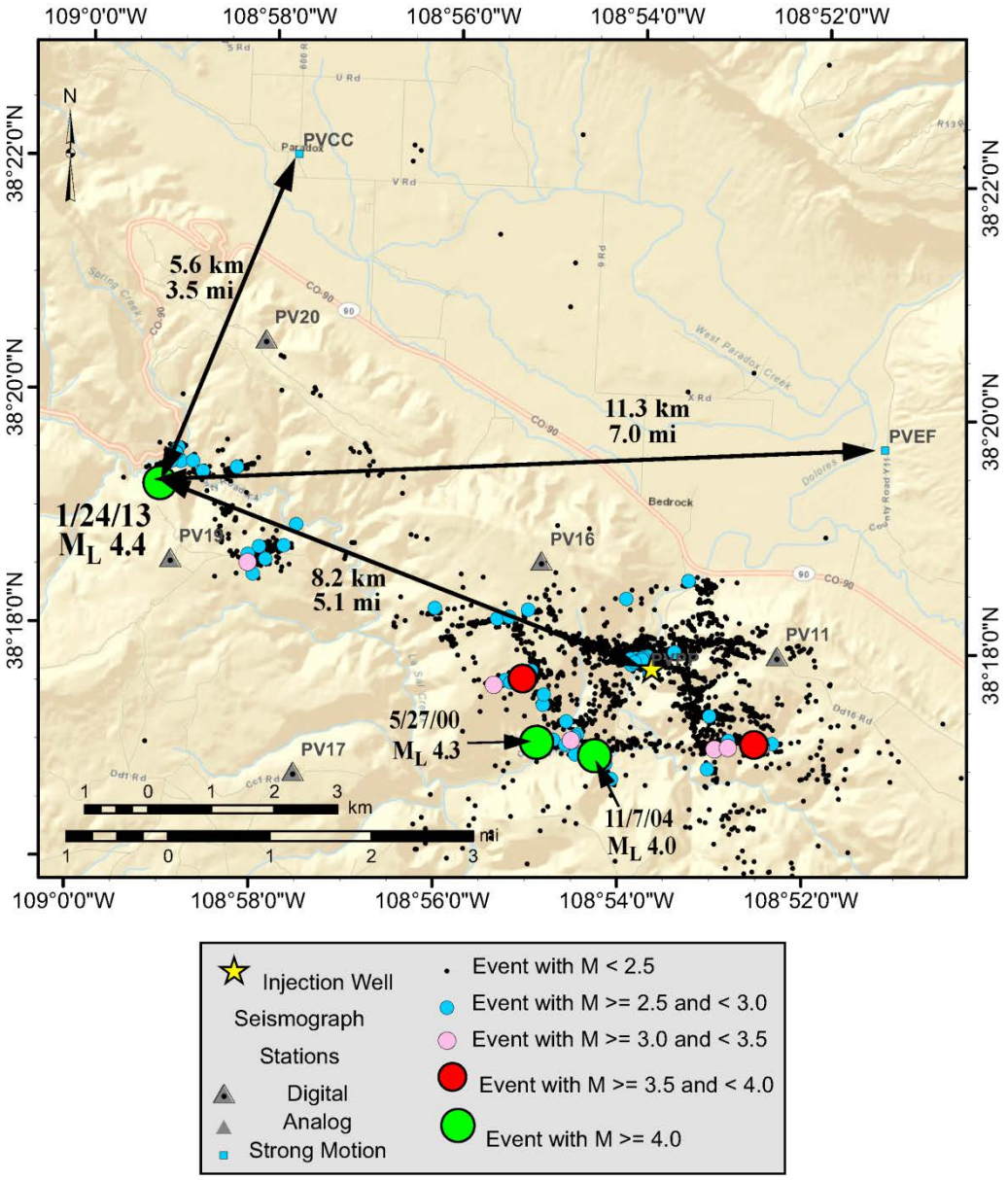

Figure 1-1. Location of the Jan. 24, 2013 M_L 4.4 earthquake relative to the Paradox Valley Unit (PVU) injection well (yellow star), PVU extraction well field (PVEF), and the town of Paradox, Colorado (PVCC).

Available data indicate that this earthquake was induced by fluid injection at the Bureau of Reclamation's (Reclamation) Paradox Valley Unit (PVU) brine disposal well. The earthquake epicenter is within the previously-identified northwest (NW) cluster of induced seismicity, a persistent zone of induced earthquakes 6 to 8 km northwest of the injection well (Figure 1-1). The NW cluster has been seismically active since mid-1997, approximately 1 year after the start of continuous fluid injection (July, 1996). The January 24th earthquake occurred 4.4 km below the local ground surface (4.1 km below the elevation of the injection wellhead), consistent with depths of previously-induced events and with the depths of injection target formations (Figure 1-2). Natural earthquakes in the region tend to occur substantially deeper.

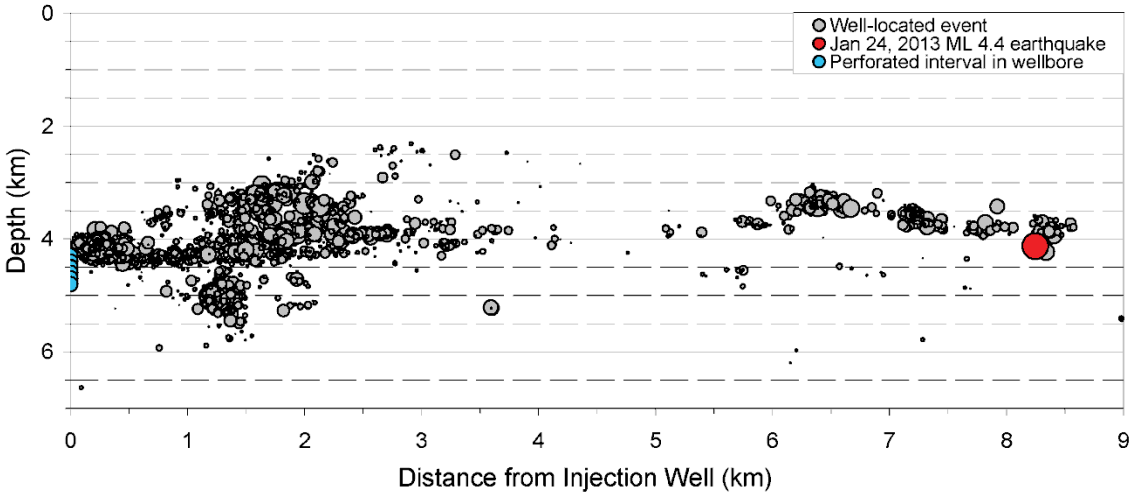

Figure 1-2. PVU-induced earthquakes having well-constrained relative hypocenters, plotted as a function of distance from the PVU injection well and depth (relative to the ground surface elevation at the wellhead). Each circle represents a single earthquake, with the width of the circle scaled by the event magnitude. The January 2013 earthquake is shown in red, and the perforated interval in the injection well (4.3 to 4.8 km depth) is indicated by the blue circles on the left side of the graph.

Since 1996, Reclamation has been disposing of brine in a deep injection well located just southwest of Paradox Valley, Colorado, as part of the PVU salinity control project. This period of continuous injection was preceded by a series of injection tests conducted between 1991 and 1995. The PVU injection well disposes of brine that would otherwise enter the Dolores River, a tributary of the Colorado River. This project is authorized by the Colorado River Basin Salinity Control Act, passed by the U.S. Congress in 1974, and is an important component of the Colorado River Basin Salinity Control Program (CRBSCP), an effort to improve water quality in the Colorado River system. Further information on the Paradox Valley Unit can be found in Block and others (2012) or at the Reclamation project website (see http://www.usbr.gov/projects, under CRBSCP, Paradox Valley Unit - Title II).

Six years of pre-injection monitoring recorded no seismicity within 18 km of the injection well. The data recorded during this period include just 1 local earthquake, which occurred almost 19 km from the PVU injection well. Within days of the start of the initial injection test in 1991, seismic events were detected in the immediate vicinity of the injection well. During subsequent injection tests and continuous injection operations, induced earthquakes occurred at increasing distances from the injection well. The close correlation between injection operations and induced seismicity at PVU has been well established, as is illustrated by Figure 1-3.

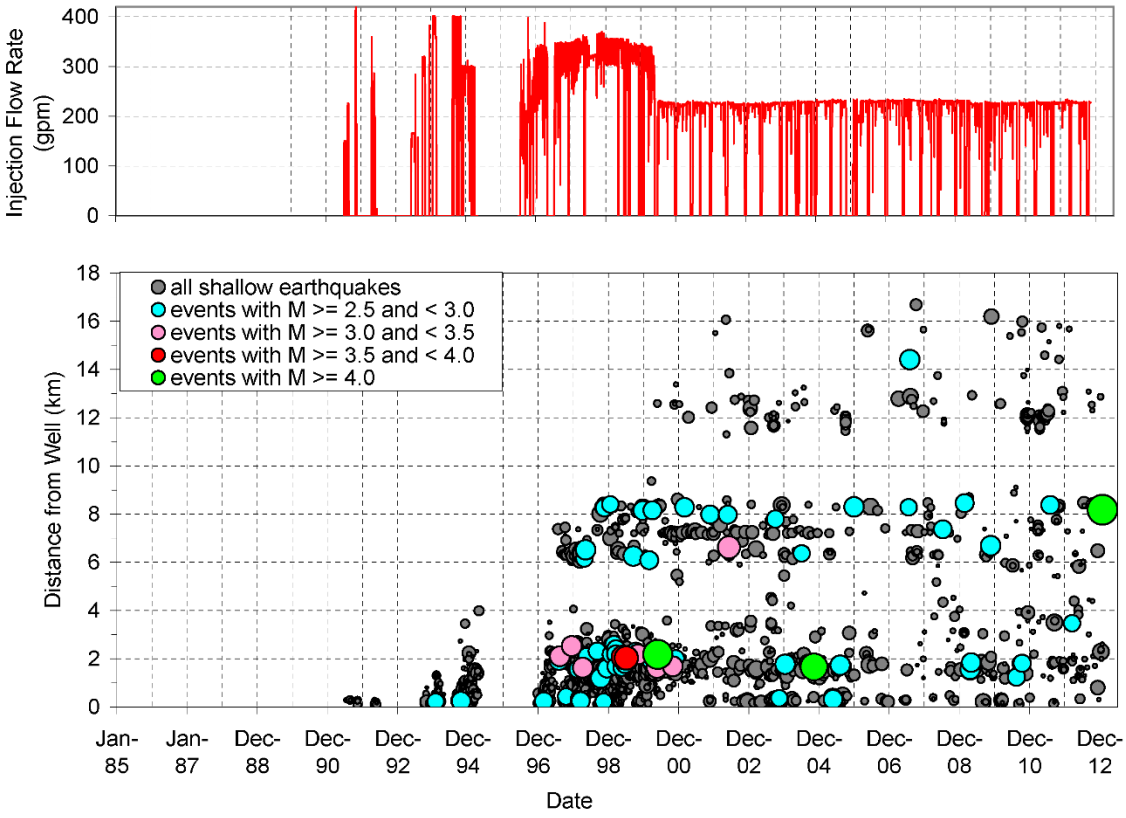

Figure 1-3. Correlation between injection flow rates and shallow seismicity (< 8.5 km depth) recorded by the Paradox Valley Seismic Network (PVSN). The network has been continuously operational since 1985, 6 years prior to injection, and no seismicity was observed within 18 km of the well prior to injection. The large green dot on the right side of the figure represents the January 24, 2013 earthquake. It is located within a group of induced earthquakes identified as the northwest (NW) cluster.

Microseismic monitoring of the Paradox Valley area began in 1983, with installation of the first stations of the Paradox Valley Seismic Network (PVSN). Network installation was timed to provide a pre-injection baseline of naturally-occurring background seismicity, and stations were located to optimize monitoring of any earthquakes that might be induced in the vicinity of the well. The network has been continuously operated since 1985, and has been expanded and updated over the years to respond to changing seismicity patterns. The current

configuration consists of a surface array of 20 digitally-recorded broad-band, 3-component sensors. A map showing the locations of the stations is shown in Figure 1-4. The January 24th earthquake was recorded by the broad-band network, as well as by 3 digital strong motion instruments operated by Reclamation and located at the Paradox Community Center (PVCC), the PVU injection well-head and pumping plant (PVPP), and the PVU extraction field and surface treatment facility (PVEF).

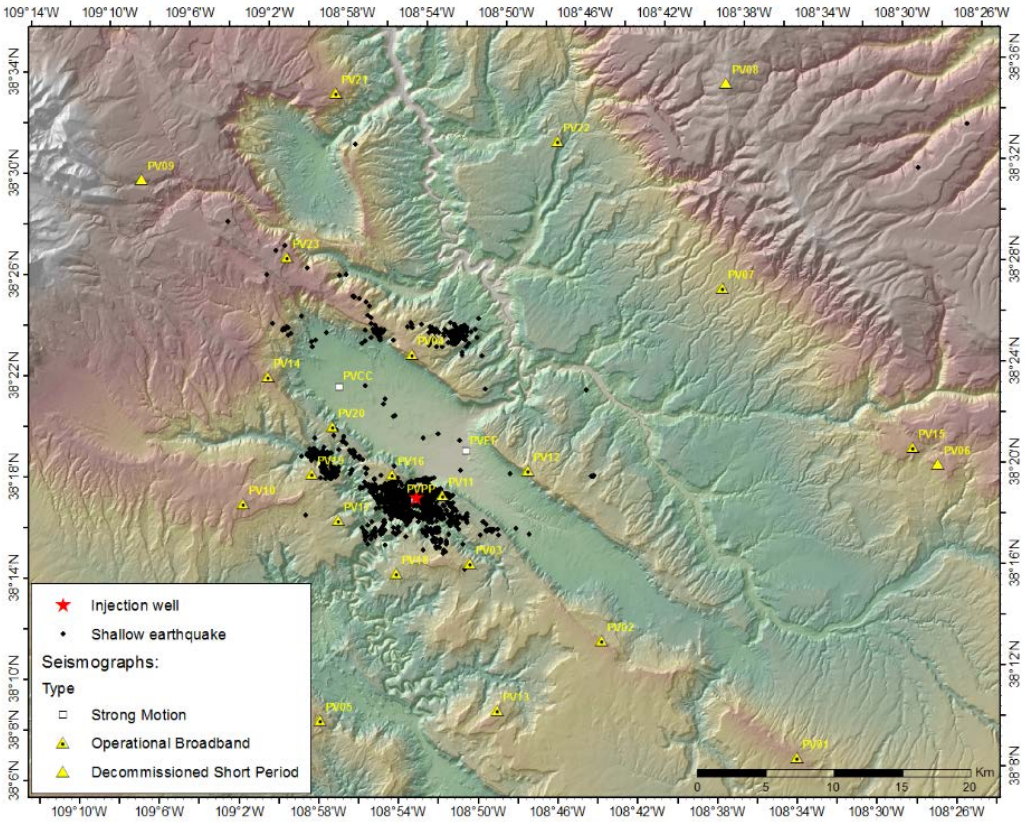

Figure 1-4. Location of Paradox Valley seismograph stations.

2 Description of the Earthquake

2.1 Earthquake Magnitude

We calculated a moment magnitude of M_W 4.0 for the January 24th earthquake, using only PVSN broad-band data. Seismic moment, and hence moment magnitude, were estimated from the long-period displacement spectra at all PVSN stations having good-quality data (Figure 2-1). An ω^2 spectral model is assumed {Brune, 1970 #2}, including correction for high-frequency attenuation {Anderson, 1984 #110}, and model parameters are estimated from the spectra using standard methods {Andrews, 1986 #111;Boore, 1986 #112;De Natale, 1987 #113;Snoke, 1987 #114;Hough, 1988 #115;Anderson, 1991 #116;Shearer, 2006 #117;Kilb, 2012 #118}. Although the seismic waveforms from the PVSN stations closest to the epicenter were clipped, and therefore not usable in this analysis, useful data were obtained from 13 of the more distant stations. Assuming a simple Brune (1970, 1971) circular rupture model, we also determined a static stress drop of 20 bars and rupture radius of 0.6 km. The moment magnitude we computed is consistent with magnitudes computed by the United States Geological Survey's (USGS) National Earthquake Information Center using data from regional seismic stations and a variety of magnitude scales, which include: moment magnitude, M_W, 3.9, local magnitude, M_L, 4.4, and body wave magnitude, m_b 3.8 (Harley Benz, personal communication). These magnitude scales are described at the end of this section.

Because earthquakes previously induced by PVU fluid injection with magnitude of 3.5 or greater have been reported using the local magnitude scale, M_L, for consistency we use the M_L of January 24th earthquake when comparing the size of this event to the historical PVSN seismicity data. The previous largest PVU-induced earthquake was the M_L 4.3 earthquake of May 27, 2000. The January 24, 2013 earthquake, with M_L 4.4, is slightly larger than the May 2000 event, making it the largest PVU-induced earthquake to date. A comparison of the local and moment magnitudes of the 3 largest PVU-induced earthquakes recorded to date is provided in Table 2-1.

Table 2-1. Comparison of local and moment magnitudes for the 3 largest PVU-induced earthquakes. The source for each magnitude estimate is given in parentheses: UUSS = University of Utah Seismograph Stations; SLU = Saint Louis University; USGS = U. S. Geological Survey; USBR = Bureau of Reclamation.

Earthquake Date (UTC)	Local Magnitude (M_L)	Moment Magnitude (M_W)
5/27/2000	4.3 (UUSS)	3.8 (SLU)
11/7/2004	4.0 (USGS)	3.6 (SLU)
1/24/2013	4.4 (USGS)	4.0 (USBR) 3.9 (USGS)

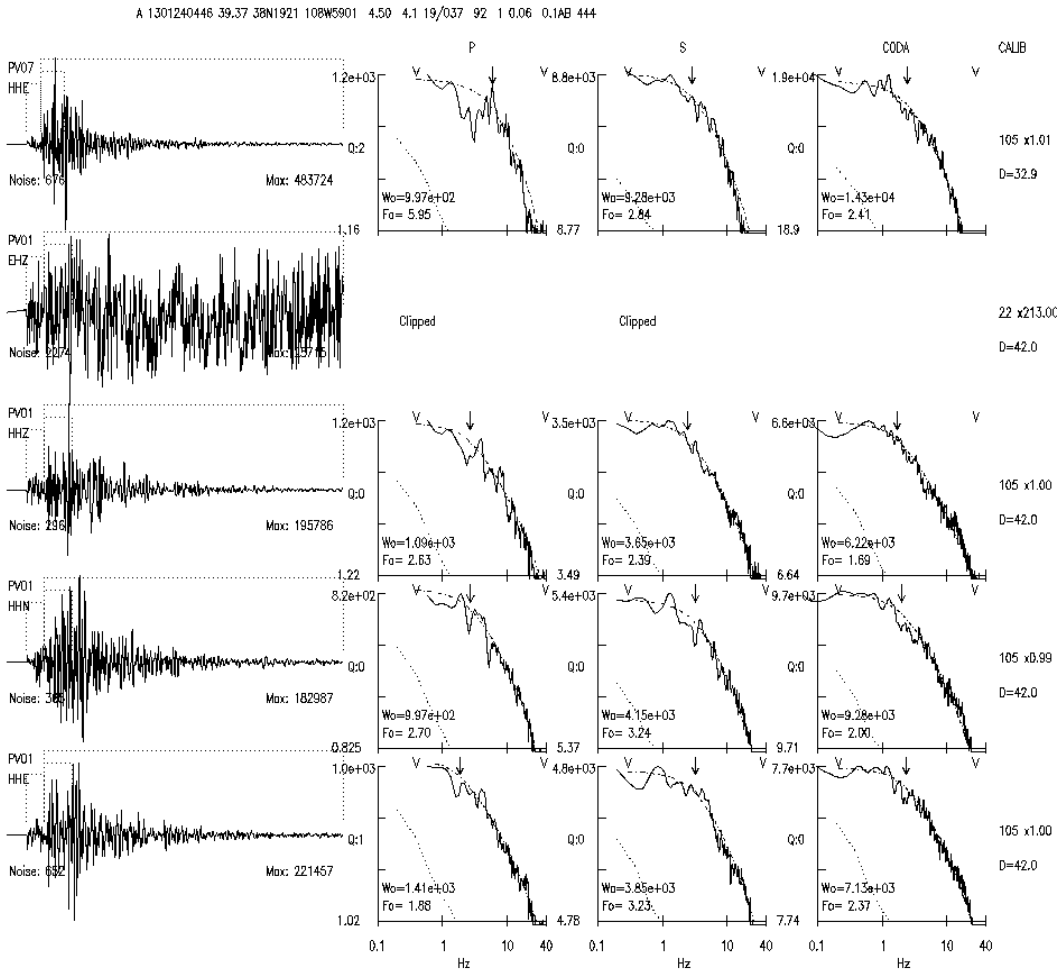

Figure 2-1. Example of automatic spectral fitting procedure used to estimate seismic moment (see text), showing selected displacement amplitude spectra for P, S, and S-wave coda at station PV01 (42 km distance) and PV07 (33 km distance). Dotted lines indicate pre-event noise, and dashed lines indicate the modeled fit to the spectra. Arrows on each spectrum indicate the fitted corner frequencies. Carat symbols indicate the limits of the frequency bands used for fitting the spectra. The spectra are also corrected for a site attenuation parameter kappa {Anderson, 1984 #110}, which ranges in value from 0.01 to 0.05. The procedure automatically rejects clipped or otherwise bad data, as is demonstrated by the second trace from the top.

2.1.1 Magnitude Scales

Multiple magnitude scales are used to quantify the size of earthquakes. Each measures different characteristics of the seismic waveforms, which can result in different numerical values between the scales and inconsistencies between different regions (Chung and Bernreuter, 1981). The *duration* magnitude scale (M_D), which uses the logarithm of the duration of the seismic signals, is commonly used for computing magnitudes of local earthquakes recorded by microearthquake networks because it is easy to apply and provides consistent results (e.g., Lee and Stewart, 1981). Duration magnitudes work well for the majority of the induced seismic earthquakes recorded by the Paradox Valley Seismic Network (PVSN) because they are small to moderate in size. Although the duration magnitude scale generally provides consistent results between earthquakes within a given network, it has certain drawbacks: (1) it may not be calibrated well between networks, especially for smaller-magnitude events; and, (2) the duration magnitude scale may saturate for larger earthquakes (M>3) recorded by PVSN due to truncation of long-duration records. Hence, other scales must be used to compare the largest PVU-induced events. The *local* magnitude scale (Richter, 1935), based on computing the logarithm of the peak amplitude of the seismic signal (corrected for a standard distance and instrumentation type), has been reported for some larger PVU events by the USGS and the University of Utah Seismograph Stations (UUSS). Other magnitude scales occasionally reported by USGS include the *surface-wave* (M_S) and *body-wav*e (m_b) magnitudes. As seismic instrumentation has improved in recent years, use of the *moment* magnitude scale (M or M_W) (Hanks and Kanamori, 1979) has become more common.

2.2 Location

We computed a hypocenter for the January 2013 earthquake using P- and S-wave arrival times from PVSN and a local 3-dimensional (3-D) velocity model we had developed previously. The earthquake epicenter is at latitude 38.32087 deg. N, longitude 108.98408 deg. W, which is 8.2 km (5.1 mi) northwest of the PVU injection well and 5.6 km (3.5 mi) southwest of the town of Paradox, Colorado (Figure 1-1). The focal depth is 4.4 km below local ground surface, which is equivalent to a depth of 4.1 km below the PVU injection wellhead.

The January 24, 2013 event is the only induced earthquake with M_L 3.5 or greater (M_L 3.5+) to occur at a radial distance greater than about 2 km from the injection well (Figure 2-2). The previous four PVU-induced M_L 3.5+ events occurred in a narrow band between 1.6 and 2.2 km from the injection well (Figure 2-2). At a distance of 8.2 km from the injection well, the January earthquake epicenter is nearly four times farther from the well than that of any other PVU-induced earthquake of comparable magnitude. In addition, the January 24th earthquake is only the second earthquake with duration magnitude of M_D 3.0 or greater to occur more than ~2 km from the injection well. The only other M_D 3.0+ earthquake at a

relatively large radial distance is an M_D 3.3 event that occurred within the NW cluster in June, 2002, about 6.6 km from the well (Figure 2-2).

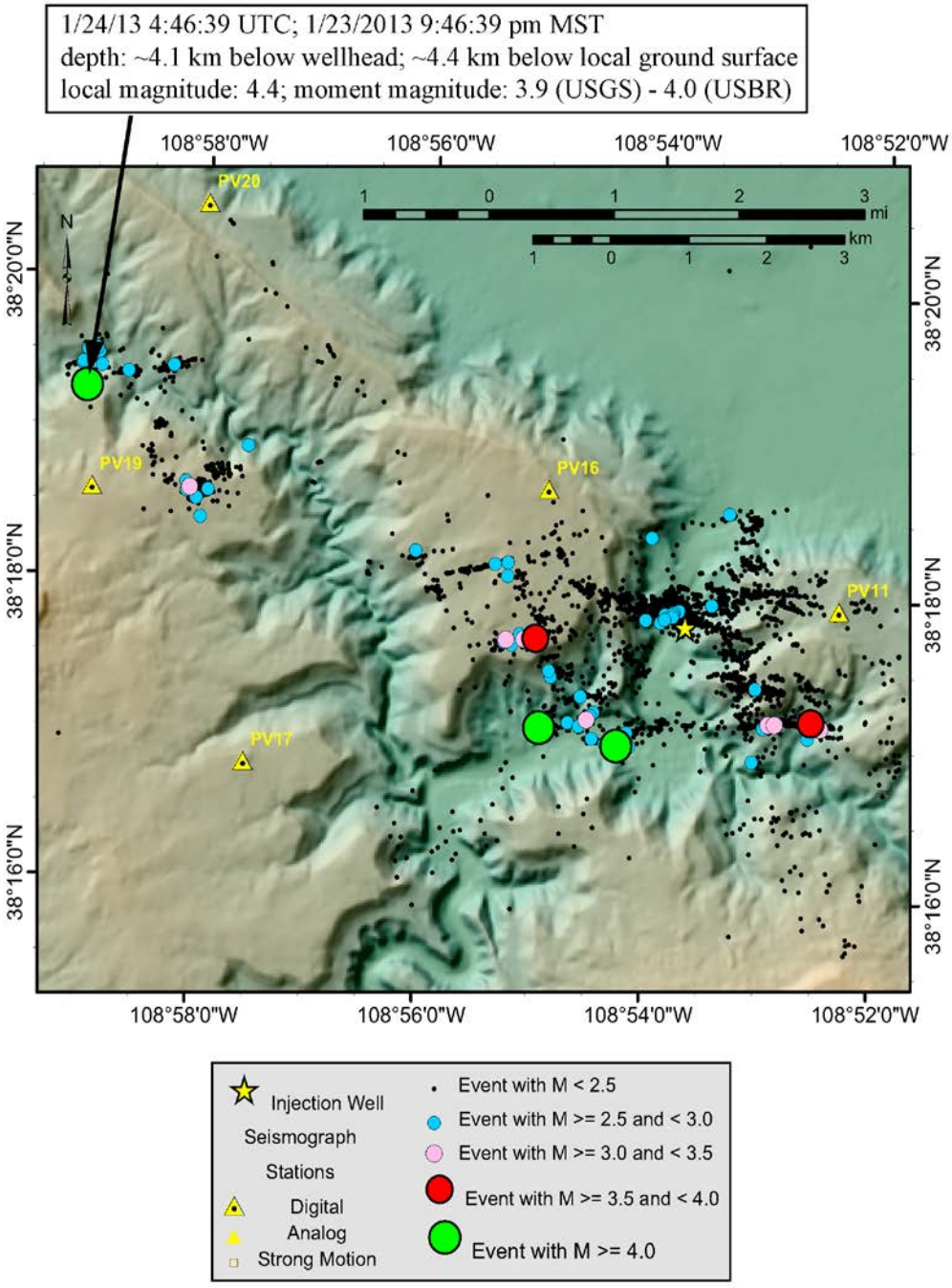

Figure 2-2. Location of PVU-induced seismicity in the near-well region (within 5 km of the injection well) and northwest cluster (6 to 8 km from the well).

2.3 Focal Mechanism

First-motion data from PVSN stations indicate that the earthquake was produced by strike-slip faulting on either of two conjugate steeply-dipping fault planes: (1) a fault striking N13°W, and dipping 79° ENE, or (2) a fault striking N78°E, and dipping 84° SSE. The directions of compression (P-axis) and extension (T-axis) are N58°W and N32°E, respectively. The strike-slip mechanism is consistent with the previous finding of Ake and others (2005), who found that strike-slip mechanisms accounted for 89% of 1345 well-determined mechanisms and determined a mean P-axis of N64°W-N67°W.

First-motion data alone do not determine which conjugate plane is the true fault plane. However, precise relative locations of earthquakes in the vicinity of the January 24th event show a 1.5-km-long lineation oriented approximately N78ºE, consistent with the ENE-striking conjugate plane. Several aftershocks of the January 24th earthquake also occurred along this lineation (Figure 2-3). Hence, the earthquake locations suggest that the second conjugate fault orientation, N 78ºE, is the rupture plane of the January 24th earthquake.

The January 24th earthquake did not occur on any of the deep faults that were mapped during previous PVU geophysical investigations. Most of the faults mapped during these early studies trend northwest (~N55°W), approximately parallel to Paradox Valley (Block and others, 2012). Because this orientation is close to the estimated direction of maximum horizontal stress (Ake and others, 2005), the major basement faults are not optimally oriented for shear slip. The majority of the induced earthquakes observed at PVU occur on unmapped, previously aseismic faults. Because these faults may not have much net vertical offset, they may be difficult to resolve on deep seismic reflection data.

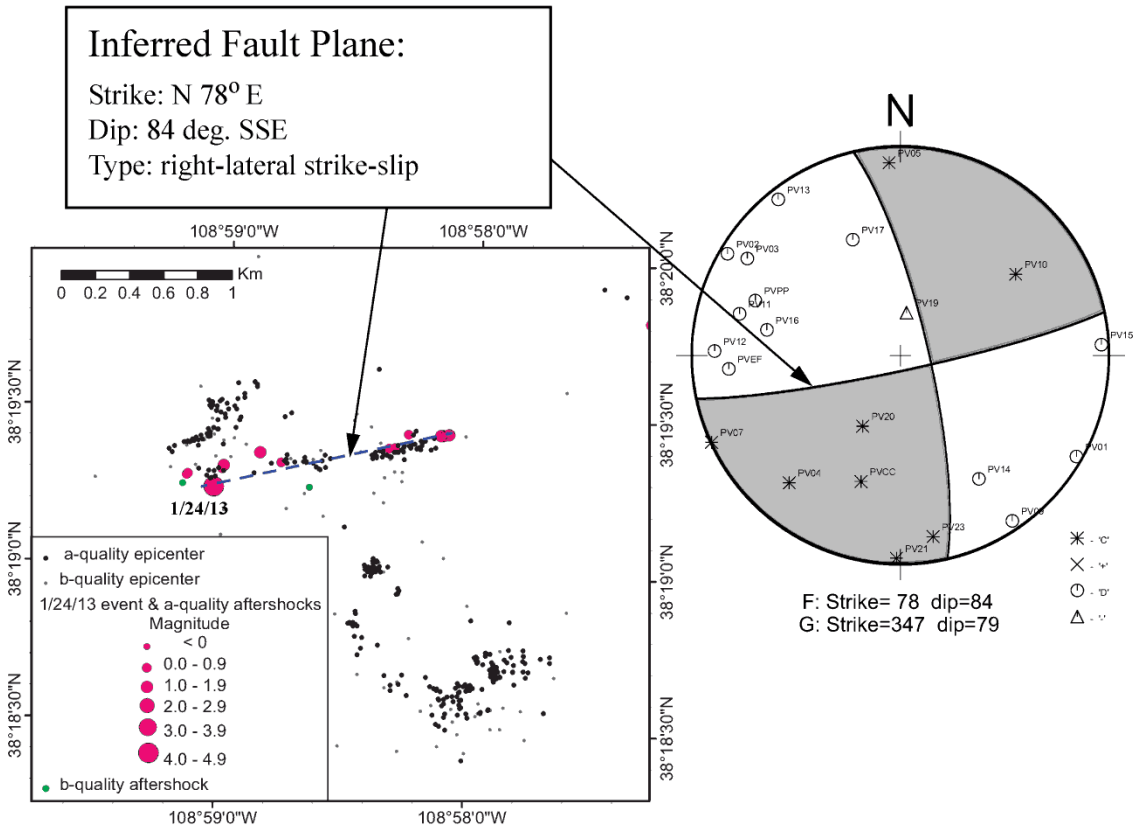

Figure 2-3. First motions and computed focal mechanism of the January 2013 event, and map showing the distribution of previously induced earthquakes in the vicinity of the January 2013 event (a-quality epicenters: black dots; b-quality epicenters: gray dots) and the locations of the January 2013 earthquake and aftershocks observed through July 2013 (a-quality epicenters: magenta circles; b-quality epicenters: green circles). Except for the main event, the a-quality epicenters were determined using a relative location routine and precise time differences from waveform cross-correlations. The main event was tied into the relative location using time differences from high-quality manual arrival time picks. The b-quality epicenters were computed using manual arrival time picks and a local 3-D velocity model.

2.4 Nearby Seismicity

In the 6 months prior to the January 2013 event, PVSN recorded about 30 induced seismic events within 1 km of the mainshock epicenter (Figure 2-4). These foreshocks had duration magnitudes less than M_D 2.0, with most having $M_D \leq 1.0$. We did not observe any increase in maximum event magnitude or any substantial change in the rate of $M_D \geq 0.5$ events in the weeks or months prior to the January 2013 earthquake. In contrast, a large increase in the rate of detected events with magnitude M_D 0.0 to 0.5 occurred during the third quarter of 2012, with 5 times more M_D 0.0-0.5 events recorded during this 3-month period than in any previous

quarter (Figure 2-5). However, the baseline period to determine seismicity rates of M_D 0.0 to 0.5 events was only about a year and a half at the time of the January 2013 event, because events this small were not reliably detected in this area until after the installation of two additional nearby seismic stations in July, 2011. Rates of M_D 0.0 to 0.5 events returned to normal levels during the fourth quarter of 2012. Hence, we have limited data to indicate whether the observed increased rate of M_D 0.0 to 0.5 events a few months prior to the January 2013 earthquake is anomalous.

We found that earthquakes in the vicinity of the January 2013 event can be grouped into two distinct faulting types, based on an analysis of 35 events with well-constrained relative hypocenters: (1) strike-slip faulting consistent with that of the January 2013 earthquake (average mechanism from 20 events is N76°E, dip 76°SSE; standard deviations of strike and dip are about 5°), and (2) an oblique normal focal mechanism (average mechanism from 15 events is (a) strike N42°W, dip 71°WSW, or (b) strike N77°E, dip 35° NNW, with standard deviations of strike and dip less than 7°). Epicenters of these earthquakes are plotted by focal mechanism type in Figure 2-6a. All analyzed events with strike-slip mechanisms are distributed along the inferred east-northeast trending fault segment interpreted to have ruptured during the January 2013 earthquake. Events with the oblique-normal focal mechanism form a tightly-spaced cluster about 250 to 450 meters (m) north of the strike-slip fault plane. Most of the foreshocks detected in the 6 months prior to the January 2013 earthquake occurred near this cluster, and relatively few foreshocks occurred near the interpreted mainshock fault plane (Figure 2-6a, squares and octagons). However, because of their small magnitude, most of these foreshocks do not have a sufficient number of clear first-motions to compute robust focal mechanisms.

The area surrounding the inferred rupture of the January 2013 earthquake has been seismically active since at least June 1997, about 1 year after the start of continuous PVU fluid injection, when PVSN recorded a cluster of earthquakes near the eastern end of the fault segment (Figure 2-6b). In October 1998, an earthquake was first detected near the center of the fault segment, approximately 500 to 700 m west of the initial cluster of events. By August 1999, seismicity was occurring near the western end of the fault segment, to within 100 m of the January 2013 event epicenter (Figure 2-6b). The seismicity pattern delineating the western end of the fault segment has not grown in size since 2000, suggesting that the segment is truncated in this direction, either by a major northwest-trending normal fault or by pinch-out of the primary injection target formation due to erosion (Block and others, 2012); (King and others). The seismicity pattern delineating the eastern limit of the fault segment has continued to expand slowly, and several aftershocks of the January 2013 event have extended seismicity on the fault segment to the east by about 100 m.

The entire fault segment, as inferred from pre-2013 seismicity, appears to have ruptured during the January 2013 earthquake. Aftershocks of the January 2013

earthquake occur near both ends of the pre-2013 seismicity zone (Figure 2-4 and Figure 2-6), and the inferred fault segment length determined from the seismicity distribution is consistent with the rupture dimension expected for the moment magnitude of the January 2013 earthquake, as will be discussed in Section 3.3.1.

Although small earthquakes have occurred since 1999-2000 along most of the fault segment that ruptured in January 2013, there was a 13-year delay before the occurrence of an earthquake which finally ruptured the entire segment. Only two earlier earthquakes of $M_D \geq 2.5$ occurred on portions of this fault segment: an M_D 2.6 event occurred near the center of the fault segment in October 2003, and an M_D 2.7 event occurred near the east end of the fault segment in July 2008 (Figure 2-6b). Assuming a similar stress drop as for the January 2013 earthquake (~20 bars), and a circular crack model, these earthquakes each ruptured less than a 300-m portion of the fault segment, or less than about 20% of the total fault segment length. One possible explanation for the 13-year delay prior to rupture of the entire fault segment is that a pore pressure threshold must be exceeded over most of the fault surface in order for rupture to propagate. We have previously observed that a pore pressure threshold may need to be reached to induce larger-magnitude earthquakes in the near-well region, based on correlation of near-well larger-magnitude earthquakes and higher injection pressures (Block and Wood, 2009; 2010). Correlation between larger-magnitude induced earthquakes and an increase in pore pressure to a threshold level over most of the fault surface has also been suggested by numerical studies (Garagash and Germanovich, 2012).

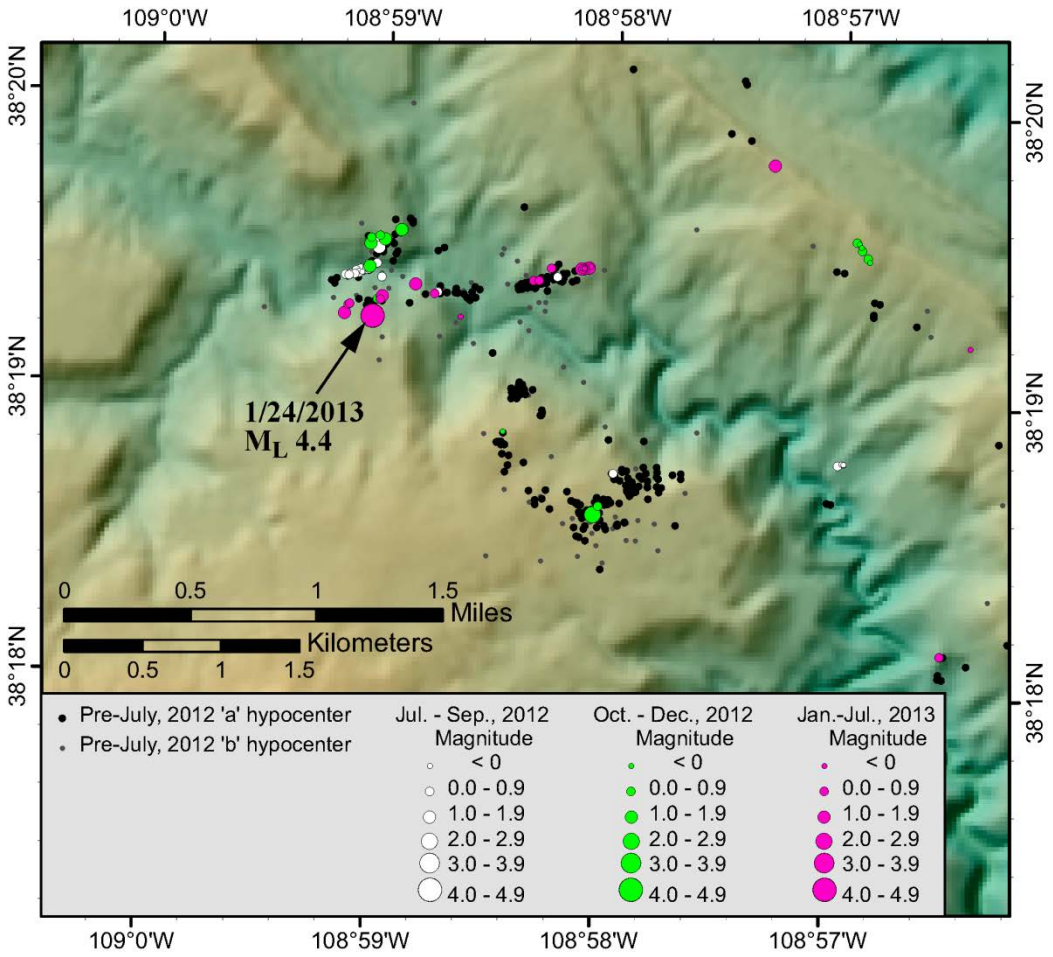

Figure 2-4. Map showing the distribution of foreshocks and aftershocks of the Jan. 24, 2013 event. The a-quality hypocenters were determined by a high-precision relative event location technique; the b-quality events did not have sufficient data to be included in the relative location and therefore have less precise locations. The July, 2012 through July, 2013 events are color-coded by month of occurrence and include both a- and b-quality hypocenters.

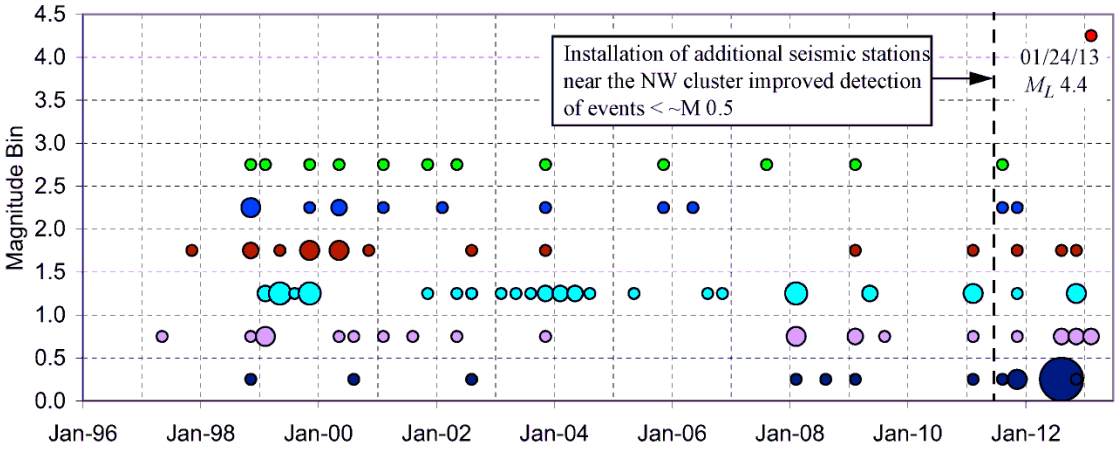

Figure 2-5. Occurrence of earthquakes within 1.0 km of the January 24, 2013 event epicenter, plotted as a function of date and earthquake magnitude. The area of each circle in scaled by the number of events recorded in a given quarter-year and magnitude range.

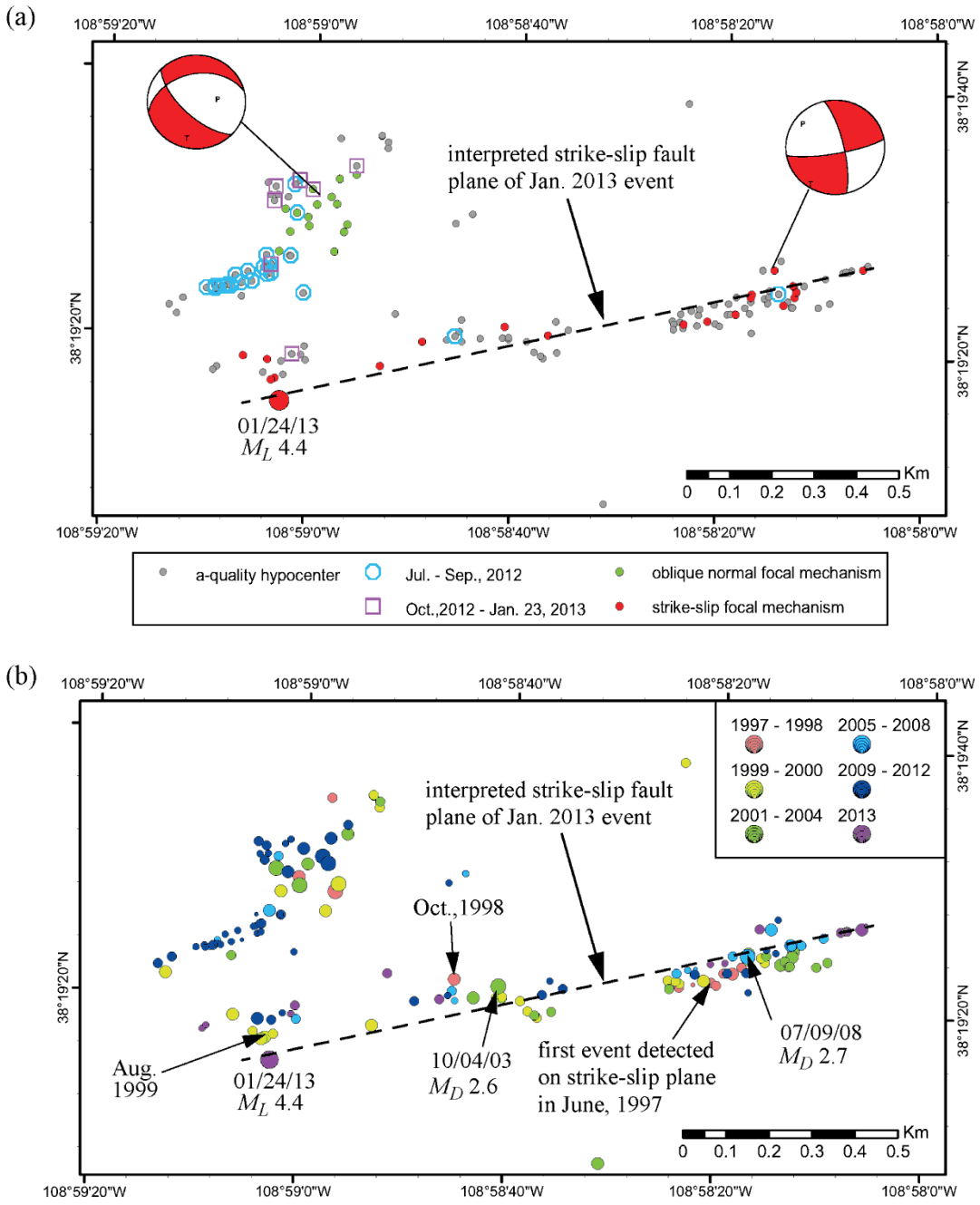

Figure 2-6. Epicenters of earthquakes with well-constrained relative locations in the near vicinity of the January 2013 M_L 4.4 earthquake. (a) Earthquakes having similar strike-slip focal mechanisms are indicated by the filled red circles, and those having similar oblique normal focal mechanisms are indicated by the filled green circles. A typical focal sphere plot for each type of mechanism is shown. Gray circles indicate events that lack well-defined focal mechanisms. Earthquakes occurring during the 6-month period before the January 2013 event are identified by the open squares and octagons, as indicated in the legend. (b) Earthquakes color-coded by year of occurrence and with symbol size scaled by event magnitude.

2.5 Strong Ground Motions

Strong-motion records were obtained from the Paradox Community Center (station code PVCC), the PVU injection wellhead and pumping plant (station code PVPP), and from the surface treatment facility and extraction well field (station code PVEF). The acceleration time histories are shown in Figure 2-7 (PVCC), Figure 2-8 (PVPP), and Figure 2-9 (PVEF), and a summary of the observed peak ground motions is provided in Table 2-2. Acceleration and velocity response spectra were also computed for each component of motion at each station, and these are shown in Figure 2-10 through Figure 2-15.

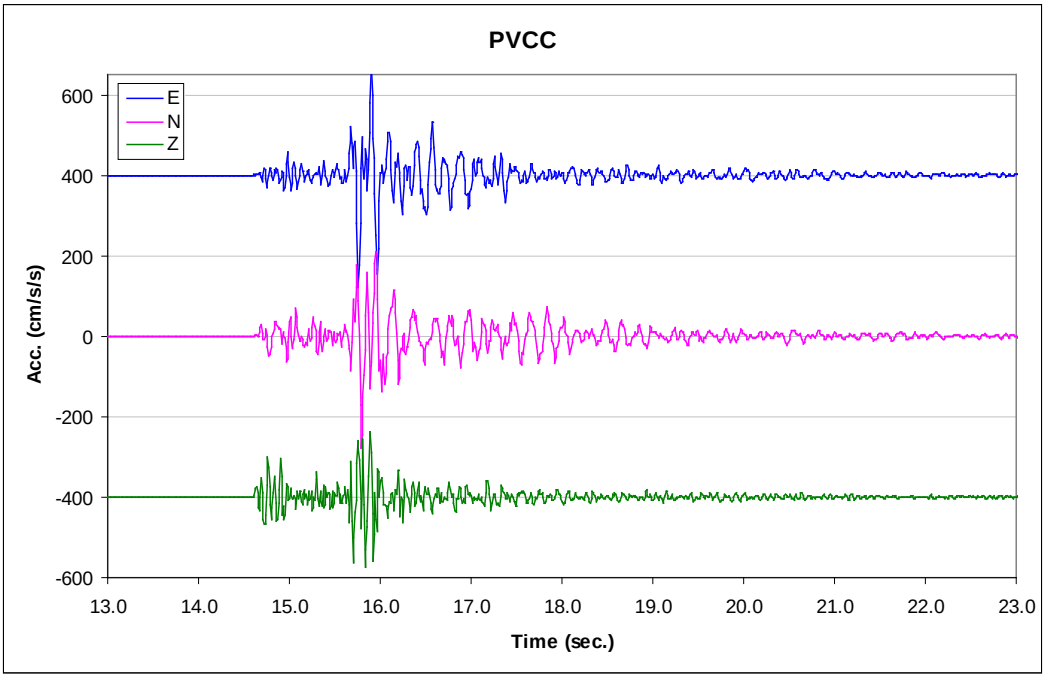

Figure 2-7. Acceleration ground motion time histories recorded by strong-motion instruments located at the community center in the town of Paradox, Colorado (PVCC). Traces are offset for clarity. Recorded peak horizontal acceleration (PHA) at PVCC was 0.28 g.

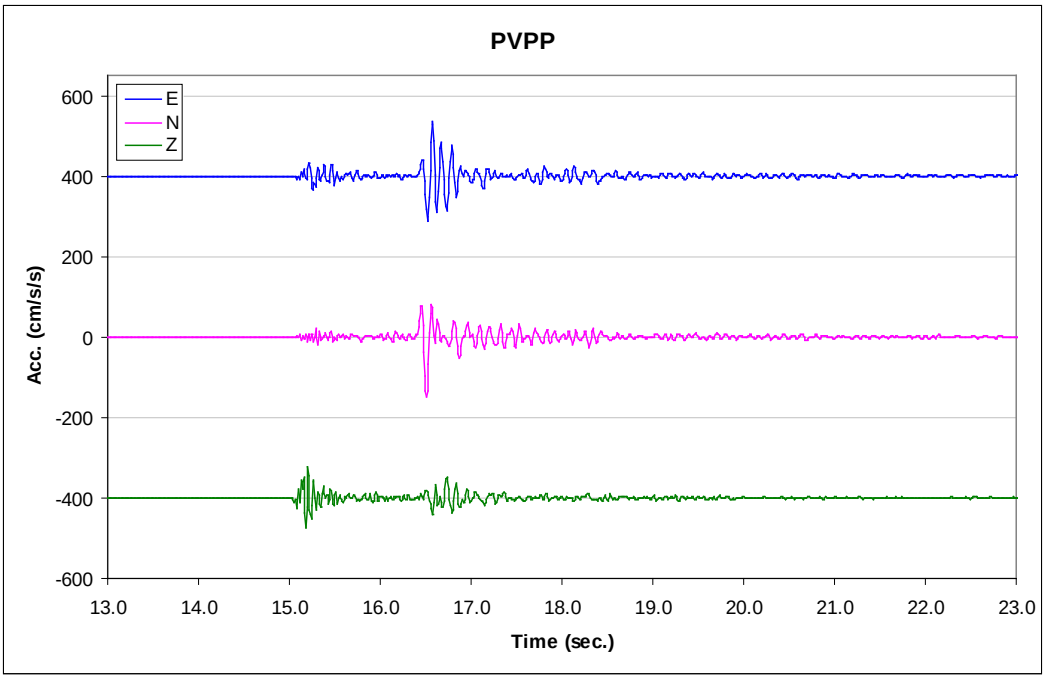

Figure 2-8. Acceleration ground motion time histories recorded by strong-motion instruments located near the PVU injection well and pumping plant (PVPP). Traces are offset for clarity. Recorded peak horizontal acceleration (PHA) at PVPP was 0.15 g.

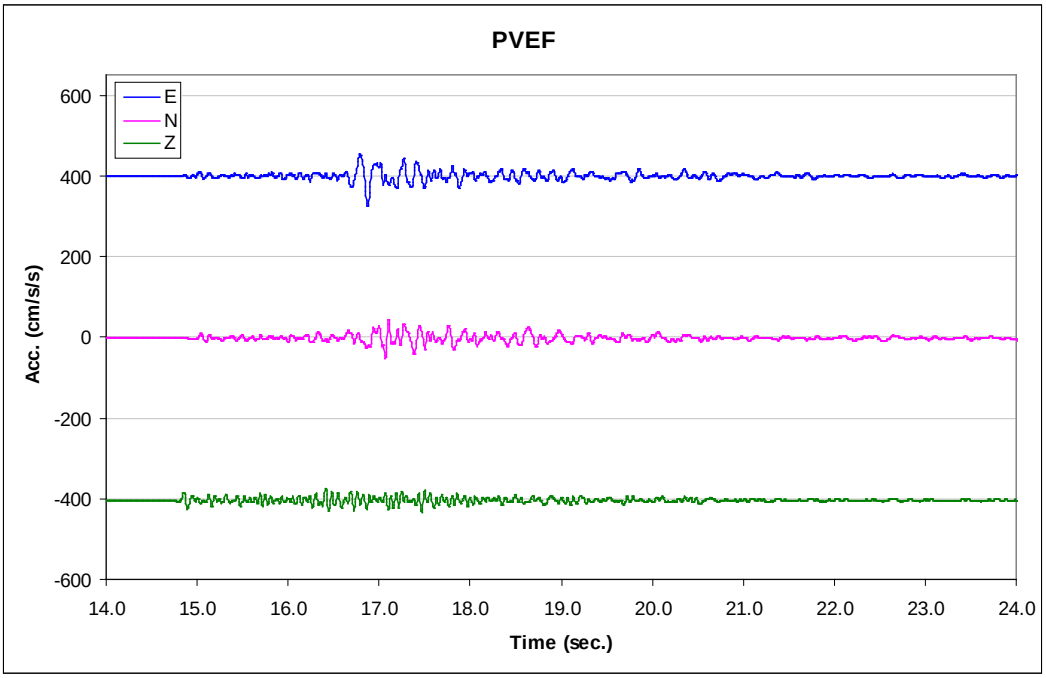

Figure 2-9: Acceleration ground motions recorded by strong-motion instruments located at the PVU surface treatment facility and extraction-well field (PVEF). Traces are offset for clarity. Recorded peak horizontal acceleration (PHA) at PVEF was 0.08 g.

Table 2-2. Observed ground motions and distances for the Paradox Community Center (PVCC), the injection well (PVPP), and the surface treatment facility (PVEF).

Site	Distance from Epicenter (km)	PHA (g)	1.0-sec. SA (g)	PHV (cm/s)
PVCC	5.6	0.293	0.011	6.1
PVPP	8.2	0.153	0.006	3.5
PVEF	11.3	0.077	0.006	2.0

Strong-motion instruments are designed to make on-scale recordings of strong ground shaking, and were installed in the Paradox Valley area to evaluate the likely engineering effects of shaking on structures. In contrast, the 20-station PVSN is designed to detect the weak motions from small earthquakes, and the high-gain instrumentation tends to saturate for large earthquakes. The strong motion instruments are 24-bit Kinemetrics model K2 data loggers, with either internal Episensor or external FBA-23 accelerometers, each with a nominal full-scale range of 2 g (PVCC and PVPP) or 1g (PVEF). (g is the value of gravitational acceleration on the surface of the Earth, equal to ~980 cm/s^2 at sea level.) The instruments record ground acceleration in 3 mutually perpendicular directions (East-West, North-South, and vertical). The first strong-motion instrument was installed near the injection wellhead (station code PVPP) in January, 1998. In November, 1999, a second strong-motion instrument was installed near the surface treatment facility (station code PVEF). A third strong-motion instrument was installed in the town of Paradox, Colorado (station code PVCC) following an M_L 4.0 induced earthquake on November 7, 2004.

Residents of the nearby community of Paradox, and in surrounding areas, reported feeling strong shaking from the January, 2013 earthquake. These reports are consistent with recordings obtained from the strong motion instruments. These data show peak horizontal accelerations (PHA) of 287 cm/s^2 (0.29 g) in the town of Paradox, 150 cm/s^2 (0.15 g) near the wellhead, and 75 cm/s^2 (0.08 g) at the surface treatment facility.

To get a sense of whether ground motions recorded at Paradox Valley during the January, 2013 earthquake differed substantially from what would be expected for tectonic earthquakes at similar magnitudes and distances, we have compared the recorded horizontal ground motions to ground motions estimated using the Next Generation Attenuation (NGA) empirical ground-motion prediction equations (Power and others, 2008). We use four of the NGA equations (Abrahamson and Silva, 2008; Boore and Atkinson, 2008; Campbell and Bozorgnia, 2008; Chiou and Youngs, 2008), and compute a mean value by assigning equal weight to each NGA equation used. To use the NGA equations, the following site properties must be assumed: (1) V_{S30}, defined as the time-averaged shear-wave velocity in the upper 30 m of soil; and, (2) $Z_{1.0}$ and $Z_{2.5}$, defined as the depths to where shear-wave velocities reach 1.0 and 2.5 km/s, respectively. We have assumed site V_{S30} values corresponding to moderate to soft soil sites, and computed $Z_{1.0}$ and $Z_{2.5}$ values using the relations in Abrahamson and Silva (2008) and Campbell and

Bozorgnia (1987), following the suggestions of Kaklamanos and others (2011). Assumed properties required for the NGA relations are shown in Table 2-3. The NGA values are for a randomly oriented horizontal component of motion, but we have not corrected the data to obtain the random component.

Table 2-3. Input parameters used for estimating ground motions from the NGA equations. See Kaklamanos and others (2011) for a description of the parameters.

Site	R_{JB} (km)	Z_{TOR} (km)	R_{RUPT} (km)	*Dip* (deg)	*Rake* (deg)	*Width* (km)	V_{S30} (m/s)	$Z_{1.0}$ (m)	$Z_{2.5}$ (m)
PVCC	4.9	4.0	6.3	80	5	0.6	300	330	1700
PVPP	7.1		8.1				530	170	1100
PVEF	10.0		10.8				400	220	1300

In general, the observed short-period (< 0.4-second) ground motions from the January 24th earthquake are substantially greater than the NGA relations predict, given our assumed site properties. The mean NGA acceleration and velocity response spectra are shown for each spectral period in Figure 2-10 through Figure 2-15, and compared to the observed response spectra. For periods greater than 1.0 second, the observed results are consistent with the NGA relations. The recorded high-frequency (> 2.5 Hz) recorded ground motions are substantially higher than would be predicted by the NGA equations. This effect is greatest at PVCC, but is observed at all stations. Comparison of the recorded peak horizontal accelerations, 1.0-second spectral accelerations, and peak horizontal velocities are shown in Figure 2-16 through Figure 2-18. The recorded PHA at PVCC is nearly two standard deviations above the NGA mean PHA (Figure 2-16), and peak horizontal velocity (PHV) is more than 1 standard deviation above the NGA mean PHV (Figure 2-18). At PVEF, the PHA and PHV values are also above the mean NGA values, but are within 1 standard deviation of the mean. In contrast, the 1.0-second spectral acceleration values at all sites are within 1 standard deviation of the NGA mean (Figure 2-17).

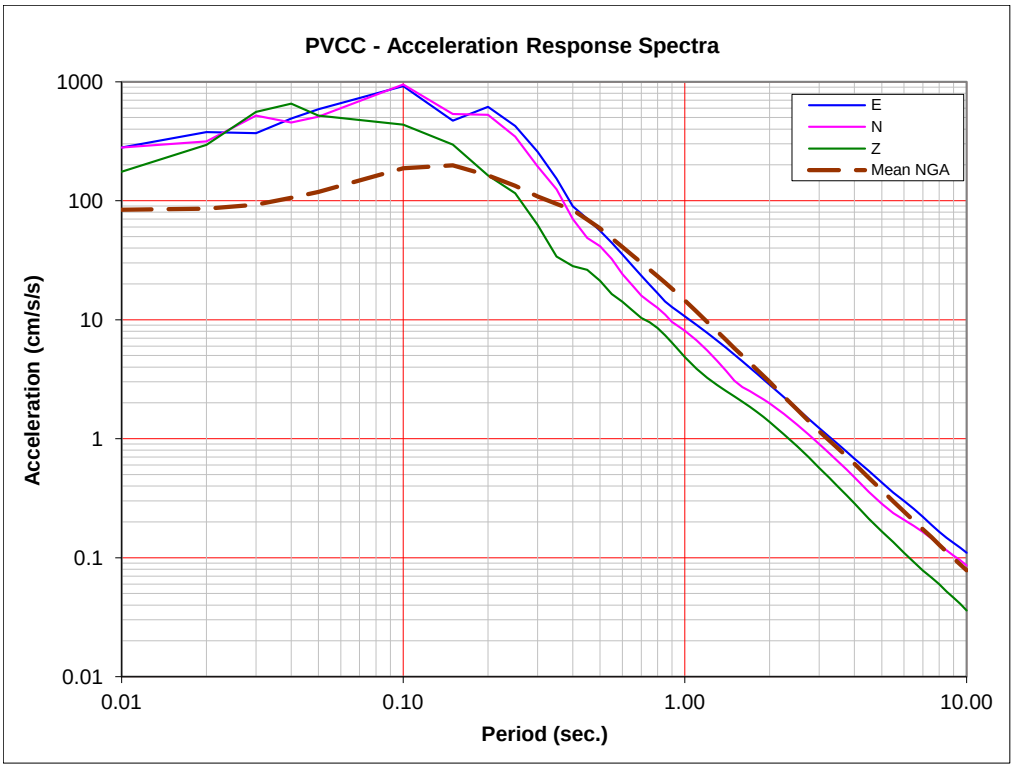

Figure 2-10. Acceleration response spectra for the Paradox Community Center (PVCC), and comparison with NGA results.

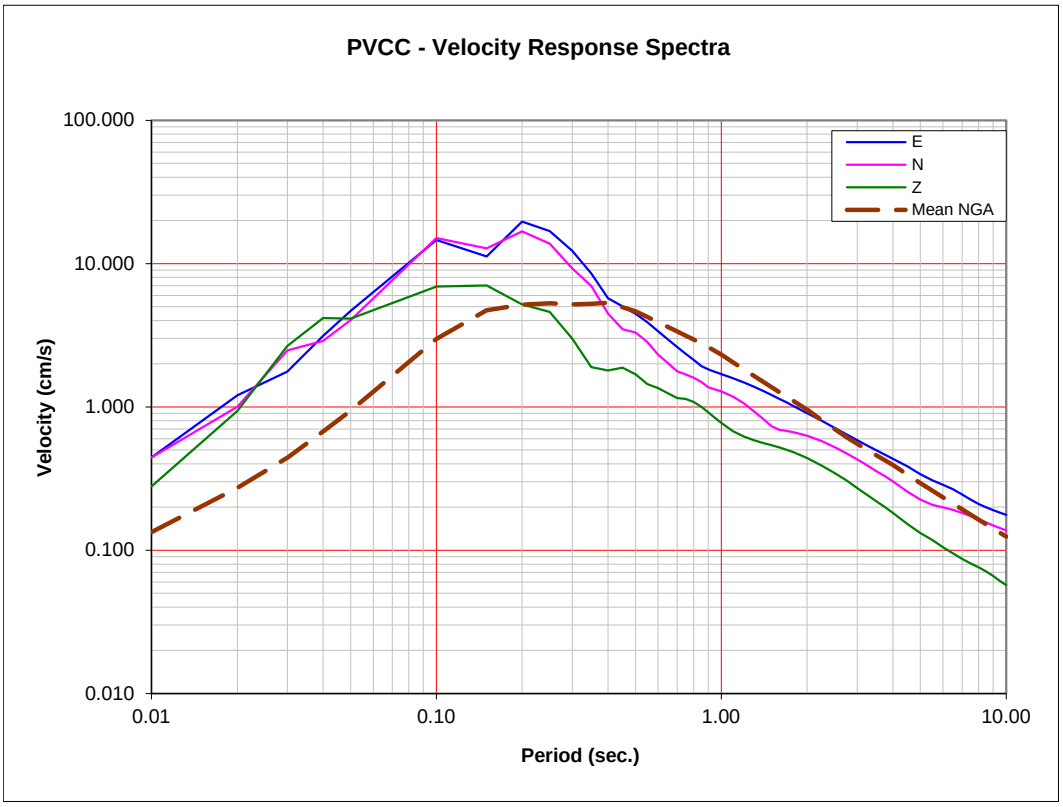

Figure 2-11. Velocity response spectra for Paradox Community Center (PVCC), and comparison with NGA results.

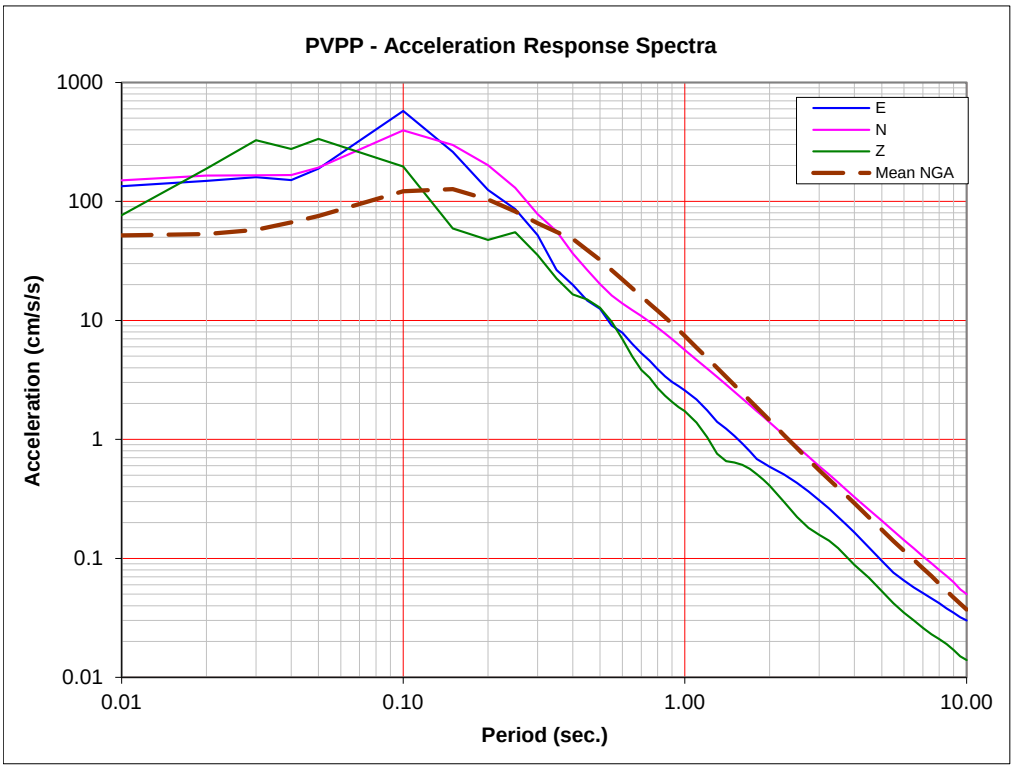

Figure 2-12. Acceleration response spectra for the injection well (PVPP), and comparison with NGA results.

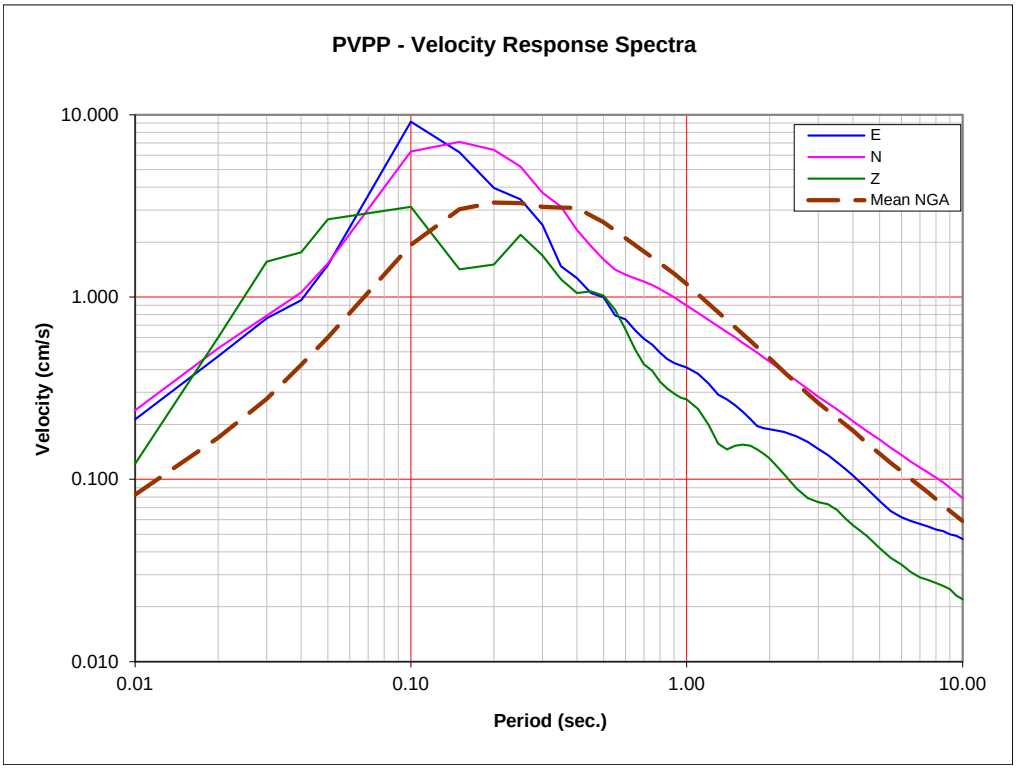

Figure 2-13. Velocity response spectra for the injection well (PVPP), and comparison with NGA results.

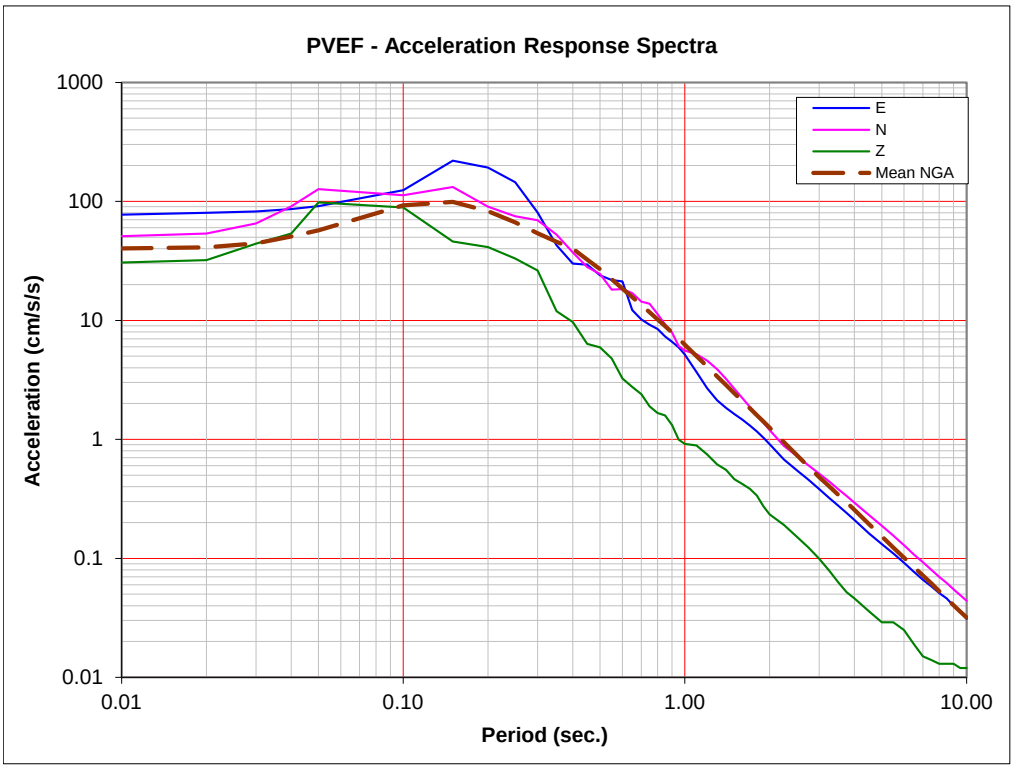

Figure 2-14. Acceleration response spectra for the surface-treatment facility (PVEF), and comparison with NGA results.

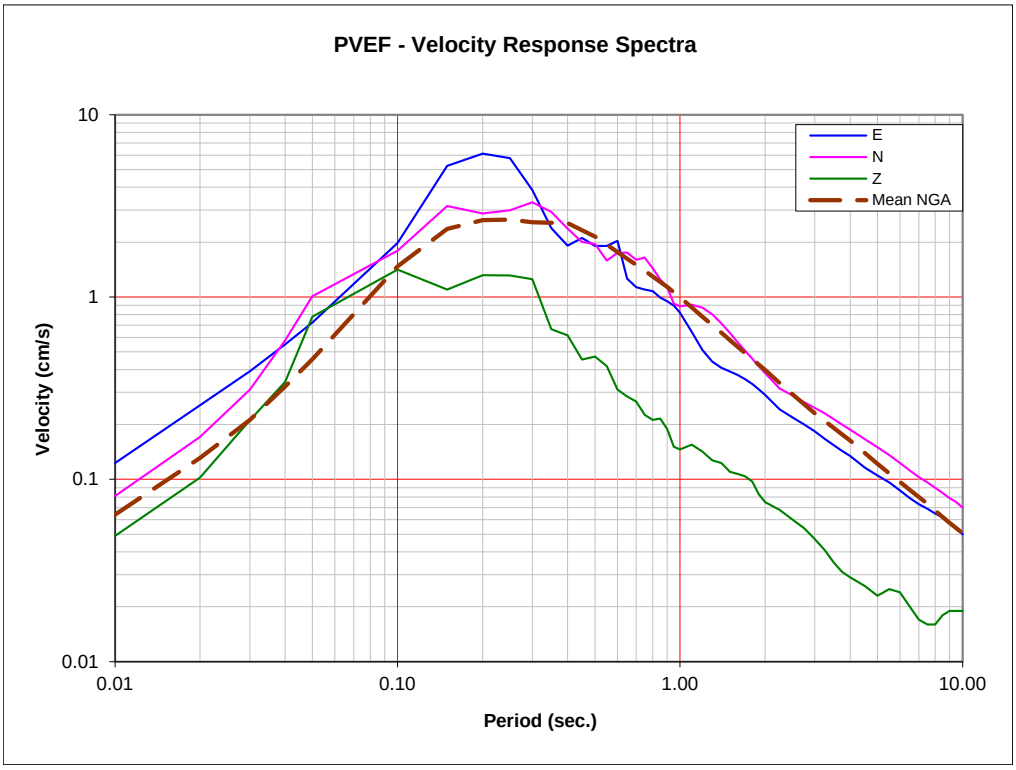

Figure 2-15. Velocity response spectra for surface-treatment facility (PVEF), and comparison with NGA results.

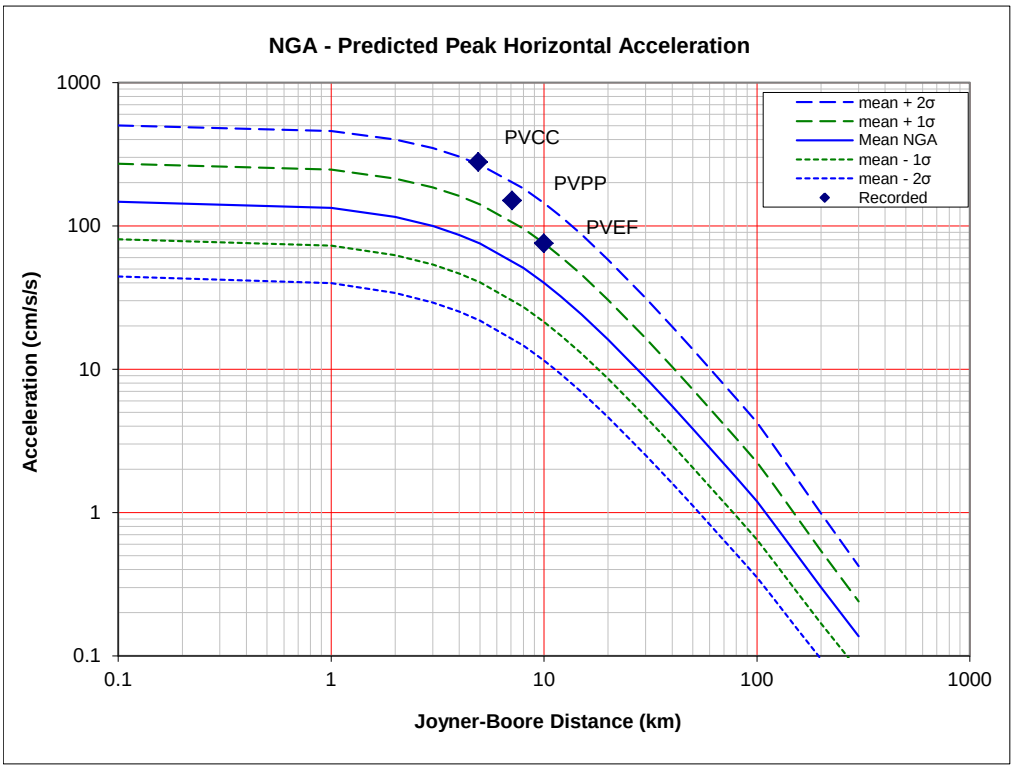

Figure 2-16. Comparison of observed PHA values versus distance, with NGA results.

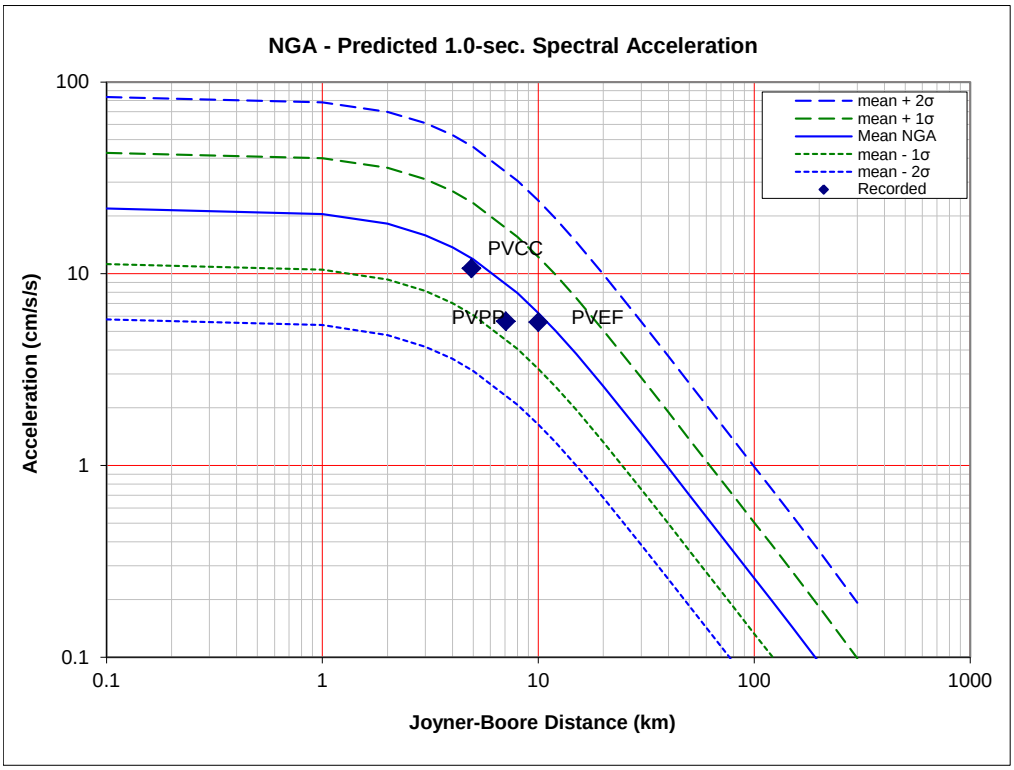

Figure 2-17. Comparison of observed 1.0-second spectral acceleration values versus distance, with NGA results.

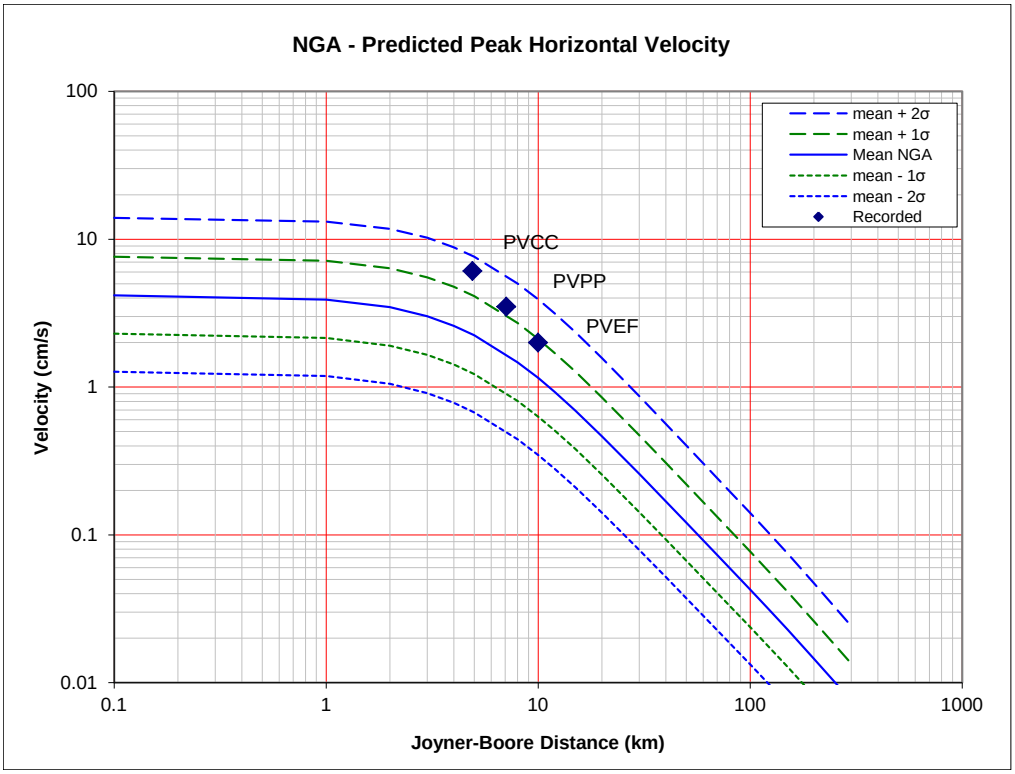

Figure 2-18. Comparison of observed peak velocity values versus distance, with NGA results.

The strong-motion records also can be used to evaluate the level of shaking in the town of Paradox by comparing them to vibration control standards used by the mining and construction industries to minimize shaking damage to residential structures. This comparison is done in the following section.

2.6 Ground Motion Effects and Standards

We know of no regulatory standards for control of shaking from induced seismicity applicable to the Paradox Valley area. However, well-established standards exist for the control of vibrations during blasting and construction activities, which are applicable to residential structures. According to an induced seismicity protocol recently published by the U. S. Department of Energy (DOE) (Majer and others, 2012), "the seismic energy from these activities would be similar to that from induced seismic events (in frequency bandwidth and range) and thus be applicable to induced seismicity cases". This protocol specifically addresses seismicity induced by fluid injection during geothermal energy development. However, we believe that the recommendations in this protocol are directly applicable to seismicity induced by fluid injection at the Paradox Valley Unit because the physical mechanisms for triggering the induced earthquakes, and therefore their characteristics, are essentially the same. According to the DOE protocol, of the various standards used for blasting and construction activities, those established for the regulation of ground vibrations from surface mine blasting are the most applicable to injection-induced seismicity.

The Office of Surface Mining (OSM), U.S. Department of the Interior, has performed extensive studies of ground vibrations and building damage caused by surface blasting. These studies began as early as the 1930s. A report published by OSM in 1971 summarizes the results from a 10-year program conducted to study the effects of vibrations from surface blasting (Nicholls and others, 1971). One of the main goals of this program was to establish the relationship between the magnitude of ground vibration and the resulting damage to structures. The report recommends that peak particle velocity of ground motion, as measured in any of 3 mutually perpendicular directions, be used as the measurement of vibration from blasting for correlation to damage of residential structures. The report states that, based on analysis of data from several earlier studies, particle velocity more closely relates to structural damage than measurements of displacement or acceleration. The report concludes that a peak particle velocity (PPV) limit of 2.0 in/sec (5.1 cm/sec) will provide protection from damage to residential structures in the majority of cases (Nicholls and others, 1971). The report also states that, "If the observed particle velocity exceeds 2.0 in/sec in any of the 3 orthogonal components, there is a reasonable probability that damage will occur to residential structures."

Additional studies indicated that the potential for damage to structures varied considerably depending on the frequency range of the ground vibrations. This variation is due to the natural frequency response of buildings, which can amplify the particle velocities. Results published by the Office of Surface Mining in 1980 indicate that the natural resonance frequencies for typical one- to two-story residential structures range from about 4 to 24 Hz, and the maximum amplification factors measured for these structures occurred for ground vibrations between 5 and 12 Hz (Siskind and others, 1980). As a result of the new studies, OSM reduced the maximum peak particle velocity limit for ground vibrations under 40 Hz. For ground vibrations in this frequency range, OSM concluded that a PPV limit of 0.5 in/sec (1.3 cm/sec) will provide protection from blast damage for older homes with plaster walls. Modern drywall (gypsum board) interior-walled homes were judged to be safe at somewhat higher vibration levels, up to 0.75 in/sec (1.9 cm/sec) (Siskind and others, 1980). The report left the recommended limit for ground vibrations above 40 Hz at the previous level of 2.0 in/sec. The frequency content of ground vibrations generated by induced seismic events fall within the lower frequency range (< 40 Hz), and therefore the lower PPV limits would be applicable.

The current OSM standards for ground vibrations from surface mine blasting are stated in Title 30 of the Code of Federal Regulations (2012) and summarized in Table 2-4. The regulations state that the maximum ground vibration shall not exceed the limits given in Table 2-4 "at the location of any dwelling, public building, school, church, or community or institutional building". The regulations also state that the particle velocity should be measured in 3 mutually perpendicular directions and that the vibration limits apply to each of the 3 measurements. Three separate peak particle velocity limits are listed in the

Federal Code, depending on the distance of the structure from the blasting site. The limits are stricter for farther distances, because the ground motions become more dominated by lower frequencies at greater distances from the source. As discussed above, the lower frequencies are more damaging to structures than the higher frequencies. The PPV limit listed for distances greater than 5000 ft (0.75 in/sec; 1.91 cm/sec) is the most applicable to ground vibrations from induced earthquakes. The OSM limits were adopted by the State of Colorado for the regulation of ground vibrations from blasting associated with coal mining in 1980 (Alt and others, 1980).

Table 2-4. Summary of current ground vibration limits from blasting set by the Office of Surface Mining, Reclamation and Enforcement, U. S. Department of the Interior; taken from Title 30, Subchapter K, of the Code of Federal Regulations, dated July 1, 2012.

Distance from Blasting Site (ft)	Peak Particle Velocity	
	(in/sec)	(cm/sec)
0 – 300	1.25	3.18
301 – 5000	1.00	2.54
5001 and higher	0.75	1.91

In order to compare the ground vibrations measured by the PVSN strong motion instruments to the vibration limits given by the OSM regulations, the acceleration time histories were integrated to produce velocity records. The velocity data were then corrected for instrument response. The final velocity records are presented in Figure 2-19 (PVCC), Figure 2-20 (PVPP), and Figure 2-21 (PVEF).

The peak particle velocity measured in the town of Paradox for January 24, 2013 earthquake was 6.2 cm/sec (2.4 in/sec, East component). This ground vibration level is more than 3 times the 1.9 cm/sec (0.75 in/sec) limit set in the OSM regulations for distances from the source exceeding 5000 ft. A comparison of the peak particle velocity records measured in the town of Paradox and these standards is shown in Figure 2-19. Based on this comparison, it is possible that minor damage may have occurred to structures in and near the town of Paradox from ground vibrations produced by the earthquake.

The peak particle velocity measured at the surface treatment facility is 1.9 cm/sec (0.78 in/sec, East component), slightly exceeding the OSM safe vibration limit (Figure 2-21). Based on the OSM standards, damage would not be expected to have occurred at this location from the earthquake.

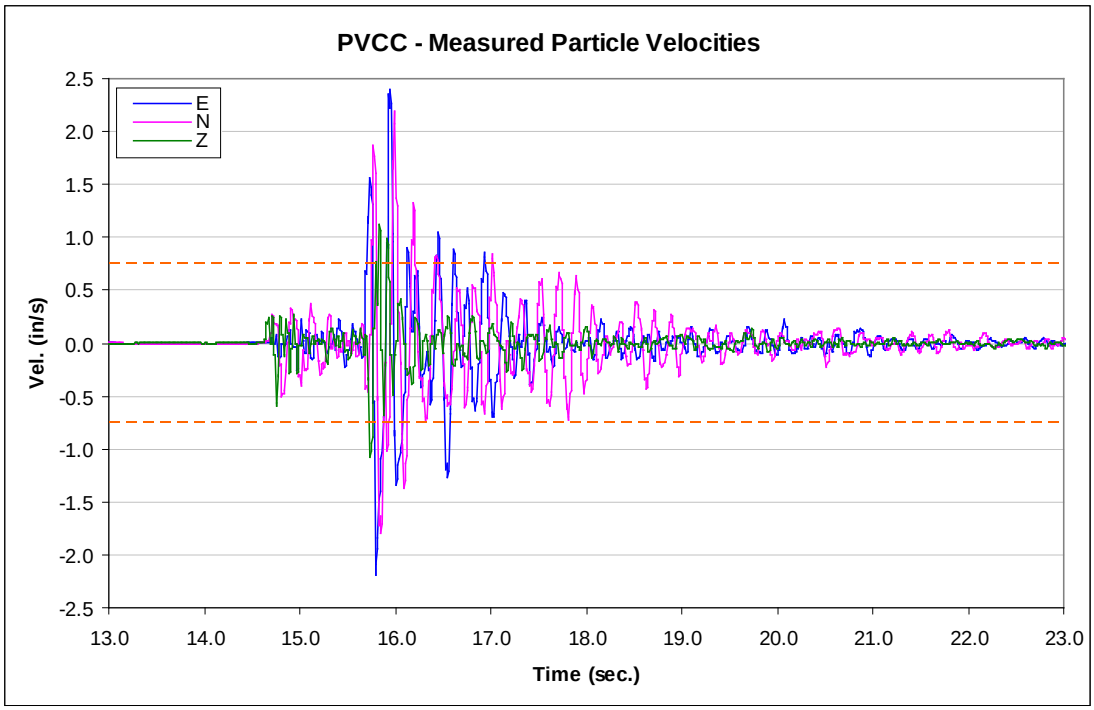

Figure 2-19. Comparison of measured particle velocities at station PVCC (Town of Paradox, community center) and the blasting standard of 0.75 in/sec peak particle velocity (orange dashed lines). Recorded ground motions reached a maximum peak particle velocity of 2.4 in/sec, more than 3 times the standard.

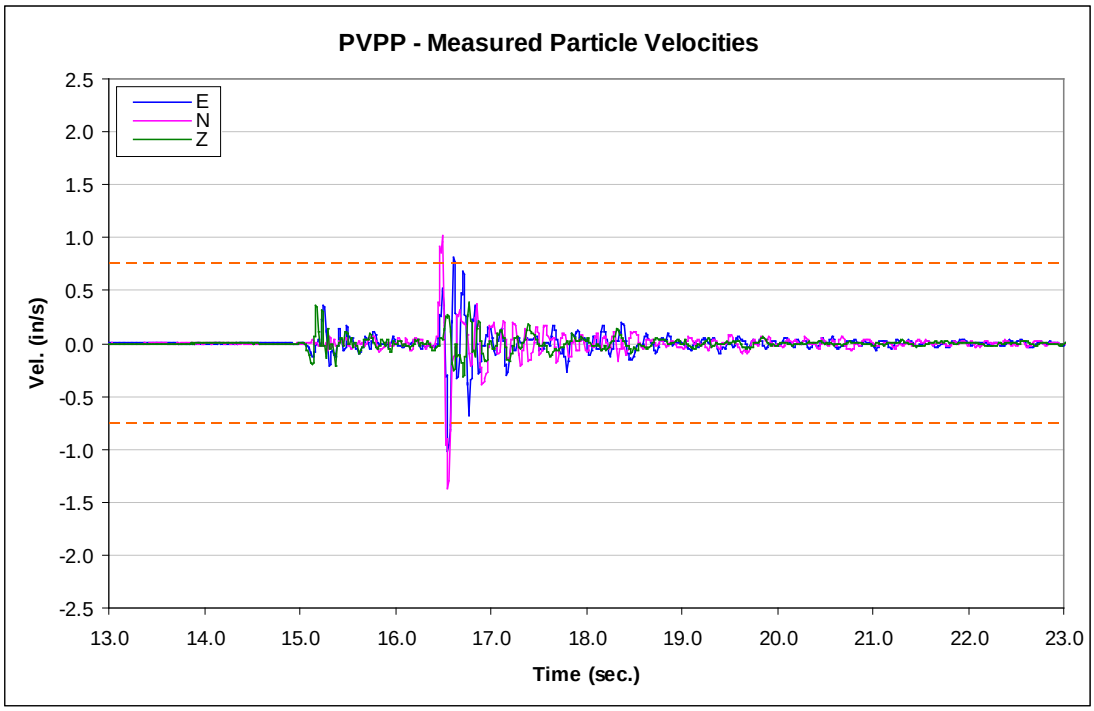

Figure 2-20. Comparison of measured particle velocities at station PVPP (near the injection well-head) and the blasting standard of 0.75 in/sec peak particle velocity (orange dashed lines). Recorded ground motions reached a maximum peak particle velocity of 1.4 in/sec, exceeding the standard.

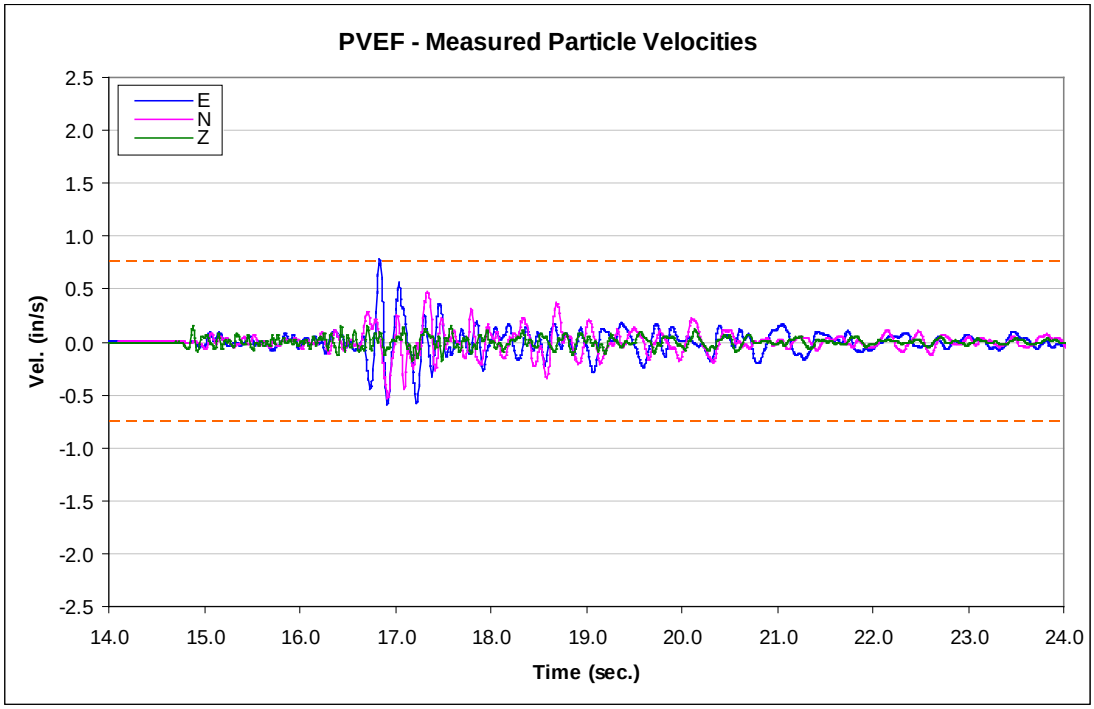

Figure 2-21. Comparison of measured particle velocities at station PVEF (Surface Treatment Facility and brine extraction) and the blasting standard of 0.75 in/sec peak particle velocity (orange dashed lines). Recorded ground motions reached a maximum peak particle velocity of 0.78 in/sec, slightly exceeding the standard.

2.7 Triggering Mechanism

During fluid injection, earthquakes may be induced by increases in pore pressure, by redistribution of stress (from accommodation of the injected fluid into the rock or from the occurrence of previously-induced earthquakes), or by cooling and shrinking of the rock matrix. The latter thermodynamic effect is important in geothermal areas but is unlikely to be a dominant factor at PVU, except possibly in the near vicinity of the injection well. Changes in pore pressure and the redistribution of stress are likely the major triggering mechanisms for earthquakes induced by fluid injection at PVU.

The triggering mechanism for the January 24, 2013 event in the NW cluster is not known. Previous analysis shows a general correlation between the occurrence of induced earthquakes in the near-well region (within 4 to 5 km of the injection well) and long-term average injection pressures (Block and Wood, 2009), as is shown in Figure 2-22. This correlation suggests that pore pressure increase is a dominant factor contributing to the rate and magnitude of induced seismicity in the near-well region. The same analysis, however, does not show a correlation between injection pressure and seismicity for earthquakes occurring at distances greater than 5 km, such as those in the NW cluster (Figure 2-22, lower plot).

Roeloffs and Denlinger (2009) suggested that seismicity was initially triggered in the NW cluster by stress redistribution. This hypothesis stems from the fact that the seismicity in the NW cluster began only 1 year after the start of continuous injection operations, too soon for significant pore pressure changes to have propagated 6 km from the well, based on results from an axisymmetric fluid flow model. Mahrer and others (2008) proposed a different possibility - a northwest-trending fault zone allows for relatively rapid propagation of pore pressure from the vicinity of the injection well to the NW cluster (a feature the radially-symmetric fluid flow model of Roeloffs and Denlinger would not have accounted for). In this case the earthquakes may be primarily driven by pore pressure changes. It is also feasible that the triggering mechanisms for earthquakes occurring in the NW cluster have changed over time, with stress redistribution being the primary cause of the initial seismicity and pore pressure increase becoming an increasingly important factor at some later date as the pressure front from injection has expanded over time.

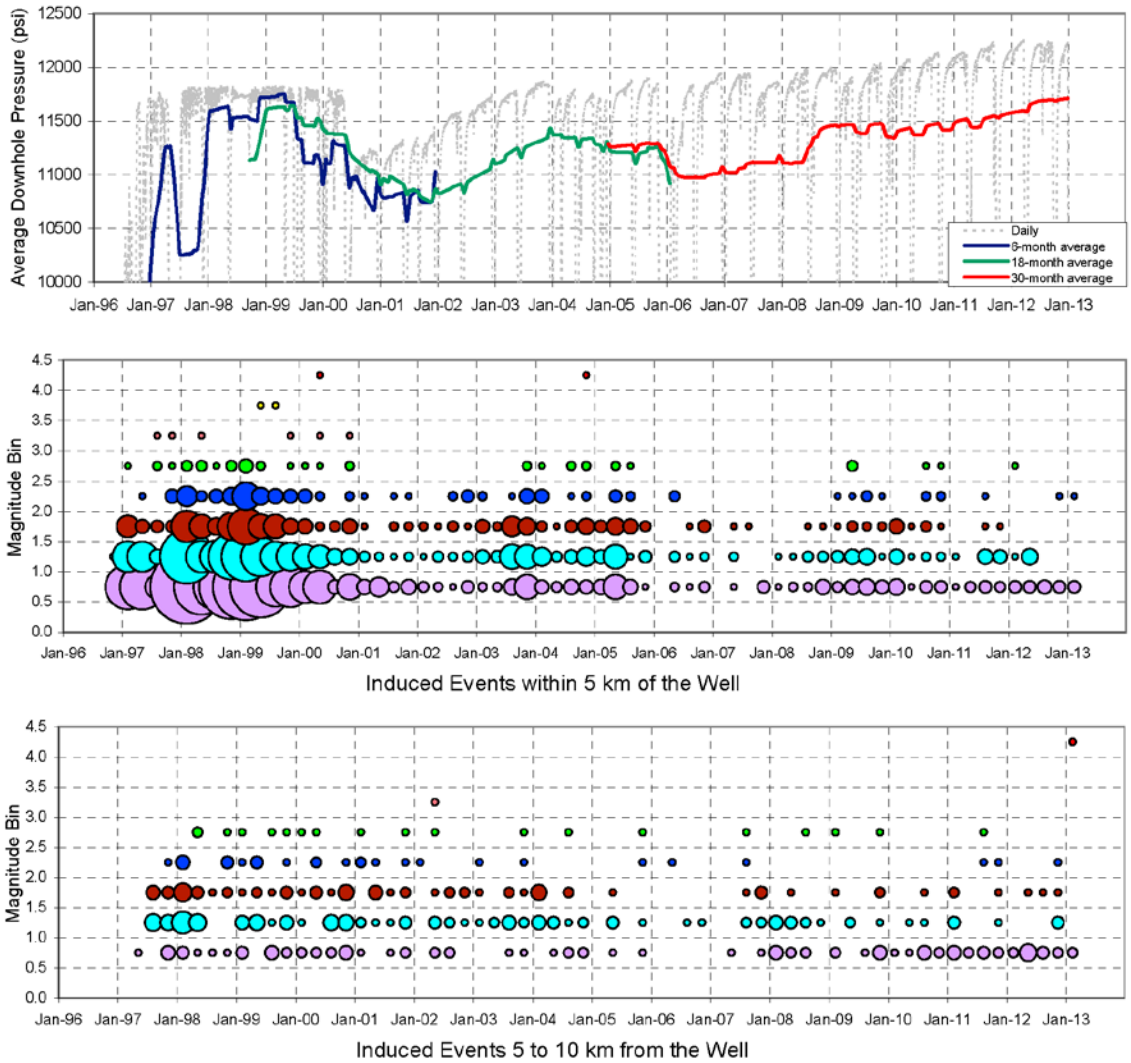

Figure 2-22: Injection downhole pressure data averaged over daily, 6-month, 18-month, and 30-month time periods (top), and occurrence of induced seismicity as a function of time and magnitude within 5 km of the injection well (middle) and at distances of 5 to 10 km from the well (bottom). In the seismicity plots, the area of each circle is scaled by the number of events in a given quarter-year and magnitude range. The low seismicity rate in the smaller magnitude bins from about mid-2005 to mid-2007 in the bottom plot is believed to be due to an unusually large number of offline stations.

3 Seismic Hazard Factors

Factors controlling seismic hazard include seismicity rates, distribution of earthquake magnitudes, and the distances from the primary areas of seismicity to residences or other sites of concern for strong ground shaking. For the induced seismicity at Paradox Valley, some of these factors appear to change substantially over time periods of several years or less. Such variability makes it difficult to estimate long-term seismic hazard, since it will not be sufficient either to determine parameters at a single point in time, or to characterize hazard using the occurrence of a particular earthquake. In order to evaluate seismic hazard arising from long-term fluid injection at PVU, we examine how parameters normally used to characterize hazard have changed over the life of the project, and assess how they may change in the future.

In this section we review what is currently known about key factors controlling seismic hazard arising from injection operations at PVU, and examine how these have varied over the history of the project. We also discuss important factors for which we have little or no data.

3.1 Geographical Distribution of Seismicity

To first approximation, common measures of earthquake shaking (e.g., peak horizontal acceleration or velocity) depend on the magnitude of the earthquake and the distance between the causative fault and a site of interest. For a given magnitude, the expected ground motions (and associated seismic hazard) generally are higher if earthquakes are occurring closer to a site. For induced earthquakes, maximum magnitude may be related to the volume of rock stimulated by injection, and the stimulated volume may be inferred by the extent of the cloud of induced seismicity. An analysis of the spatial evolution of induced seismicity in the Paradox area therefore can provide important constraints for evaluating hazards. Data collected by the Paradox Valley Seismic Network provides the basis for such an analysis.

3.1.1 Relation of Seismicity to Inhabited Areas in Paradox Valley

The geographical distribution of induced seismicity at PVU has evloved over time, with clusters of seismicity expanding from the near-well region, during the earliest phases of injection, to locations closer to inhabited areas in Paradox Valley. Since the inhabited areas are spread out over a large region, the issue of the distances between potential seismic sources to sites of concern is complex. Below we provide a brief review of the geographical evolution of PVU-induced seismicity over time. We then provide a simplified look at the source-to-site

distance parameter by examining the evolution of closest distances from induced earthquakes to the local population center, the town of Paradox in northern Paradox Valley.

3.1.1.1 Geographical Evolution of Seismicity

The geographical distribution of induced seismicity over time is presented in the series of maps shown in Figure 3-1 and Figure 3-2. For reference, we have delineated and named four key seismicity areas: **(1) Near-well:** By the end of the injection tests in 1995, earthquakes were occurring 3 to 4 km from the injection well (Figure 3-1a). This area of induced seismicity immediately surrounding the injection well is referred to here as the "near-well" region. **(2) Northwest (NW) cluster**: In mid-1997, about a year after the start of continuous injection, earthquakes began occurring 6 to 8 km northwest of the injection well (Figure 3-1b). This cluster of induced seismicity is called the "northwest (NW) cluster". **(3) Northern valley:** In mid-2000, earthquakes were first detected 12 to 14 km from the injection well, along the northern edge of Paradox Valley (Figure 3-1b). Several distinct clusters of earthquakes have occurred along the northern edges of the valley since 2000 (Figure 3-2a). The earthquakes occurring in all of these clusters are referred to as "northern valley events". **(4) Southeast (SE) cluster:** An earthquake was first detected about 6 km southeast of the injection well in 2004 (Figure 3-2a), but the seismicity rate in this area markedly increased beginning in 2010 (Figure 3-2b). This group of earthquakes is referred to as the "southeast (SE) cluster". In recent years, a few isolated earthquakes have been detected in previously aseismic areas, including in the center of Paradox Valley (Figure 3-2b).

The geographical expansion of seismicity has varied over time. The rate of expansion was highest during the later injection tests (1994-1995) and the early phase of continuous injection (1996-2000). However in mid-2000, when the PVU injection flow rate was decreased by about 33% in response to a magnitude 4.3 induced earthquake, the geographical expansion of seismicity slowed greatly, and the spatial extent of the near-well and NW-cluster areas largely stabilized. While new clusters of seismicity appeared in the northern-valley area in the years following the reduction in flow rate, seismicity rates there were very low. This relatively stable period lasted for about a decade.

Beginning in 2009, the spatial distribution and rates of seismicity within 10 km of the injection well began to change. Five induced earthquakes of magnitude 2.5 or greater occurred in 2009. This was the highest annual rate of M 2.5+ earthquakes in 5 years, and the second highest rate since the injection flow rate was reduced in mid-2000. A distinct group of earthquakes developed in 2010 about 6 km southeast of the injection well, the SE cluster. While the first detected SE cluster event occurred in 2004, with 2 additional events recorded in 2008 and 2009, beginning in 2010 the SE cluster experienced increasing rates of seismicity: 11 events in 2010, 17 events in 2011, and 25 events in 2012.

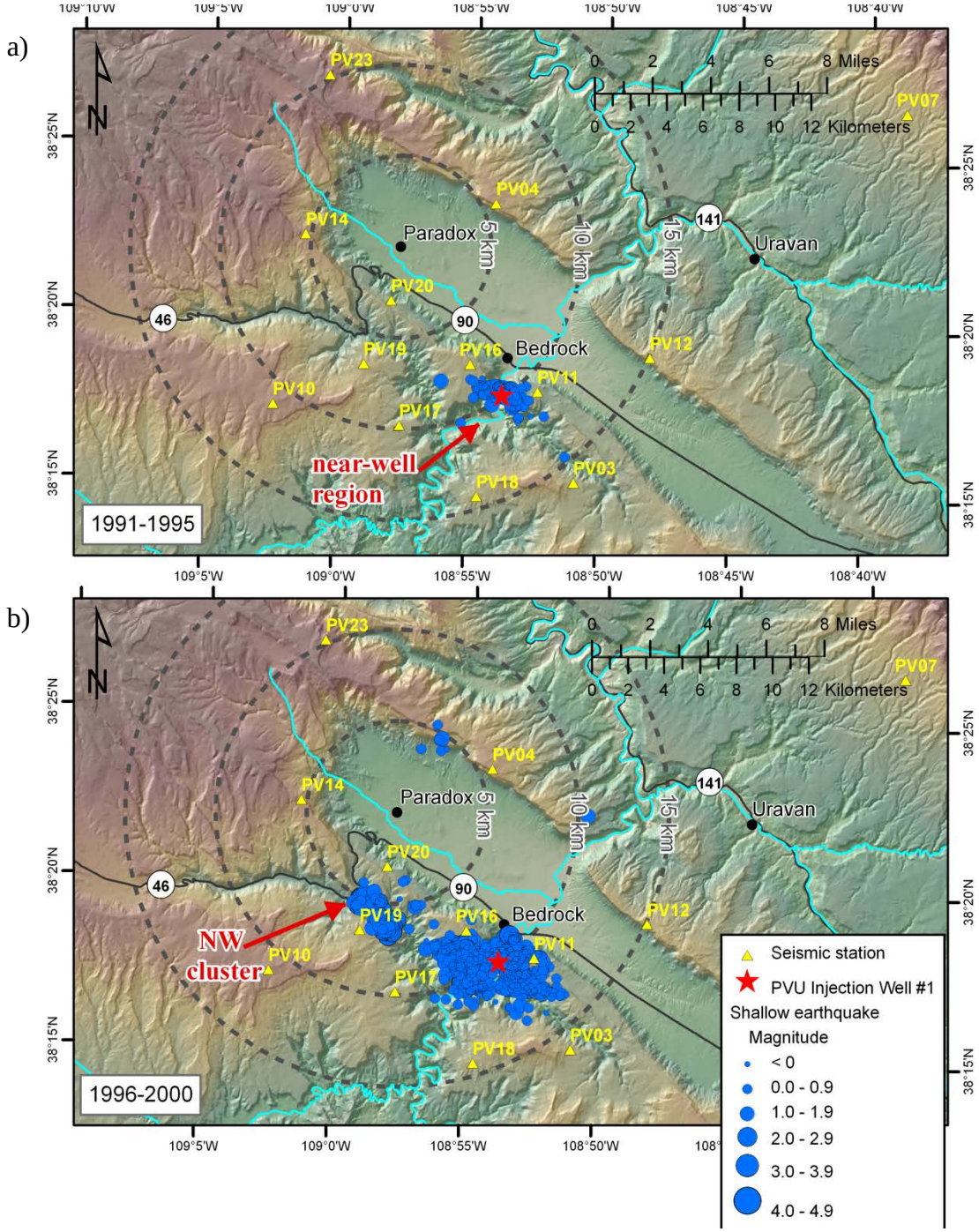

Figure 3-1. **Maps showing the geographical distribution of shallow seismicity recorded in the Paradox Valley area from 1991 through 2000: (a) injection tests, 1991-1995 (b) continuous injection, 1996-2000. All detected earthquakes locating less than 8.5 km deep (relative to the ground surface elevation at the injection wellhead) are included.**

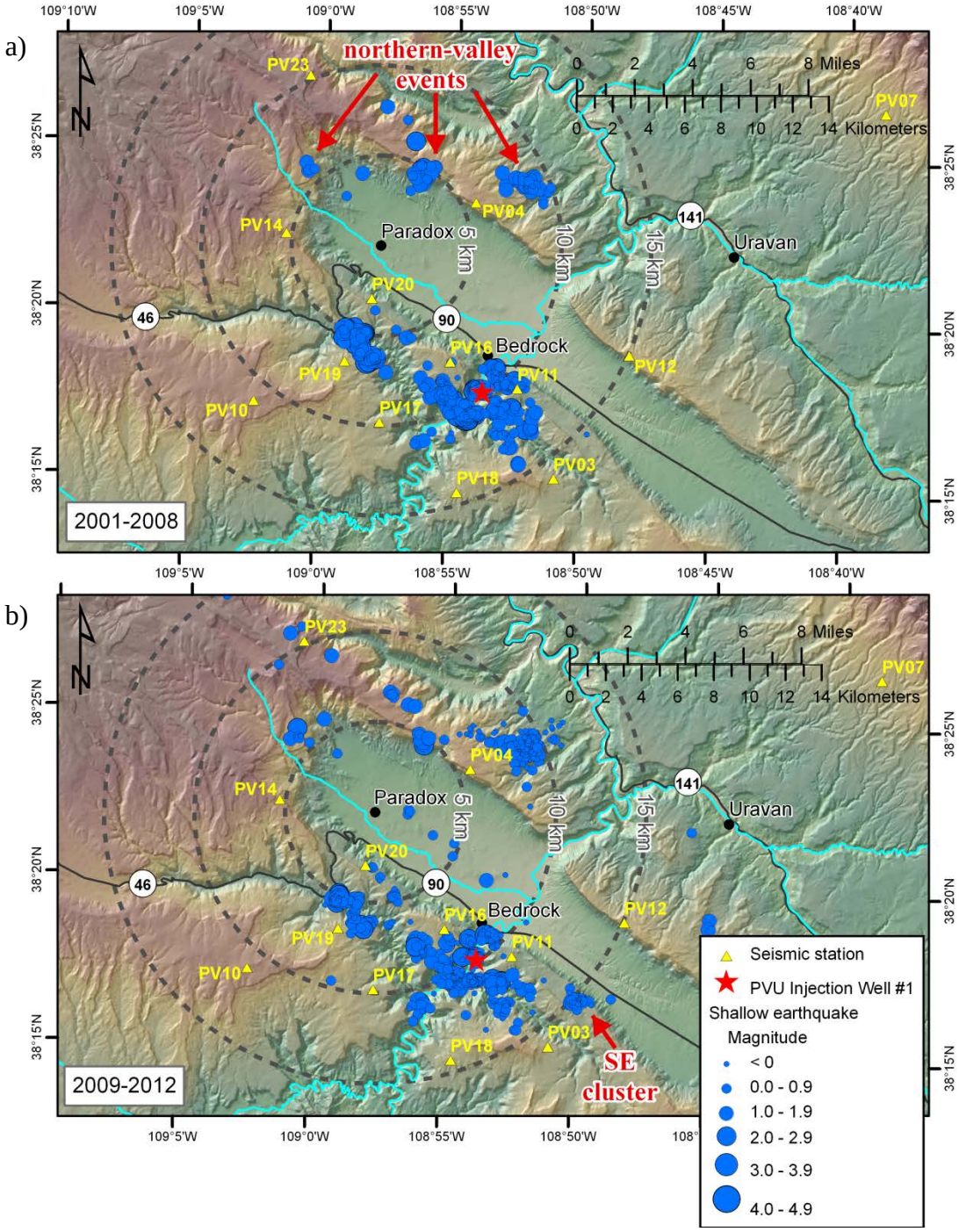

Figure 3-2. Maps showing the geographical distribution of shallow seismicity recorded in the Paradox Valley area from 2001 through 2012: (a) continuous injection, 2001-2008 (b) continuous injection, 2009-2012. All detected earthquakes locating less than 8.5 km deep (relative to the ground surface elevation at the injection wellhead) are included.

Seismicity rates within the northern-valley area have also changed in recent years. During each year from 2000 (when the northern valley seismicity was first detected) to 2009, between 2 and 33 earthquakes were recorded. In 2010, the rate increased markedly: 557 northern-valley earthquakes were recorded, with the

majority occurring in a single swarm lasting just 16 days. Northern-valley seismicity rates remained elevated during 2011, with 113 earthquakes recorded, but declined back to pre-2010 rates during 2012, with just 10 events recorded.

Beginning in mid-2010 and continuing through the present, several shallow earthquakes have been detected beneath the floor of Paradox Valley. Three earthquakes were detected in 2010; 2 in 2011; and 5 in 2012. Although the total number of events is small (10 events in 3 years), no earthquakes were detected beneath the floor of Paradox Valley in the 25 years of seismic monitoring prior to 2010. The renewed spatial expansion of seismicity and increased seismicity rates in recent years may be related to a trend of increasing injection pressures at the well, which in turn is related to the long-term average injection flow rates.

3.1.1.2 Epicentral Distance Evolution of Seismicity

Because most of the local population near the injection well resides in the northern part of Paradox Valley, with the town of Paradox being the main population center, the distance of PVU-induced earthquakes from Paradox is an important seismic hazard factor. To evaluate how the distance of PVU-induced seismicity from the town of Paradox has changed over time, we plot the seismicity as a function of date and distance from Paradox in Figure 3-3. In addition, the maps in Figure 3-1 and Figure 3-2 include circles of equal distance from Paradox, for distances of 5, 10 and 15 km.

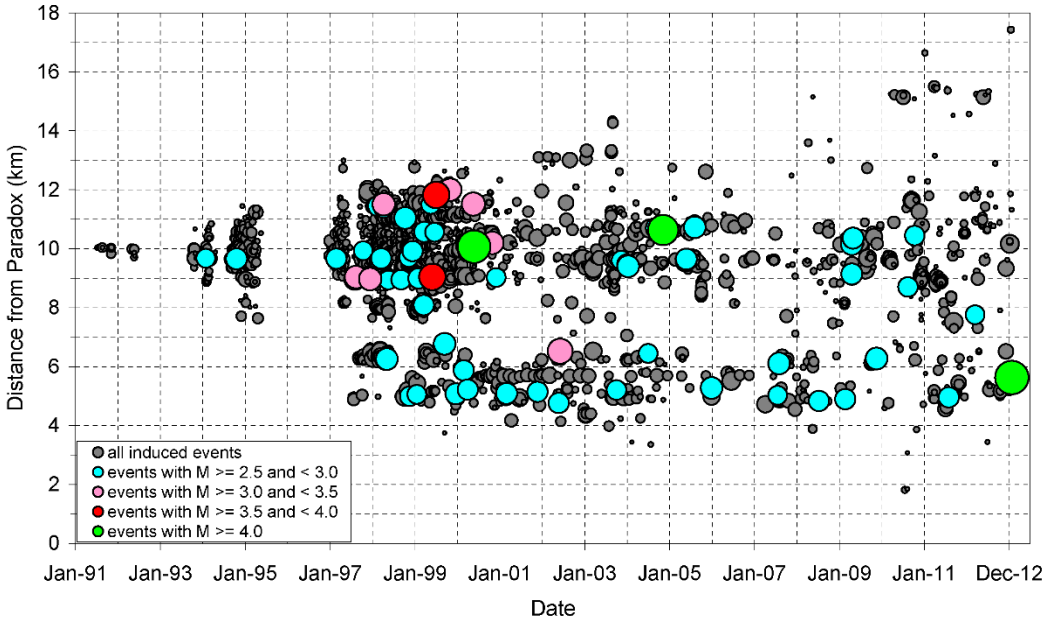

Figure 3-3. Occurrence of PVU-induced seismicity as a function of date, distance from the town of Paradox, and earthquake magnitude. All recorded events locating less than 8.5 km deep (relative to the ground surface elevation at the injection wellhead) are included. Each circle represents a single earthquake, with its diameter scaled by event magnitude.

Epicentral distances between the town of Paradox and the nearest induced earthquakes have changed markedly over time, as shown by the plot of distance versus time (Figure 3-3), and by epicenter maps (Figure 3-1 and Figure 3-2). The injection well is located at a distance of 10 km from Paradox. During the earliest injection tests (1991-1994), the seismicity was restricted to within about 1 km of the injection well, and therefore the epicentral distance between the induced seismicity and the town of Paradox ranged from slightly less than 9 km to 11 km (Figure 3-3). During the later injection tests (1994-1995), the induced seismicity cloud expanded away from the injection well, with earthquakes occurring between 7.5 and 11.5 km from Paradox. During continuous injection operations, as the boundary of the seismicity cloud has progressively expanded away from the well, earthquakes have occurred at both smaller and larger distances from Paradox, with shallow, potentially-induced earthquakes now being detected as close as 2 km from Paradox, and as far as 17 km.

The earthquakes occurring closest to the town of Paradox include events in the center of Paradox Valley (with epicentral distances as small as 1.9 km), events in the NW cluster (at distances of about 3.5 to 7 km), and events in some of the northern-valley clusters (at distances of about 4 to 7 km). To date, of the earthquake clusters occurring near the town of Paradox, only the NW cluster has produced M>3 earthquakes. As discussed in the following sections, however, both the rates and magnitude distributions of PVU-induced seismicity have varied significantly over time. Hence, we cannot exclude the possibility that future M>3 earthquakes will occur in the other earthquake clusters near the town of Paradox, including either the central or northern-valley areas.

3.1.2 Volumetric Evolution of Seismicity

Understanding the temporal and spatial evolution of brine in the subsurface is important for understanding how earthquakes are induced, and how earthquake hazards may be affected. For example, whether injected brine can be expected to be smoothly distributed within the rock mass near the well bore, or concentrated along discrete fracture networks opened up during injection, may have a significant effect on where future earthquakes are likely to occur and what magnitudes can be expected.

Brine migration can be inferred using several methods, including monitoring wells, leveling lines, borehole tiltmeters (Jahr and others, 2007; Jahr and others, 2008), gravimetry, seismic tomography, and seismicity. Of these methods, only induced seismicity data is readily available at PVU. Monitoring wells (e.g., new wells or re-entered abandoned wildcat wells) have not been available at PVU. Geochemical analysis of brine obtained from a wildcat well drilled in 2008 about 10 km northwest of the PVU well, and which penetrated the Leadville formation, indicated that PVU brine had not migrated to that location at the time of drilling. To our knowledge, no geodetic leveling lines are available in the area around the injection well, nor are there any borehole tiltmeters.

The relationship between induced seismicity and the migration of injected brine is poorly understood at PVU. Simple numerical models have been used to estimate the time and distance variations in pressure away from the wellbore (e.g., Roeloffs and Denlinger, 2009), but such models are difficult to validate in the absence of monitoring wells or other direct measurement. Following Shapiro and others (1997; 2003) we simply assume that the state of stress in the rock surrounding the injection well is close to critical, and that small changes in that stress state resulting from diffusion of pore pressure is the direct cause of most induced earthquakes. Specifically, we assume that induced earthquakes occur in response to a decrease in the effective normal stress on pre-existing fracture surfaces resulting from the diffusion of pore-pressure transients produced by injection (e.g., Shapiro and others, 1997; Shapiro and others, 2002; Shapiro and others, 2005). Fracture initiation is assumed to be adequately described by a Coulomb fracture criterion (Jaeger, 1969), and we assume that the observed seismicity is the result of frictional failure due to shearing (tensile failure events may also occur, but have not been observed in the seismicity data).

Following Shapiro and others (2011), we use the volume enclosed by the observed seismicity cloud as a working approximation to the total volume of rock stimulated by injection, although this may be an over-estimation if the seismicity is not homogeneously distributed. The stimulated volume is important because its size may be related to the maximum magnitudes of induced seismicity (Shapiro and others, 2011).

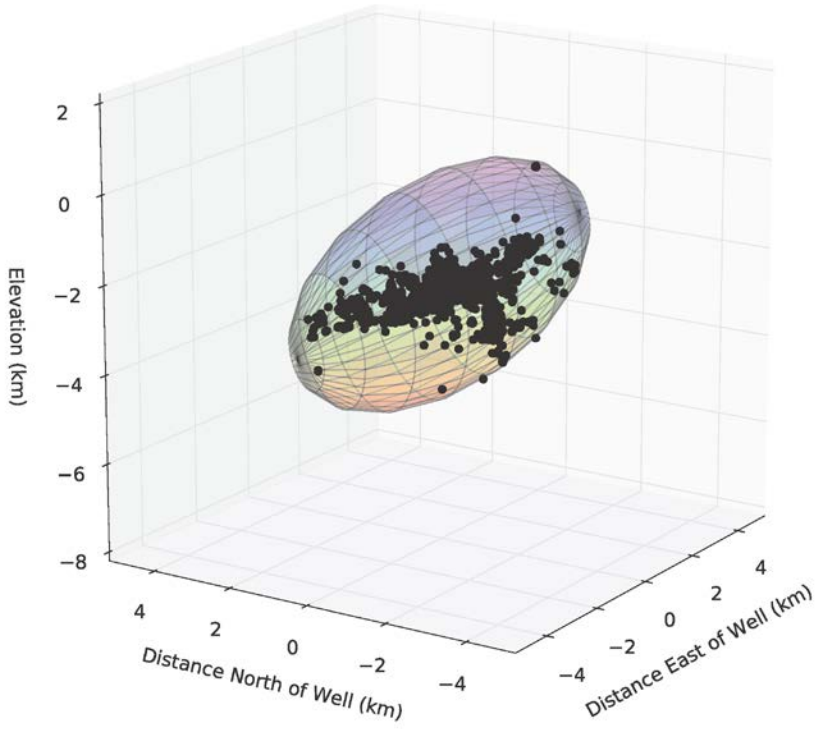

Figure 3-4. Example of minimum ellipsoid fit to hypocenters (grey dots) from the near-well cluster.

We model the volume of the seismicity cloud by determining the volume of the minimum ellipsoid enclosing all hypocenters within an identified cluster (Figure 3-4). Only high-quality, relatively-relocated hypocenters are used for this analysis. To determine minimum ellipsoids, we first selected well-defined, dense clusters of events, and ignored isolated hypocenters. This process is necessarily somewhat subjective, so alternative selections of hypocenters were considered, as shown in Figure 3-5. The final results do not appear to be strongly dependent on the hypocenter selections used.

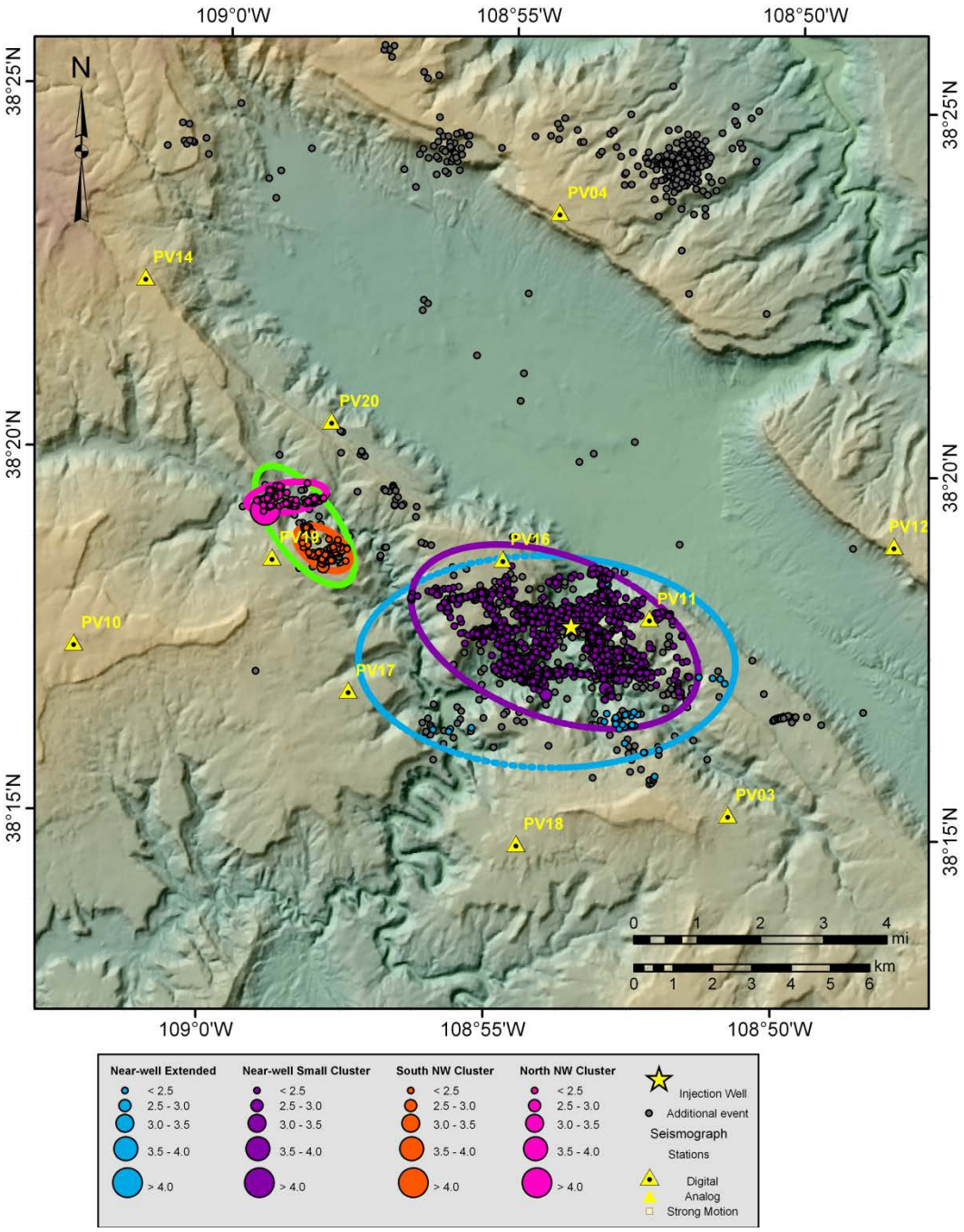

Figure 3-5. Map showing the surface projections of the minimum ellipsoids fitting the near-well and NW clusters. The near-well data is modeled with two data sets: (1) all events within the near-well area (blue); and (2) events selected to be in the highest-density areas (purple). The northwest cluster events are treated in three data sets: (1) all events (green); (2) NW cluster - north sub-cluster (magenta); and, (3) NW cluster – south sub-cluster (orange).

Selected clusters of events for this analysis are shown in map view on Figure 3-5. Two clusters were defined for the near-well seismicity: (1) all events located within the near-well region; and, (2) selected events that don't include small sub-clusters in the southwest and southeast directions. For the NW cluster, two sub-

clusters were defined. In addition, all events within these two sub-clusters were considered as a single cluster. Once the clusters were defined, we computed minimum ellipsoids containing the cumulative seismicity, by year.

We estimate the evolution over time of the stimulated volumes of rock containing the near-well and NW clusters of induced seismicity. These volumes are determined by finding the minimum ellipsoids containing the cumulative hypocenters, by year, within each cluster. A plot of the volumes of the minimum ellipsoids is shown in Figure 3-6. This plot also shows the cumulative volume of brine injected.

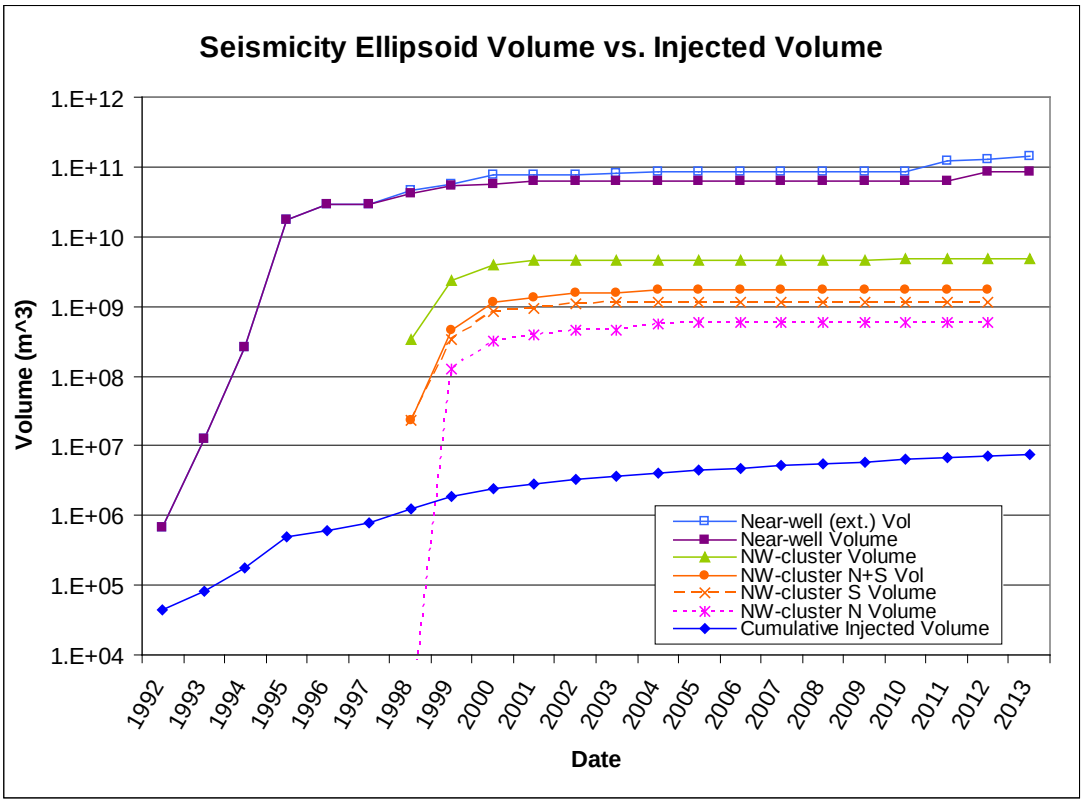

Figure 3-6. Evolution of seismicity ellipsoids for alternative selections of hypocenters representing the near-well and the NW clusters (colors correspond to the ellipsoids shown in map view on Figure 3-5). Cumulative volume of injected brine is also shown.

The results shown in Figure 3-6 indicate that the near-well and NW-cluster seismicity clouds initially grew rapidly in volume (as measured by the computed ellipsoids), followed by much longer periods of very slow growth. Expansion of the near-well seismicity volume occurred most rapidly during the injection tests (1991 – 1995), slowed during the early phase of continuous injection (1996-2000), and then nearly halted after the injection flow rate was decreased in 2000. Beginning in about 2011, the near-well seismicity volume began to again grow slowly. The volume trend for the NW cluster (and its sub-clusters) is similar to that for the near-well region, although delayed in time due to the distance of the earthquakes from the injection well.

During the periods of time following the initial rapid expansion of volume, earthquakes continued to occur within each of the seismicity clouds. These events have served essentially to "fill-in" the enclosing volume without significantly increasing its overall size. After the initial expansion, earthquakes were either occurring in the same locations as previous events, on different parts of previously-active faults, or on newly-active faults elsewhere within the same volume. Hence, although the enclosing volume of stimulated rock appears to have stabilized, the seismicity distribution occurring within this volume has become more complex over time rather than tending towards uniformity.

The volume of the NW cluster seismicity cloud is much less than the near-well seismicity cloud. Considering the NW cluster as a single ellipsoid, its volume is about 7% of the volume of the near-well seismicity volume. Considering the NW cluster as two sub-clusters, the sum of the volumes of the sub-clusters is about 3% of the near-well volume. One hypothesis for the cause of the NW cluster seismicity is that it represents the terminus of a high-permeability zone (or perhaps a series of interconnected zones) that connects with the well (Ake and others, 2005).

3.2 Seismicity Rates and Magnitude Distribution

Seismic hazard is determined by the rates at which earthquakes capable of producing damage occur in proximity to sites of interest. These rates can be expressed in terms of an overall rate of occurrence of earthquakes equal to or greater than some minimum magnitude $M_{\min}$, and the magnitude probability distribution function, which defines the relative likelihood of earthquakes occurring at different magnitudes ($\geq M_{\min}$). This separation is useful in seismic hazard analysis of naturally-occurring earthquakes because larger-magnitude earthquakes tend to occur much less frequently then smaller-magnitude quakes, making their rates difficult or impossible to determine from direct observations of historical seismicity. In contrast, smaller-magnitude earthquakes tend to occur much more frequently, with the relative proportion of small to large-magnitude earthquakes typically following an exponential or "Gutenberg-Richter" distribution. The parameters defining the magnitude distribution can be determined from the smaller-magnitude earthquakes, thus providing a means for indirectly estimating the rates of the infrequent, larger-magnitude events.

The magnitude distribution of induced seismicity may not necessarily follow that of naturally-occurring earthquakes, since the overall seismicity rate depends on the injection history in a complicated way. For induced seismicity, both the occurrence rate and the magnitude probability distribution may have a strong time dependence. In the following sections, we examine the observed seismicity rates and magnitude distributions of induced seismicity at PVU.

3.2.1 Seismicity Rates

The cumulative seismicity rate (over all magnitudes) is a critical parameter in seismic hazard investigations. Given a specified probability distribution of earthquake magnitudes, the higher the total rate of seismicity, the more frequently that large, potentially damaging earthquakes are expected to occur.

The rate of PVU-induced seismicity for $M_D \geq 0.5$ has varied significantly over time, as shown in Figure 3-7. This plot shows the number of shallow earthquakes recorded per quarter during PVU injection operations, all of which we assume to be induced. Only earthquakes with magnitude 0.5 or greater are included in the plot. Seismicity rates are shown for earthquakes occurring at 3 distance ranges from the injection well: up to 5 km, 5 to 10 km, and greater than 10 km. The number of $M_D \geq 0.5$ earthquakes per quarter has varied from 0 to more than 250. In general, the highest seismicity rates occurred early during injection operations (prior to 2000), with lower rates occurring in the last 12 years. However, a very high seismicity rate (over 220 events per quarter) occurred relatively recently, when a swarm of seismic activity occurred in the northern valley area during the last quarter of 2010.

The temporal patterns in seismicity rate also differ from region to region. The near-well region (≤ 5 km distance) shows a large variation in rate. Seismicity rates in this region also show some correlation with injection parameters (Block and Wood, 2009; Block and Wood, 2010). Seismicity rates at distances of 5 to 10 km from the well show much less temporal variation in rate than the near-well region. Seismicity rates in these areas also show much less correlation with injection operations. Shallow, likely-induced earthquakes occurring at greater than 10 km distance from the well have historically had very low seismicity rates. However, rates spiked in late 2010 and early 2011 when several swarms of higher seismic activity occurred.

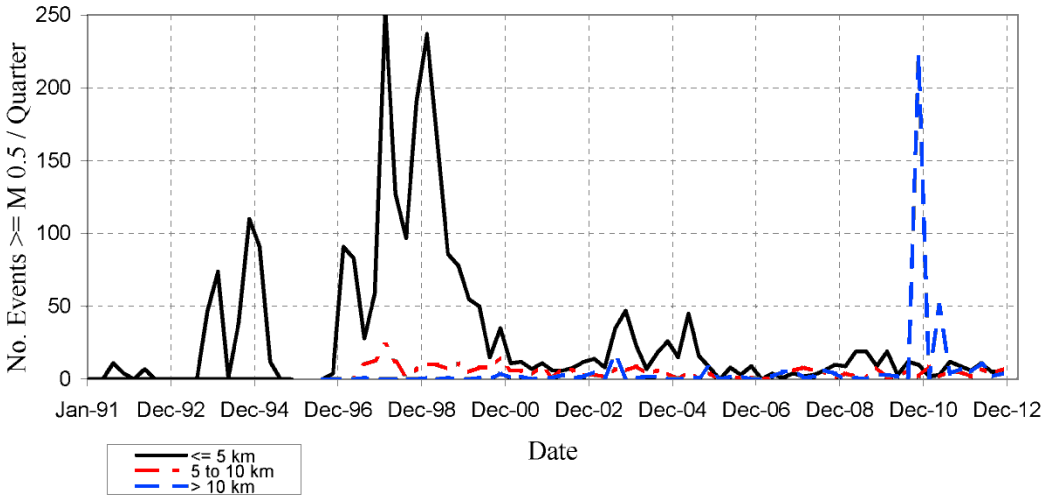

Figure 3-7. Seismicity rates as a function of time for earthquakes occurring at distances of less than 5 km, 5 to 10 km, and greater than 10 km from the injection well. Shallow (<= 8.5 km depth), likely-induced earthquakes with magnitude of M 0.5 or greater are included.

3.2.2 Gutenberg-Richter Magnitude Distribution

In order to estimate the frequency of occurrence of large-magnitude earthquakes, given an estimate of the cumulative seismicity rate, the earthquake probability distribution over magnitude must be determined. This distribution quantifies the relative numbers of earthquakes occurring as a function of magnitude. Earthquake frequency-magnitude distributions for naturally-occurring earthquakes are often characterized using the Gutenberg-Richter (GR) relation (Gutenberg and Richter, 1954), which can be expressed as (e.g., Bender, 1983):

$$\begin{aligned} \lambda_{Cumulative} &= 10^{a-bM} && \text{for } M \in \left[M_i \pm \Delta M/2\right] \\ \lambda_{Incremental} &= \left(10^{b\Delta M/2} - 10^{-b\Delta M/2}\right)\cdot 10^{a-bM_i} && \text{for } M \in \left[M_i \pm \Delta M/2\right] \end{aligned} \quad (3.1)$$

where $\lambda_{Cumulative}$ represents the mean rate at which earthquakes of magnitude M or greater occur, $\lambda_{Incremental}$ represents the mean rate at which earthquakes within magnitude bin M_i of width ΔM occur, and a and b are constants. The GR relation has been applied to induced seismicity in many areas (e.g., Shapiro and others, 2007; Shapiro and Dinske, 2009; Shapiro and others, 2010; Bachmann and others, 2011; Shapiro and others, 2011; Convertito and others, 2012; Barth and others, 2013; Mena and others, 2013). Unlike tectonic earthquake applications, these applications of the GR relation to induced seismicity have mostly been done without declustering of the earthquake catalog.

For tectonic earthquakes, the simple GR relation typically is modified to account for a minimum magnitude of significance (or detection) $M_{\min}$, and a maximum

magnitude of occurrence $M_{\max}$ (e.g., Cornell and Vanmarcke, 1969; Anderson, 1979; Molnar, 1979; Berrill and Davis, 1980; Anderson and Luco, 1983):

$$\lambda_{Cumulative} = \begin{cases} \lambda_a \equiv 10^a \cdot \left(10^{-bM_{\min}} - 10^{-bM_{\max}}\right) & for\ M \le M_{\min} \\ 10^a \cdot \left(10^{-bM} - 10^{-bM_{\max}}\right) & for\ M_{\min} < M \le M_{\max} \\ 0 & for\ M > M_{\max} \end{cases} \qquad (3.2)$$

$$\lambda_{Incremental} = \begin{cases} \left(10^{b\Delta M/2} - 10^{-b\Delta M/2}\right) \cdot 10^{a-bM_i} & for\ M \in \left[M_i \pm \Delta M/2\right] \\ 0 & for\ M < M_{\min}, M > M_{\max} \end{cases}$$

where λ_a represents the cumulative event rate for $M \ge M_{\min}$.

The corresponding complimentary cumulative probability for magnitude, $P^C(M)$, is therefore a truncated exponential distribution. This and its associated probability density function $p_m(M)$ can be written in terms of the GR parameters as follows (Bender, 1983):

$$P^C(M) = \begin{cases} 1 & for\ M \le M_{\min} \\ \dfrac{1 - e^{-\beta(M - M_{\min})}}{1 - e^{-\beta(M_{\max} - M_{\min})}} & for\ M_{\min} < M \le M_{\max} \\ 0 & for\ M > M_{\max} \end{cases} \qquad (3.3)$$

$$p_m(M) = -\frac{dP^C(M)}{dM} = \begin{cases} \dfrac{\beta e^{-\beta(M - M_{\min})}}{1 - e^{-\beta(M_{\max} - M_{\min})}} & for\ M_{\min} < M \le M_{\max} \\ 0 & otherwise \end{cases}$$

where $\beta = b \ln 10$. With this definition, the mean earthquake rates in Equation (3.2) can be rewritten in terms of the GR magnitude probability densities:

$$\begin{aligned} \lambda_{Cumulative} &= \lambda_a P^C(M) \\ \lambda_{Incremental} &= \lambda_a \frac{\left(e^{\beta\Delta m/2} - e^{-\beta\Delta m/2}\right)}{\beta} p_m(M) \end{aligned} \qquad (3.4)$$

B-values for earthquakes observed within the near-well and NW-cluster areas were estimated using three methods. The first method simply computes *b*-values from the logarithm of the ratios of the cumulative number of earthquakes at two magnitudes $M_1 < M_2$, where M_1 and M_2 are chosen from inspection of the data so that the GR is approximately valid for $M \ge M_1$. Similar approaches have been used elsewhere (e.g., Frohlich, 1989; Frohlich and Davis, 1993). Neglecting the effect of $M_{\max}$, this method yields:

$$b \approx \log_{10}\left[N_{Cumulative}\left(M_1\right) / N_{Cumulative}\left(M_2\right)\right] \tag{3.5}$$

where the total number of events of magnitude M or greater occurring in time T is given by $N_{Cumulative}\left(M\right) = N\left(m \geq M\right) = \lambda_a\left(m \geq M\right) \cdot T$. Because of the limited range of magnitudes available in the PVSN data, we chose $M_2 = M_1 + 1.0$ for a range of M_1 values greater than an assumed $M_{\min}$ of 0.5. The time windows used to compute $N(M)$ are the same for each magnitude, and various time windows were tried.

The second method uses the maximum-likelihood estimate for the simple Gutterberg-Richter relation, which neglects the effect of $M_{\max}$ (e.g., Aki, 1965; Utsu, 1966):

$$b = \log_{10} e \Big/ \left(\bar{M} - M_{\min}\right) \tag{3.6}$$

where $\bar{M}$ is the average of the observed magnitudes $\bar{M} = \sum_{i=1}^{N} M_i \Big/ N$ for $M_i \geq M_{\min}$.

Lastly, we employ a maximum-likelihood method which corrects for both magnitude binning and $M_{\max}$ (Bender, 1983):

$$\frac{q}{1-q} - \frac{nq^n}{1-q^n} = \sum_{i=1}^{n} \frac{(i-1)k_i}{N} \tag{3.7}$$

where $q = \exp(-\beta \Delta m)$, n is the number of magnitude bin intervals, and k_i is the number of earthquakes in a magnitude bin. The minimum and maximum magnitudes are implicit in this formulation, and the *b*-values are solved for numerically.

The error in estimated *b*-value can be estimated using two methods that do not have significant biases from binned magnitudes (Marzocchi and Sandri, 2003). Following the work of Shi and Bolt (1982):

$$\sigma_b = \log(10) b^2 \sqrt{\sum_{i=1}^{N} \frac{\left(M_i - \bar{M}\right)^2}{N\left(N-1\right)}} \tag{3.8}$$

Following the work of Tinti and Mulargia (1987):

$$\sigma_b = \frac{1-p}{\log(10)\Delta m\sqrt{Np}}; \quad p = \left(1 + \frac{\Delta m}{\overline{M} - M_{\min}}\right) \tag{3.9}$$

When using the simple ratio method, we computed *b*-values using 5 sets of minimum magnitude pairs (M_1, M_2): (0.7, 1.7); (0.8, 1.8); (0.9, 1.9); (1.0, 2.0); and (1.1, 2.1). All 5 of these sets were used for analyzing data from the near-well region. The smallest magnitude pair (0.7, 1.7) was omitted when analyzing the NW-cluster data because of probable slightly higher event detection threshold for areas farther from the well. For both maximum-likelihood methods, $M_{\min}$ values of 0.7, 0.8, 0.9, 1.0, and 1.1 were used for the near-well region, and values of 0.8, 0.9, 1.0, and 1.1 were used for the NW cluster. For the purpose of comparing results from the corrected maximum likelihood method to those from the other two methods, M_{max} was initially set to a value of 10 to have minimal effect. (Results using different values of M_{max} are presented later in this section.)

B-values were computed using each of the three methods using running time windows over the near-well and NW-cluster data, incorporating data from the beginning of continuous injection (July, 1996) through the end of 2012. A window length of 1.5 years was used for the near-well region. Because the seismicity rate is much lower in the NW cluster than in the near-well region, a much longer time window, 3 years, was used to obtain robust *b*-value estimates for that region. *B*-value estimates are not presented for time periods when the seismicity rates are too low to obtain robust estimates.

The two maximum-likelihood methods were also used to compute *b*-values for the seismicity data recorded during the injection tests (1991 to 1995). The ratio method was not used for the injection test data because for the earliest injection tests the number of events induced was too low to produce reliable results using this technique. Seismic data from the first year of injection testing (July, 1991 to May, 1992) were combined into one data set to obtain enough data points for reliable estimation. The data from each of the last three injection tests (October, 1993 to April, 1995) were analyzed separately. A minimum magnitude value of 0.5 was used for these computations, to incorporate more data points.

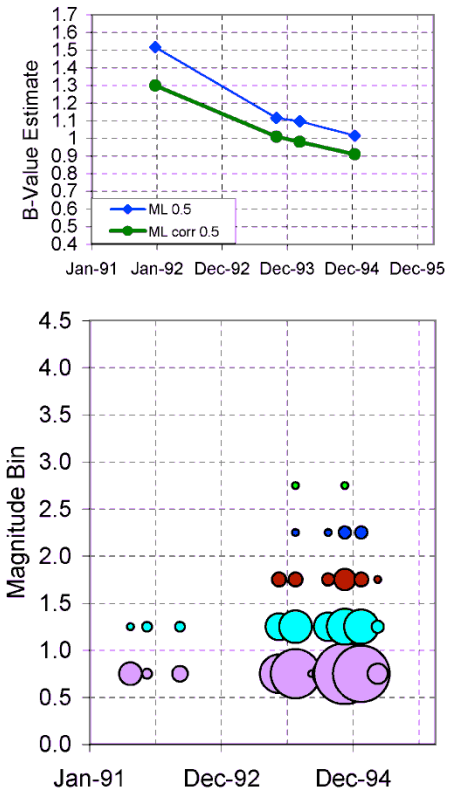

Figure 3-8. *B*-values estimated by two maximum-likelihood methods for the earthquakes induced during the injection tests (1991 – 1995) (upper plot). The lower plot shows the induced earthquakes as a function of date and magnitude; the area of each circle is scaled by the number of earthquakes occurring in a given quarter-year and magnitude bin.

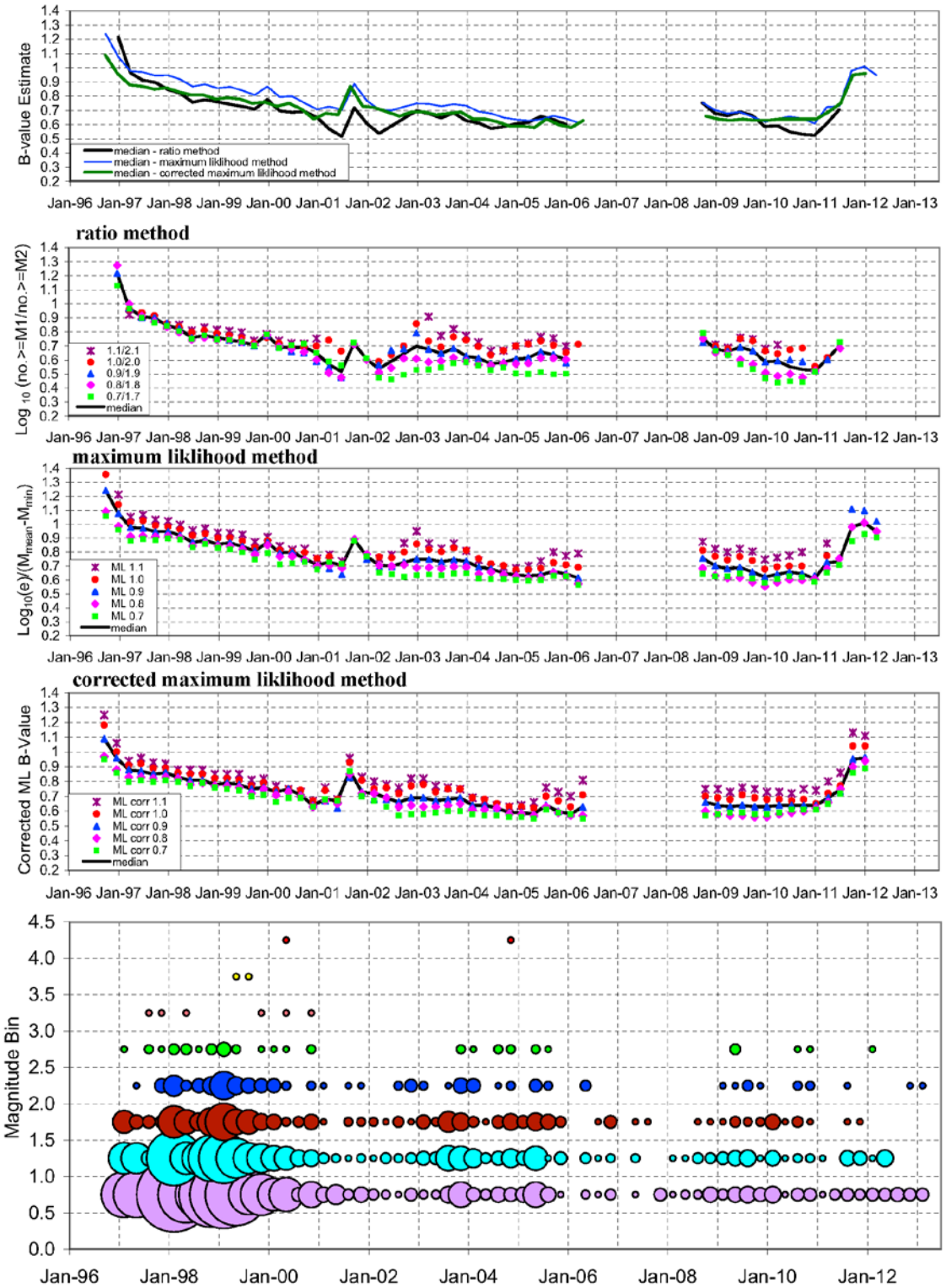

Figure 3-9. *B*-values estimated by three methods for the earthquakes induced in the near-well region (within 5 km of the wellhead) during continuous injection operations (1996 – 2012). The lower plot shows the induced earthquakes as a function of date and magnitude; the area of each circle is scaled by the number of earthquakes occurring in a given quarter-year and magnitude bin.

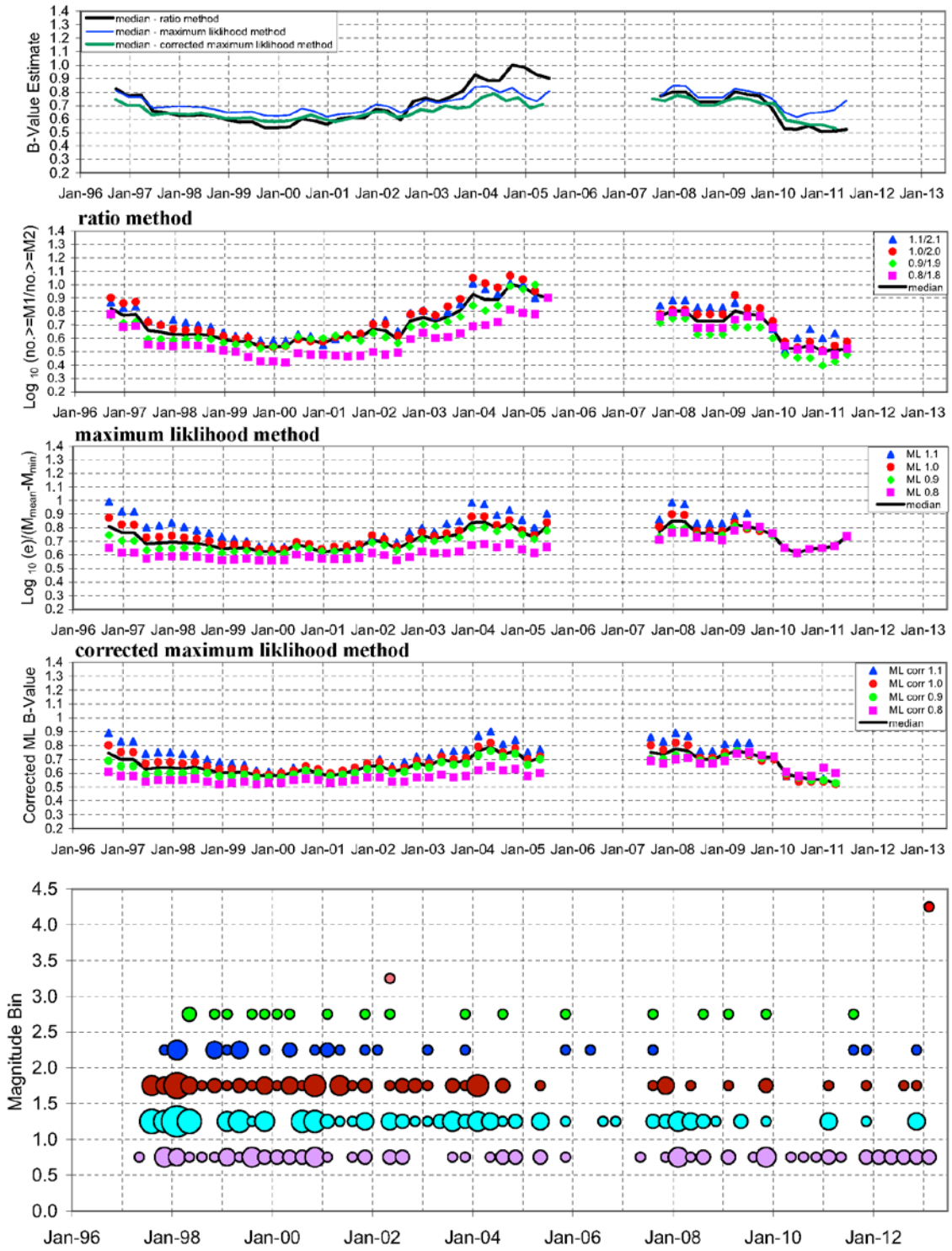

Figure 3-10. *B*-values estimated by three methods for the earthquakes induced in the northwest (NW) cluster during continuous injection operations (1996 – 2012). The lower plot shows the induced earthquakes as a function of date and magnitude; the area of each circle is scaled by the number of earthquakes occurring in a given quarter-year and magnitude bin.

The *b*-values computed for the injection test earthquake data are presented in Figure 3-8, while the results for the period of continuous injection are shown in Figure 3-9 (near-well region) and Figure 3-10 (NW cluster). The uppermost plot in each figure compares the results from the three estimation methods used. The three methods produce fairly consistent results, and show that the *b*-value changes systematically over time.

For the near-well region, *b*-values generally decrease from about 1.3 to 1.5 at the beginning of the injection tests (Figure 3-8) to about 0.6 to 0.7 at the end of 2000, after continuous injection had been underway for several years (Figure 3-9). From 2001 through 2010, the near-well *b*-value estimates are fairly constant, fluctuating mainly between 0.6 and 0.8. Beginning in early 2011, however, the *b*-value estimates show an abrupt increase to about 0.95 to 1.0 by the end of 2011. Since 2011, seismicity rates in the near-well region have been too low to compute robust *b*-value estimates. The abrupt increase in *b*-value in 2011, if valid, would represent a marked change in the long-term trend in the near-well region. It may be too soon to definitively reach such a conclusion, however. Additional data gathered over the coming months and years is needed to confirm this change in *b*-value trend.

B-value estimates for the NW cluster (Figure 3-10) also show temporal variations. As observed for the near-well region, *b*-values in the NW cluster also initially decreased, from about 0.7 to 0.8 when earthquakes first began occurring in the NW cluster, to about 0.55 to 0.65 by the end of 1999. *B*-values then gradually increased, to a maximum of about 0.7 to 1.0 by the end of 2004. Since then, *b*-values have generally decreased, to about 0.5 to 0.7 in 2011. Unlike the near-well region, no abrupt change in *b*-value is observed for recent years, although because of the longer time window used for the analysis (3 years), any shorter-term temporal variations would be smoothed.

Similar temporal variations in *b*-value have been reported elsewhere. For example, Lei and others (2008) reported significant temporal variations in computed b-values for induced seismicity recorded over a period of several years. Their data show decreasing *b*-value over the first 5 to 6 years, from values of about 1.3 – 1.5 to 0.7 - 0.9, followed by a relatively stable period of about 6 to 7 years, similar to the trend seen in the PVU near-well region. Their hypothesis, supported by results of epidemic-type aftershock sequence (ETAS) modeling, is that the variation in *b*-value is related to variation in the relative contributions of fluid-driven (pore pressure-induced) seismicity and stress-triggered aftershock seismicity. According to this model, as the stress level is reduced by induced earthquakes, the ability to trigger aftershocks declines and therefore fluid-driven seismicity becomes more dominant as injection progresses. Variation in the relative contributions of pore pressure-induced and stress-induced earthquakes may also be an important source of the temporal changes in b-values observed at PVU, but to date no analyses have been completed to support the hypothesis for this site.

The value of the maximum possible magnitude, M_{max}, can have a substantial effect on the computed maximum-likelihood *b*-value (Figure 3-11a). The trends in *b*-value, however, remain largely the same. Lower *b*-values are calculated when assumed maximum magnitudes are small (i.e. < 4), however similar *b*-values are computed for $M_{max} \geq 4.5$. A larger difference in the computed *b*-value occurs when the minimum magnitude is changed (Figure 3-11b). This is either the result of an incomplete earthquake catalog, or the fact that Paradox Valley earthquakes may not follow Gutenberg-Richter statistics at lower magnitudes. Further evaluation of the PVSN event detection threshold as a function of time is needed to determine which factor is the primary cause. Due to the difference in *b*-values from distinct M_{min} and M_{max} inputs, a median *b*-value was also computed using a large value of M_{max} (6.0), and M_{min} = 0.8, 0.9, 1.0, and 1.1 (Figure 3-11c). Lastly, the effect of bin window length was investigated (Figure 3-11d). The general trend of decreasing near-well b-value with time holds for all bin windows, and b values remain similar regardless of window length.

a)

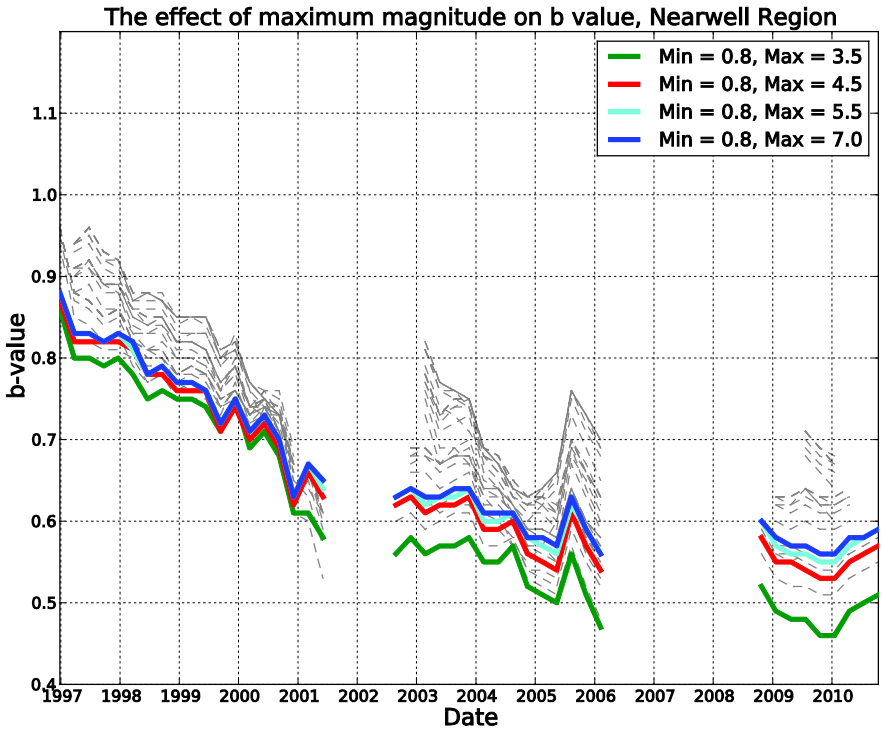
The effect of maximum magnitude on b value, Nearwell Region
Min = 0.8, Max = 3.5
Min = 0.8, Max = 4.5
Min = 0.8, Max = 5.5
Min = 0.8, Max = 7.0
b-value
Date
1.1
1.0
0.9
0.8
0.7
0.6
0.5
0.4
1997 1998 1999 2000 2001 2002 2003 2004 2005 2006 2007 2008 2009 2010

b)

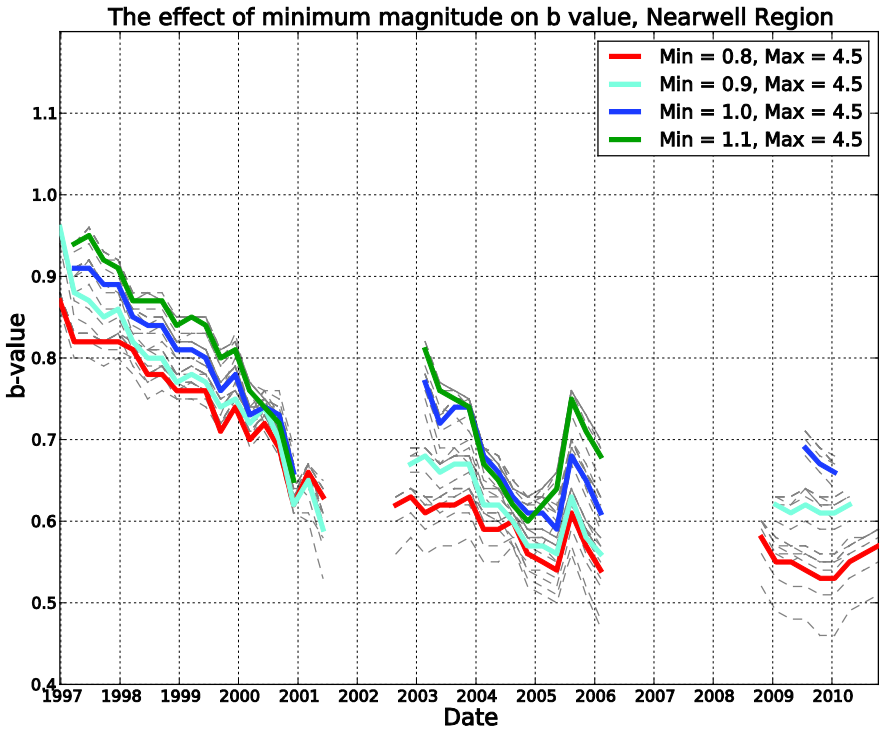
The effect of minimum magnitude on b value, Nearwell Region
Min = 0.8, Max = 4.5
Min = 0.9, Max = 4.5
Min = 1.0, Max = 4.5
Min = 1.1, Max = 4.5
b-value
Date
1.1
1.0
0.9
0.8
0.7
0.6
0.5
0.4
1997 1998 1999 2000 2001 2002 2003 2004 2005 2006 2007 2008 2009 2010

c)

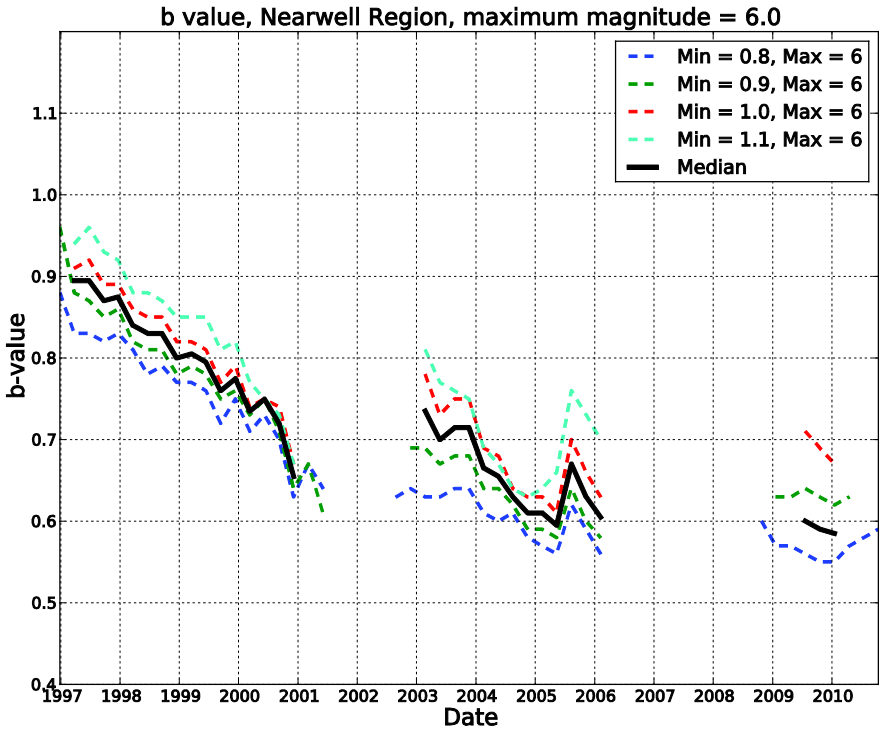

d)

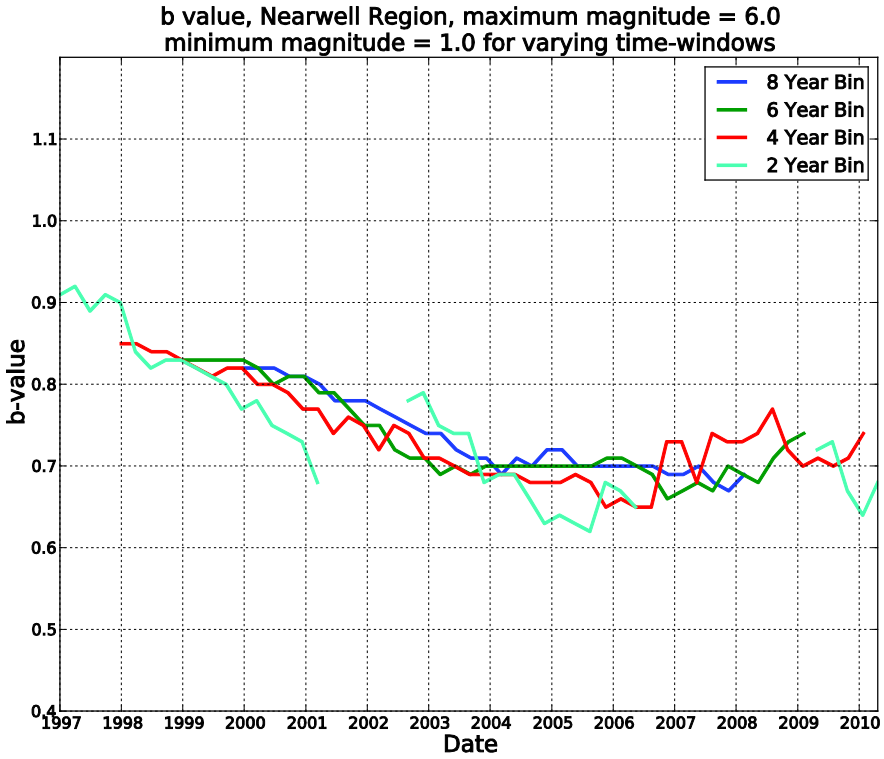

Figure 3-11. (a) The effect on near-well *b*-value estimates when changing the maximum magnitude (Mmax = 3.5, 4.5, 5.5, 7.0) with constant Mmin (0.8), following Bender's (1983) maximum-likelihood calculations. The gray lines show the full range of *b*-values calculated

for a range of Mmin and Mmax values. (b) The effect on near-well *b*-value estimates when changing the minimum magnitude (Mmin = 0.8, 0.9, 1.0, 1.1) with constant Mmax (4.5). (c) The median *b*-value calculated for the near-well region with Mmin = 0.8, 0.9, 1.0, 1.1 and Mmax = 6. This median value was used in seismogenic index calculations. (d) The effect of bin window length for fixed Mmax and Mmin. In all plots, b-values with errors > 0.1 are removed.

In order to further investigate how closely the Paradox Valley catalog follows Gutenberg-Richter statistics, we generated cumulative magnitude-frequency plots for each time interval for which *a*- and *b*-values were calculated. The cumulative data for each time interval were then compared with the corresponding maximum-likelihood magnitude-frequency curves (Figure 3-12 and Figure 3-13).

While the maximum-likelihood curves fit the data over intermediate magnitude ranges, there is a distinct roll-off in the frequency of low and high magnitude earthquakes. The roll off of low magnitude earthquakes varies over time, likely due either to changing event detection capabilities or a discrepancy in the occurrence of low-magnitude earthquakes from Gutenberg-Richter statistics. The roll off of high-magnitude earthquakes is likely due to either an actual $M_{\max}$ effect, or potential saturation of the duration-magnitude scale above about M_D 3.0. In either case, the effect of the high-magnitude roll off has a small effect in maximum-likelihood *b*-value calculations since greater weight is given to the lower-magnitude event counts.

Regardless of the root causes of the magnitude roll-offs, it is clear that the shape of the frequency-magnitude cumulative distribution has evolved over the lifetime of the PVU. While the slope of these plots (*b*-value) has clearly evolved, so has the maximum and minimum magnitude roll-offs. It is also clear that the magnitude-frequency distributions are complex, and have varied over time.

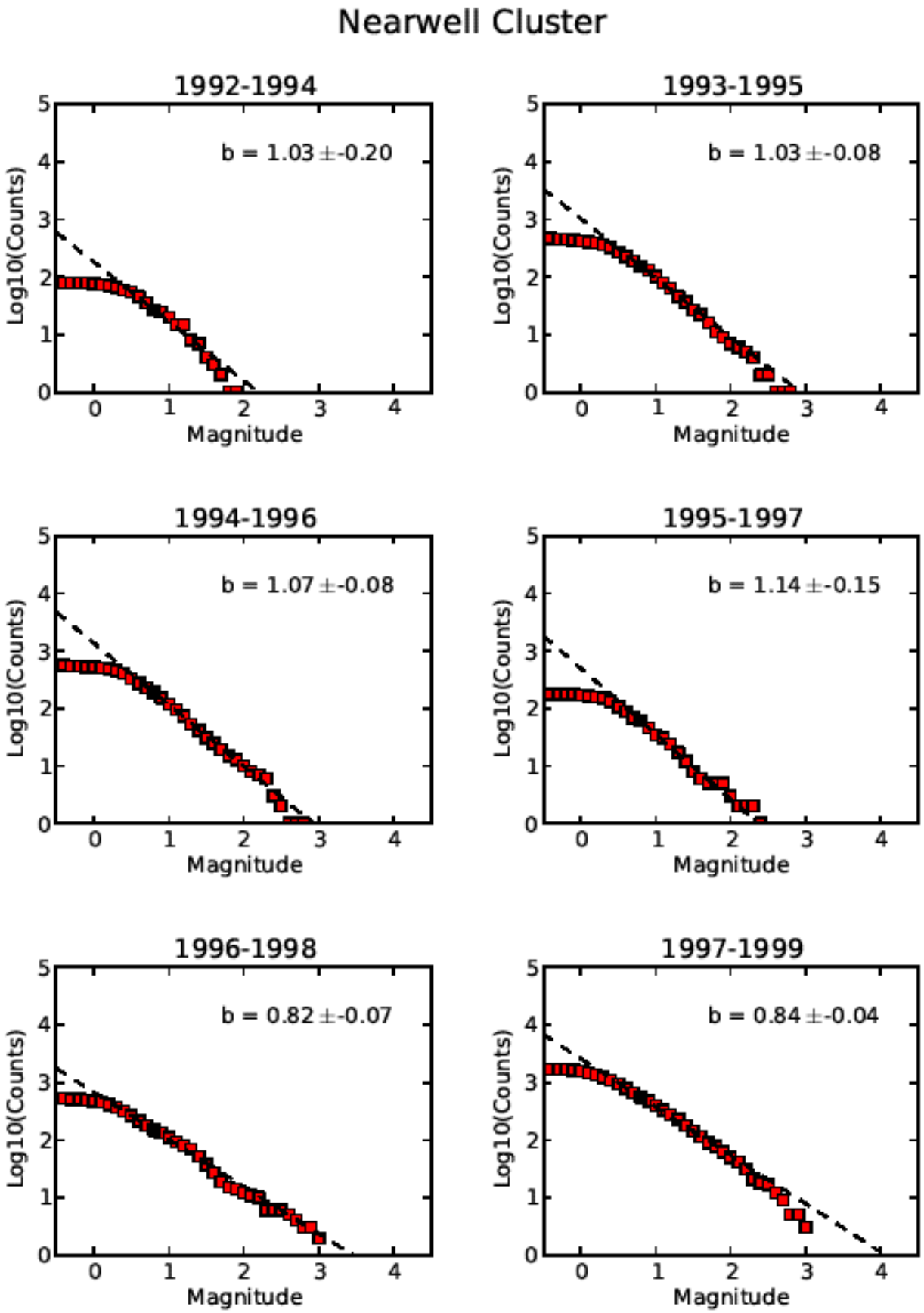
Nearwell Cluster
1992-1994
b = 1.03 ±-0.20
1993-1995
b = 1.03 ±-0.08
1994-1996
b = 1.07 ±-0.08
1995-1997
b = 1.14 ±-0.15
1996-1998
b = 0.82 ±-0.07
1997-1999
b = 0.84 ±-0.04
Log10(Counts)
Magnitude

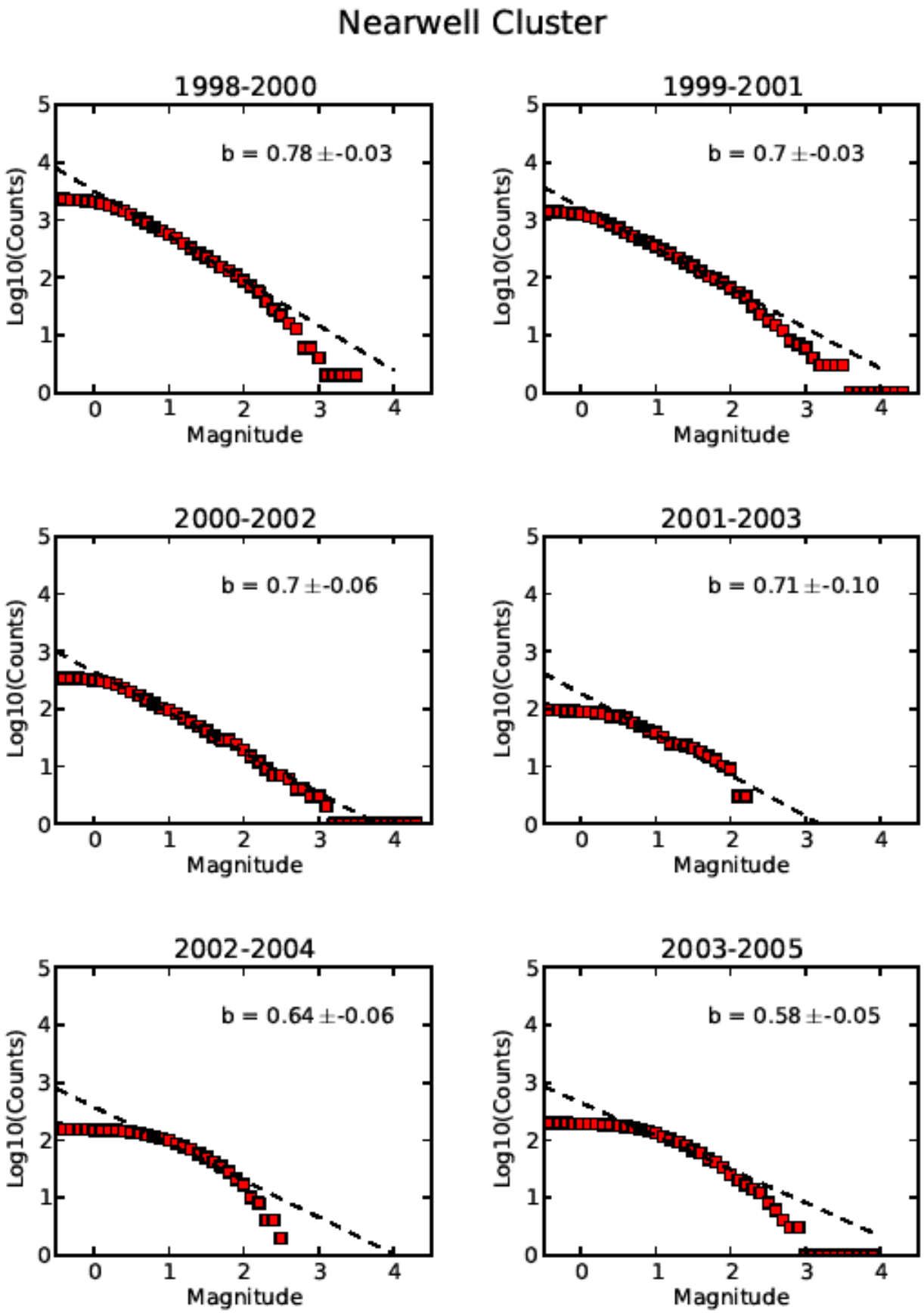
Nearwell Cluster
1998-2000
b = 0.78 ±-0.03
1999-2001
b = 0.7 ±-0.03
2000-2002
b = 0.7 ±-0.06
2001-2003
b = 0.71 ±-0.10
2002-2004
b = 0.64 ±-0.06
2003-2005
b = 0.58 ±-0.05
Log10(Counts)
Magnitude

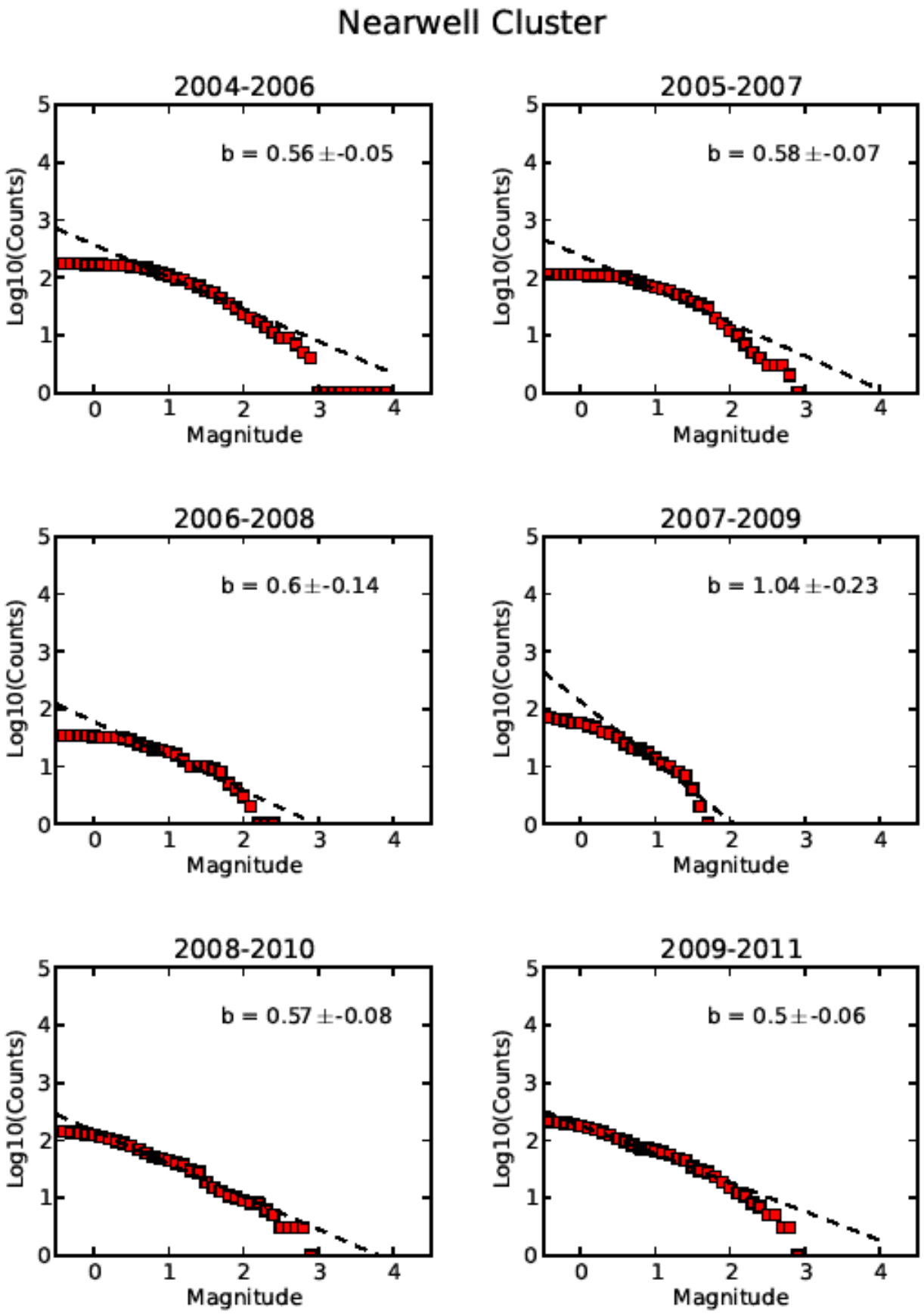
Nearwell Cluster
2004-2006
b = 0.56 ±-0.05
2005-2007
b = 0.58 ±-0.07
2006-2008
b = 0.6 ±-0.14
2007-2009
b = 1.04 ±-0.23
2008-2010
b = 0.57 ±-0.08
2009-2011
b = 0.5 ±-0.06
Log10(Counts)
Magnitude

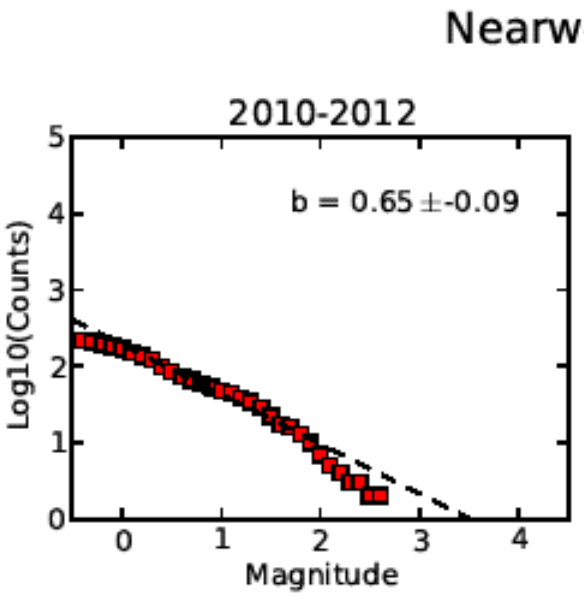

Figure 3-12. Cumulative frequency-magnitude plots for two year windows of near-well events with maximum-likelihood solution (dashed black line) following Bender (1983) (Mmin=0.8, Mmax = 4.3). The *b*-value for each fit is shown in the upper right-hand corner of the plot.

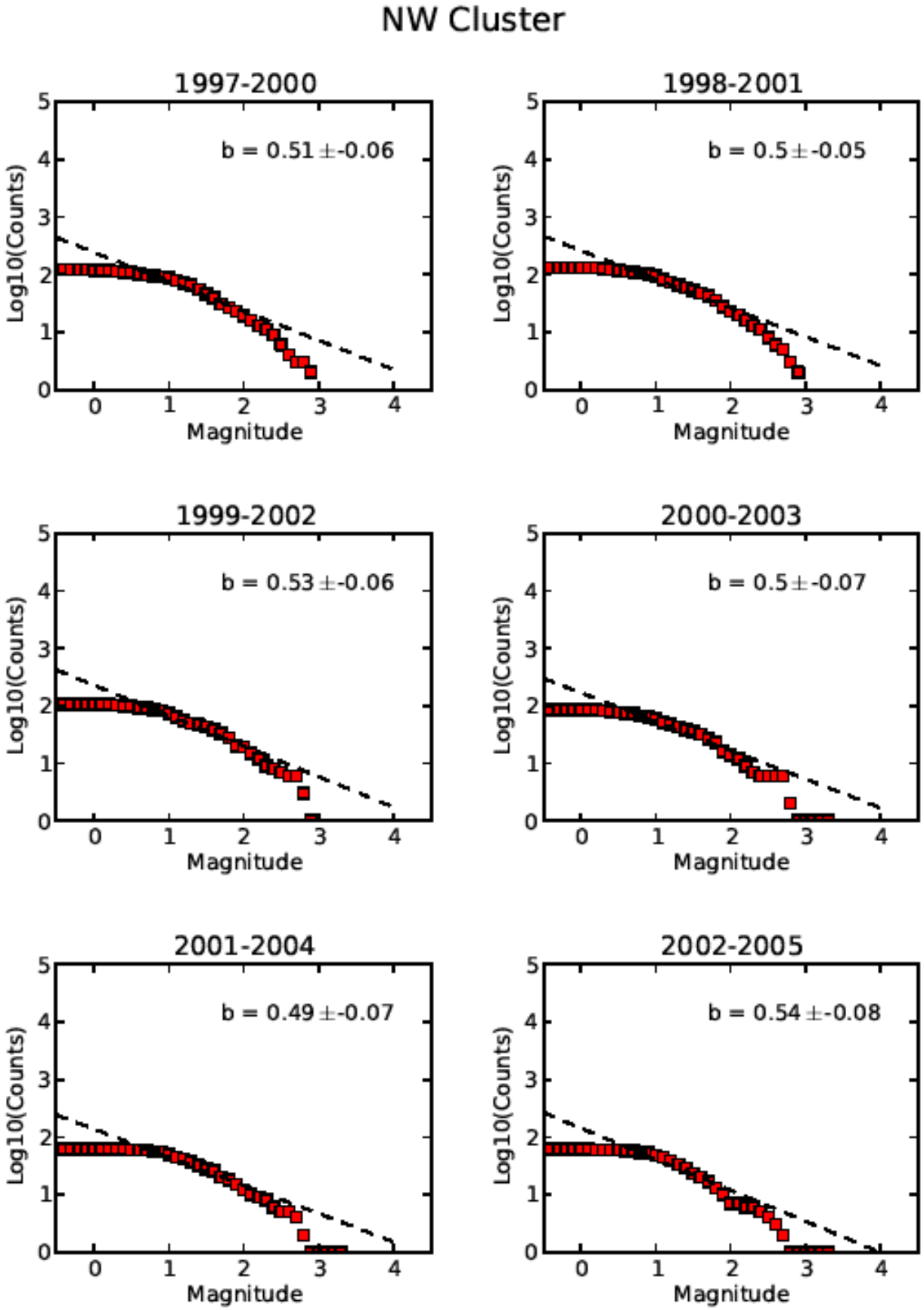
NW Cluster
1997-2000
b = 0.51 ±-0.06
1998-2001
b = 0.5 ±-0.05
1999-2002
b = 0.53 ±-0.06
2000-2003
b = 0.5 ±-0.07
2001-2004
b = 0.49 ±-0.07
2002-2005
b = 0.54 ±-0.08
Log10(Counts)
Magnitude

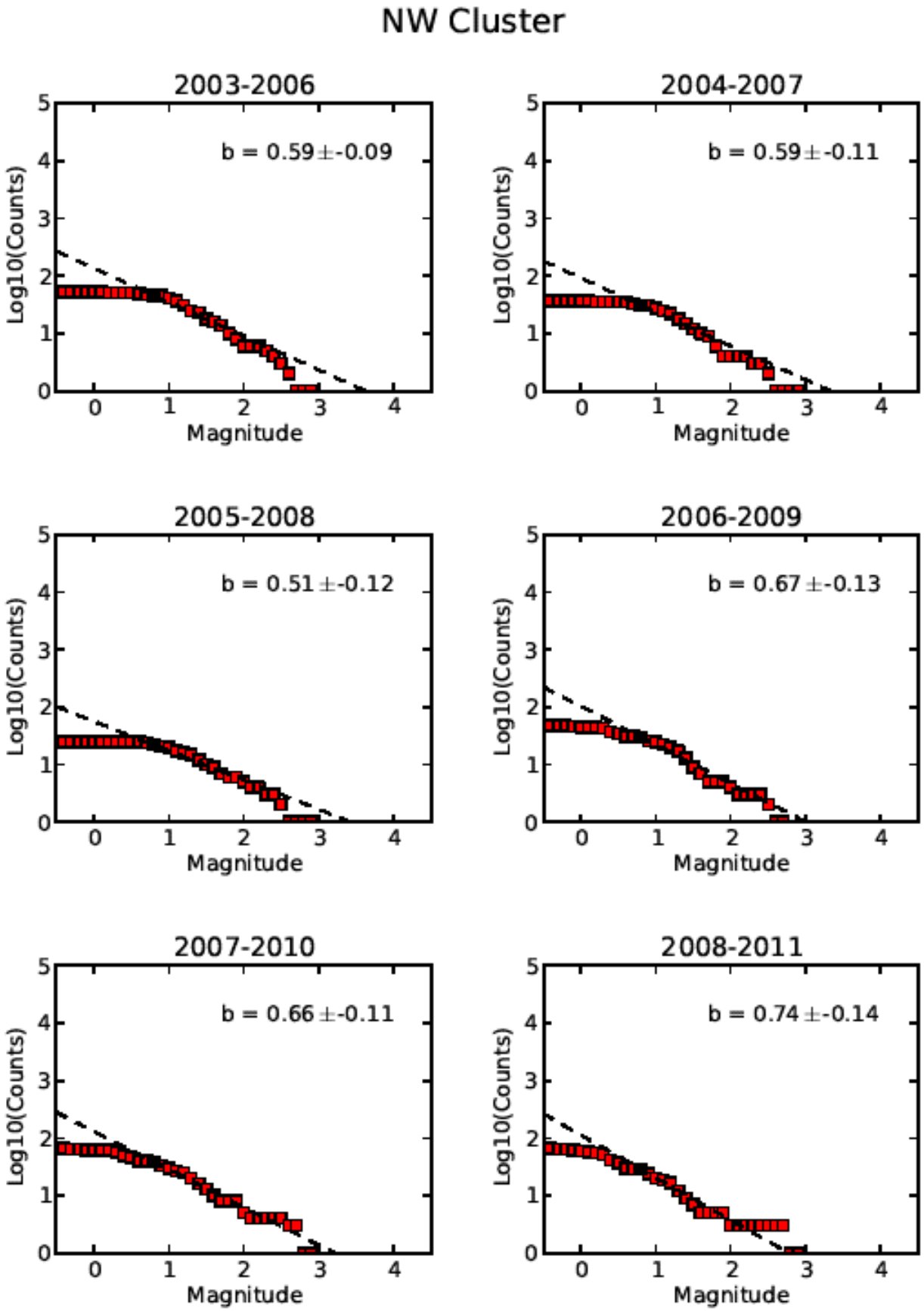
NW Cluster
2003-2006
b = 0.59±-0.09
2004-2007
b = 0.59±-0.11
2005-2008
b = 0.51±-0.12
2006-2009
b = 0.67±-0.13
2007-2010
b = 0.66±-0.11
2008-2011
b = 0.74±-0.14
Log10(Counts)
Magnitude

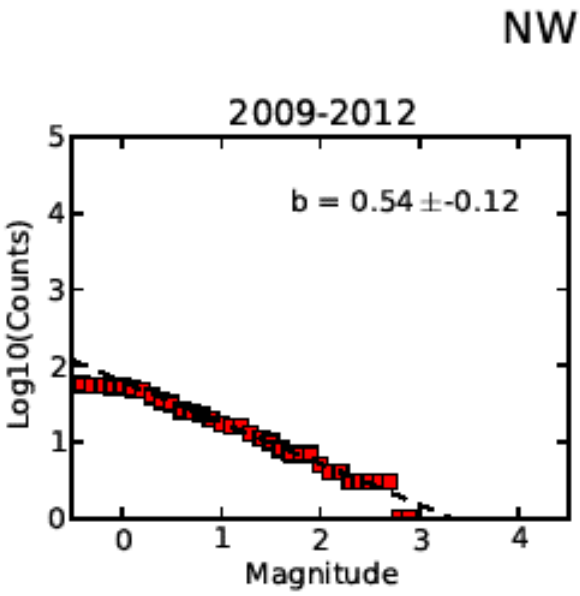

Figure 3-13. Cumulative frequency-magnitude plots for two year windows of north-west cluster events with maximum-likelihood solution (dashed black line) following Bender (1983) (Mmin=0.8, Mmax = 4.3). The *b*-value for each fit is shown in the upper right-hand corner of the plot.

3.2.3 Seismogenic Index

The seismogenic index (Shapiro and others, 2010; Shapiro and others, 2011) provides a decomposition of the cumulative event rate of earthquakes with $M \geq M_{\min}$, denoted $N_a\left(M_{min}, t\right)$, into two parts: (1) a component that depends primarily on the tectonic properties of the injected region; and, (2) a component that depends primarily on the volume injected over some time interval. This decomposition can potentially provide useful estimates of future induced seismicity rates, based on an assumed injection scenario, at least for those injection projects where there is good correlation between the number of induced events during a time interval versus the volume injected during the same interval.

The seismogenic index $\Sigma(t)$ represents the first part of this decomposition, and is designed to depend primarily on properties of the injection site, including: the concentration of pre-existing cracks, the poroelastic storage coefficient, and the maximum critical pore-pressure needed to initiate faulting (Shapiro and others, 2010). The seismogenic index is important to determine for PVU because it provides an indication about whether properties of the injection site have changed over time, and whether the rate of induced earthquakes is well-correlated with the rate of injection. Both of these factors affect whether the rate of future induced earthquakes can be reasonably inferred from injection rates. Determination of the

seismogenic index also allows for comparison of PVU induced seismicity with that of other injection sites, after correcting for differing injection volumes. Following Shapiro and others (2010; 2011), a time-dependent, cumulative seismogenic index can be defined as:

$$\begin{aligned}\Sigma(t) &= \log_{10}\left[N_a\left(M_{min},t\right)/Q(t)\right] \\ &= \log_{10} N_a\left(M_{min},t\right) - \log_{10} Q(t)\end{aligned} \tag{3.10}$$

where t is the elapsed time since the start of injection, $N_a\left(M_{min},t\right)$ is the cumulative number of events of magnitude $M_{\min}$ or larger at time t, as defined in Equation (3.2), and $Q(t)$ is the cumulative injected volume (in units of m^3).

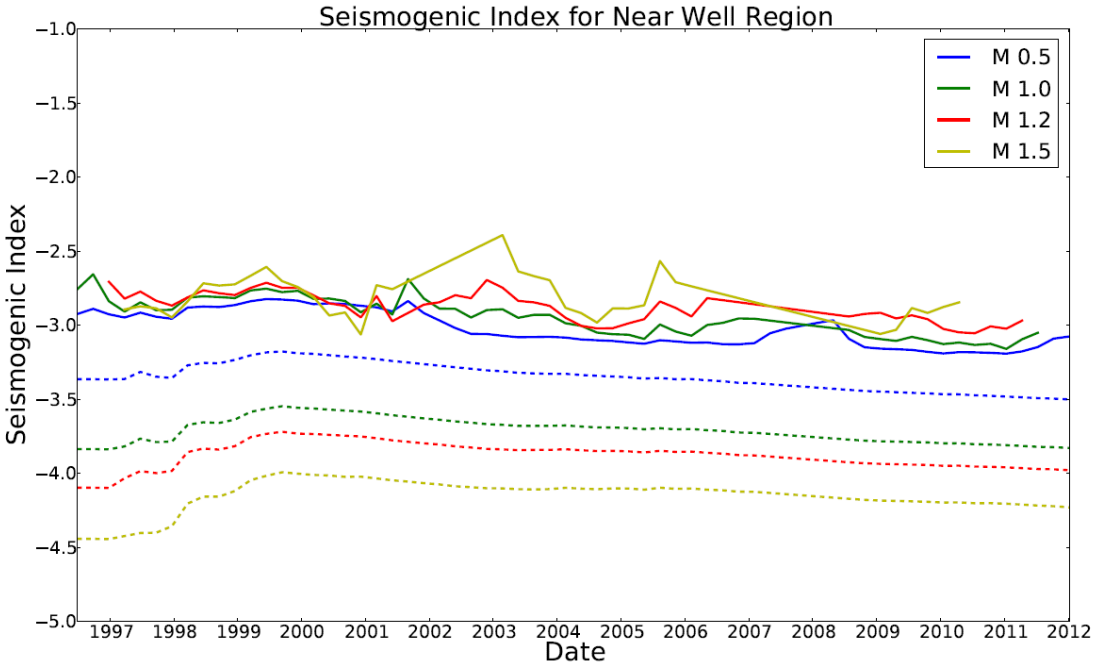

Figure 3-14. Cumulative seismogenic Index $\Sigma(t)$ calculated for the near-well region, for a range of minimum magnitudes $M_{\min}$ ranging between 0.5 and 1.5. Two definitions of cumulative seismogenic index are used: (1) uncorrected for $M_{\min}$ ("simple"), as defined by Equation (3.10) – dashed lines; and, (2) corrected for $M_{\min}$ – solid lines, as defined by Equation (3.11) using the time-dependent *b*-values shown in Figure 3-11c. Because the seismogenic index corrected for $M_{\min}$ depends on the estimated *b*-value, the uncertainty in the estimated *b*-value maps into the computed seismogenic index, leading to considerable fluctuation in the estimate. Time periods where *b*-values have high errors (e.g. the large *b*-value maximum in 2008) have been excluded.

Equation (3.10) decomposes the logarithm of the total event rate into two components by simply subtracting off the cumulative injected volume from the total number of events. Using the simple definition from Equation (3.10), the cumulative seismogenic index was estimated for the near-well region using

possible values of $M_{\min}$ ranging between 0.5 to 1.5. These estimates are shown as the smooth dashed lines in Figure 3-14, and indicate that the cumulative seismogenic index at PVU increased after the start of continuous injection, reached a peak around 2000, and has gradually decreased since that time.

The overall level of the simple seismogenic index defined by Equation (3.10) depends on the value selected for $M_{\min}$, as illustrated in Figure 3-14. This dependence can be removed by subtracting a factor $-b\left(M_{min},t\right)\cdot M_{min}$ from Equation (3.10) to obtain a second definition of seismogenic index that is corrected for $M_{\min}$ (Shapiro and others, 2010):

$$\Sigma\left(t\right)=\log_{10}\left[N_a\left(M_{min},t\right)/Q\left(t\right)\right]+b\left(M_{min},t\right)\cdot M_{min} \qquad (3.11)$$

where $b\left(M_{min},t\right)$ is the time-dependent *b*-value (calculated for a specified $M_{\min}$).

While this second definition attempts to correct for the $M_{\min}$ dependence inherent in the first definition, there is a practical difficulty in computing it: since b is not known exactly, an estimated *b*-value must be used, which may have significant uncertainty that maps into the computed seismogenic index value.

The cumulative seismogenic index defined by Equation (3.11) was calculated for the near-well region using the same values of $M_{\min}$ (0.5 to 1.5) as before, which are shown as the solid lines in Figure 3-14. The resulting curves, while grouped closer together, show considerably more fluctuation over time, which is due to uncertainty in the estimated *b*-value. The overall trends of the cumulative seismogenic index are similar, independent of which definition of seismogenic index is used. Figure 3-14 shows that cumulative Σ has decreased gradually since about 2000. There is a suggestion that the corrected seismogenic index defined by Equation (3.11) has slightly increased since 2011, but this trend results only from a recent change in the estimated *b*-value, and will need to be confirmed by analyzing data collected over the next several years. The uncorrected curves do not show such an increase.

The cumulative seismogenic index defined by Equation (3.11) becomes insensitive to changes over time because it depends on accumulated quantities – both the injected volume and the number of induced events. At PVU, however, the record of induced seismicity response to injection volume appears to show significant variations over time (Block and Wood, 2010), which are not reflected in the cumulative seismogenic index. To examine possible time variations in seismogenic index, we therefore define an instantaneous (and *b*-value corrected) seismogenic index, $\Sigma'\left(t;\Delta t\right)$, for a lag-time Δt, as follows:

$$\Sigma'(t;\Delta t) = \log_{10}\left[\frac{N_a(M_{min},t) - N_a(M_{min},t-\Delta t)}{Q(t)-Q(t-\Delta t)}\right] + \bar{b}(M_{min},t;\Delta t)\cdot M_{min}$$
$$= \log_{10}\left[\frac{\Delta N_a(M_{min},t;\Delta t)}{\Delta Q(t;\Delta t)}\right] + \bar{b}(M_{min},t;\Delta t)\cdot M_{min} \quad (3.12)$$

where $\bar{b}(M_{min},t;\Delta t)$ is the average b-value over the time interval $[t, t+\Delta t]$. Using a time window of 1.5 years, the instantaneous seismogenic index computed for the near-well region is shown in Figure 3-15, along with the cumulative seismogenic index, and for comparison, the logarithms of the constituent event and flow rates, $\Delta N_a(M_{min},t;\Delta t)/\Delta t$ and $\Delta Q(t;\Delta t)/\Delta t$, respectively.

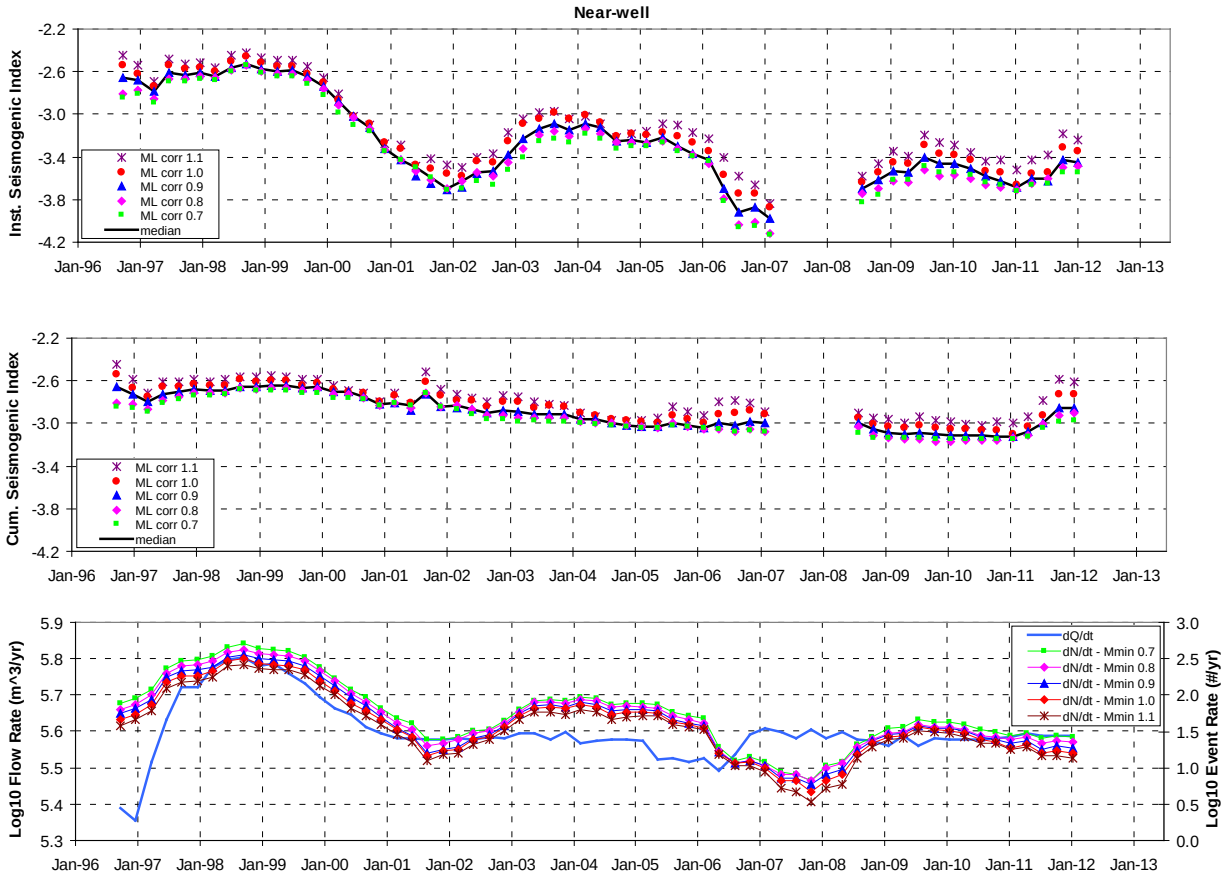

Figure 3-15. Near-well instantaneous (upper) and cumulative (middle) seismogenic index for a range of M_{min} values between 0.7 and 1.1. Each plotted point represents a centered 1.5-year moving average, with points spaced every 90 days. Data points removed for 2007-2008 time interval having a large b-value uncertainty. Lower plot shows a comparison of the logarithm of the average injection rates and event rates, which are well-correlated only until about 2002.

The near-well instantaneous seismogenic index shown in Figure 3-15 suggests that the seismicity response to injection flow rates has varied considerably over time at PVU. After about 2000, the number of events produced per unit volume injected decreased substantially, until about 2002, when it again increased. After 2004, there was another decrease, followed by further fluctuations. The observed large variability over time in seismicity response to injection rates may be due to changing reservoir properties, to a system that is highly sensitive to small changes in conditions, or to a dependence of seismicity rates on other injection parameters, such as pressure. In any case, the large variability makes it very difficult to directly use injection flow rates as the sole indicator of induced seismicity rates.

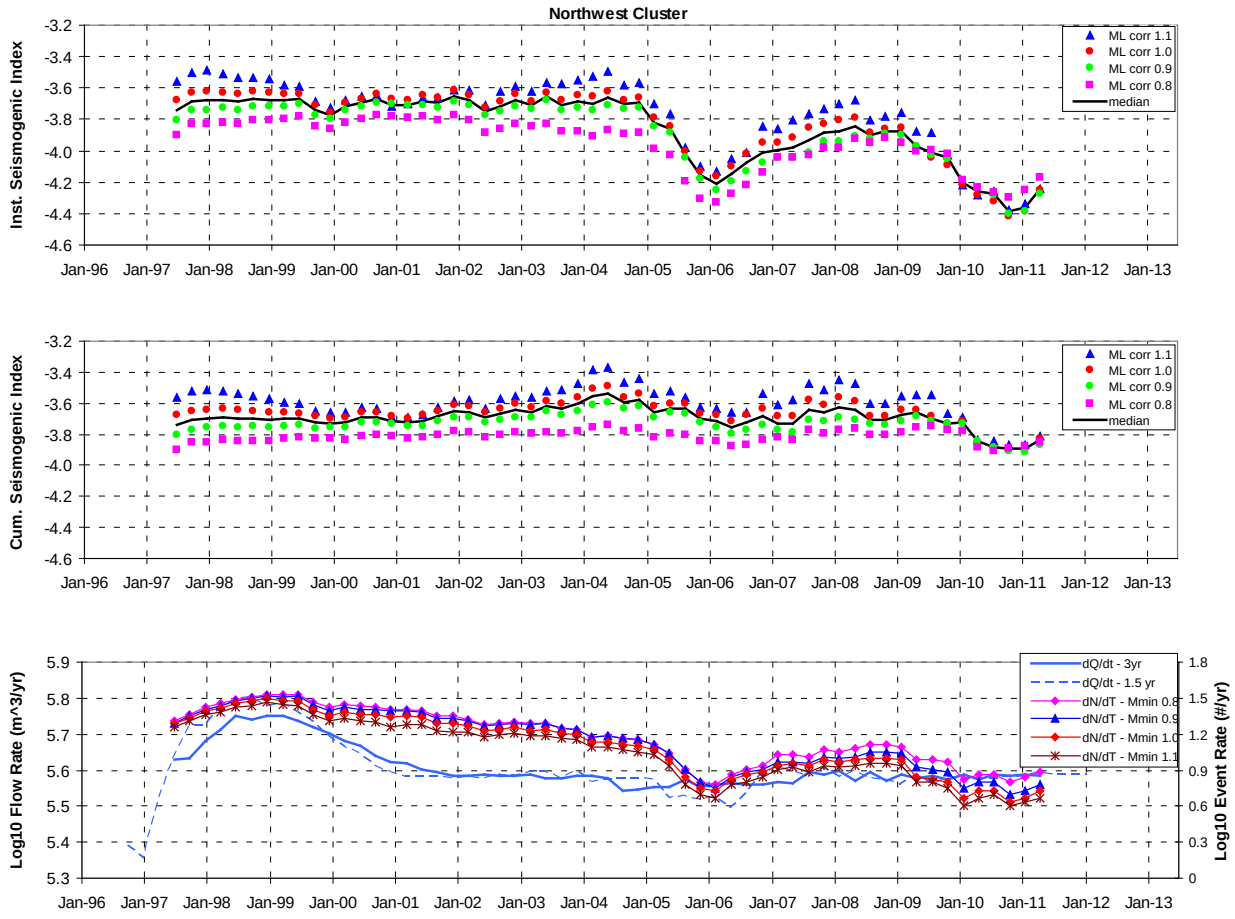

Figure 3-16. Northwest cluster instantaneous (upper) and cumulative (middle) seismogenic index for a range of $M_{\min}$ values between 0.8 and 1.1. Each plotted point represents a centered 3-year moving average, with points spaced every 90 days. Lower plot shows a comparison of the logarithm of the average injection rates and event rates, which are only generally correlated. The 1.5-year-average injection rate from Figure 3-15 is also shown for comparison.

The instantaneous seismogenic index for the NW cluster is shown in Figure 3-16, and is calculated based on the total volume of fluid injected. This plot suggests that the seismicity response to injection at the NW cluster was fairly stable until

about 2005, when it decreased and began to fluctuate. It decreased again from about 2008-2011, and has been increasing since 2011. The proportion of the total injected fluid influencing the NW cluster is not known, nor is it known if that proportion has changed over time. Like the near-well region, the seismicity response to injection rate has been variable over time, and may not provide a reliable indicator of future seismicity rates given an assumed injection rate.

3.3 Maximum Magnitude of Induced Earthquakes

The maximum possible magnitude of induced earthquakes at Paradox Valley has a significant effect on the likely seismic hazard resulting from injection operations, since strong ground shaking tends to increase with increasing earthquake magnitude. Maximum magnitude in turn depends on several key factors, such as the total volume and average rate of injected brine, the location and characteristics of preexisting fractures, and the far-field ambient stress. We examine several methods that have been used for estimating the maximum magnitude of induced earthquakes at other injection sites.

3.3.1 Geometrical scaling of maximum magnitude

Shapiro and others (2011) observed that the maximum magnitudes of induced seismicity appear to be related to the size of the observed cloud of induced seismicity. In their simplified model, the observed seismicity cloud is assumed to provide a working approximation to the current total volume of rock stimulated by injection. Potential fault rupture surfaces for induced earthquakes are assumed to be represented by a set of pre-existing circular disks with random orientation, and whose centers are randomly distributed throughout the rock volume. Earthquakes are assumed to be possible on any of these pre-existing fault surfaces once the stimulated volume has grown in size such that an entire fault surface is contained within the stimulated volume. This model is consistent with the assumption that pore pressure perturbations must extend over most of a potential fault surface in order for rupture to propagate. Shapiro and others (2011) analyzed induced seismicity from a number of fluid stimulation sites and found that the geometrical scale of the fluid-stimulated volume seems to control the magnitude of the largest observed earthquake. In particular, they found that the length of the minimum principal axis of the stimulated volume appeared to control maximum rupture size.

For a fault rupture size X (diameter) of a pre-existing fault, Shapiro and others (2011) provide a relationship between earthquake magnitude M and static stress drop $\Delta\sigma$ of the earthquake as follows:

$$M = \log_{10} X^2 + \left(\log_{10} \Delta\sigma - \log_{10} C\right)/1.5 - 6.07 \qquad (3.13)$$

In this relation, C is a constant on the order of one, and all units are metric.

For the case of a circular crack of radius R (which appears to be a reasonable model for induced earthquakes occurring at PVU) the static stress drop $\Delta\sigma$ is related to seismic moment via $\Delta\sigma = \frac{7}{16}\frac{M_0}{R^3}$ (e.g., Brune, 1970, 1971; Kanamori and Anderson, 1975). Using the Hanks and Kanamori (1979) definition of moment magnitude, $\log_{10} M_0 = 1.5M + 9.05$, equation (3.13) may be rewritten

$$M = \log_{10} R^2 + \frac{\log_{10} \Delta\sigma - \log_{10}(7/16) - 9.05}{1.5} \qquad (3.14)$$

where $R = X/2$, and the units of the radius and stress drop are metric. This relation indicates that magnitude scales with the logarithm of rupture area, for the case of constant stress drop, consistent with empirical magnitude versus rupture area relations for natural earthquakes (e.g., Wells and Coppersmith, 1994; Hanks and Bakun, 2002; Ellsworth, 2003; Shaw, 2009).

Plots of estimated maximum magnitude versus time, for the near-well and NW-cluster regions, are shown in Figure 3-17 and Figure 3-18, respectively. Maximum magnitude at a given time is estimated using Equation (3.14), assuming a value of $R(t)$ equal to the semi-minor axis $A_{\min}$ of the minimum ellipsoid for the seismicity cloud (Shapiro and others, 2011) as estimated in Section 3.1.2. As discussed in the next section, to account for uncertainty in stress drops in the near-well area we have considered potential static stress drops between 1 and 20 MPa (10 to 200 bars).

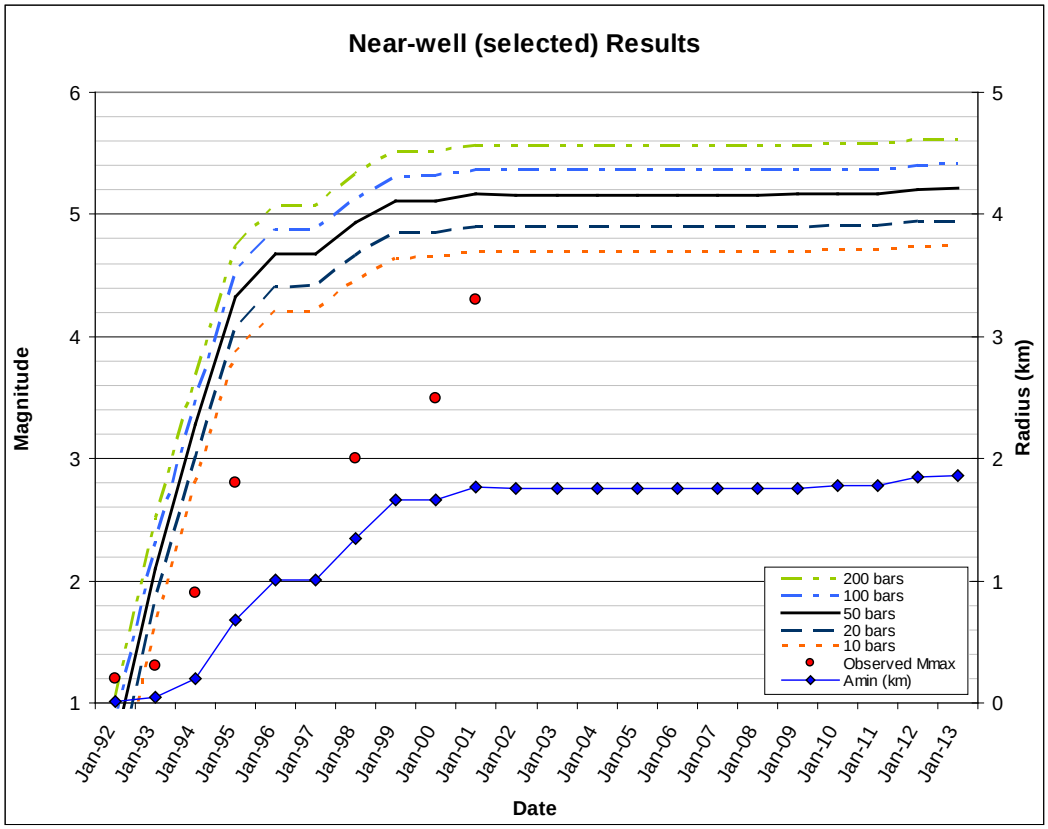

Figure 3-17. Estimated maximum magnitude for the near-well area, computed using the approach of Shapiro and others (2011) for a circular crack and various values of static stress drop. The radius A_{min} of the semi-minor axis of the ellipsoid is shown by the blue curve. Observed maximum magnitudes are shown by red dots.

Considering just the near-well area, and assuming a typical static stress drop of 5 MPa (50 bars), the computed value of maximum magnitude reached M_W 5.2 in 2001, and then remained relatively constant since that time (Figure 3-17). In contrast, the largest observed magnitude in the near-well area was the M_L 4.3 (M_W ~3.8) earthquake of May 27, 2000. Considering just the NW cluster (Figure 3-18), the computed value of maximum magnitude reached M_W 4.4 in 2000, and then remained relatively constant since (assuming a static stress drop of about 50 bars). The largest observed magnitude in the NW cluster was the M_W 4.0 earthquake of January 24, 2013. For both the near-well and NW cluster events, the estimated maximum magnitude is significantly higher than the maximum magnitude observed to date, with the greatest discrepancy in the near-well area. It is not known if this discrepancy is the result of Equation (3.14) not being applicable to PVU seismicity, or if it is more a matter of insufficient time for the maximum magnitude earthquake to occur.

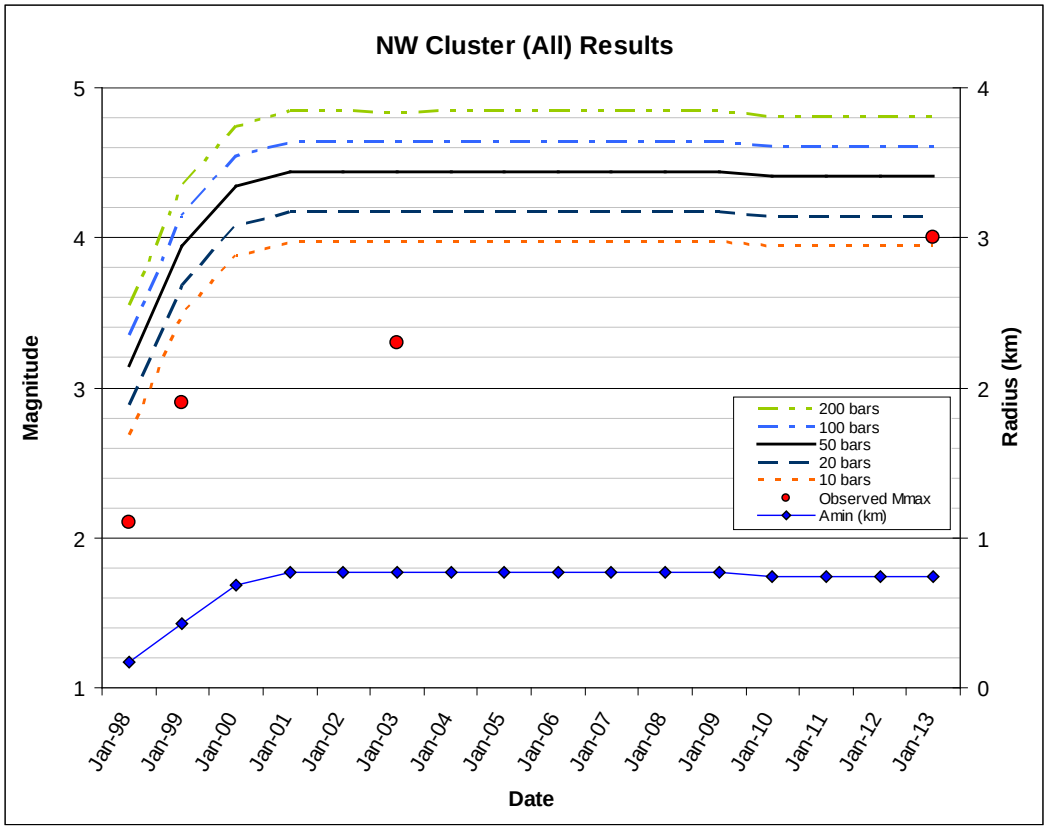

Figure 3-18. Estimated maximum magnitude for the NW-cluster area, computed using the approach of Shapiro and others (2011) for a circular crack and various values of static stress drop. The radius A_{min} of the semi-minor axis of the ellipsoid is shown by the blue curve. Observed maximum magnitudes are shown by red dots.

To use Equation (3.14) to estimate the maximum magnitude of an earthquake generated on a circular fault completely enclosed in a stimulated volume, an assumption must be made about the range of possible stress drops. Using PVSN broad-band data (Section 2.1), the estimated static stress drop for the January, 2013 earthquake was 4.5 MPa (45 bars), and its estimated radius was 0.54 km. Analysis of natural seismicity used to determine magnitude versus area scaling relations indicates that earthquake stress drops are relatively constant, from the smallest to the largest magnitude events (Shaw, 2009). For induced seismicity, however, it is not clear whether the assumption of constant stress drop scaling is appropriate. For example, Goertz-Allmann and others (2011) found an increase in stress drop with radial distance from the injection site, and also found that stress drop correlates with the pore pressure perturbations due to the injection.

We have estimated fault rupture radius versus moment magnitude using Equation (3.14) for static stress drops of 2, 5, and 10 MPa (20, 50 and 100 bars). We have also estimated fault rupture radius (median and ±1 σ) using several empirical area-versus-magnitude relations: WC94-RA: (Wells and Coppersmith, 1994), Els03-RA: (Ellsworth, 2003), Shw09-RA: (Shaw, 2009), as well as the mean of these estimates (equal weight). In using these area-versus-magnitude relations, we have assumed a circular fault geometry. We also estimated fault radius using one

half of the rupture-length-at-depth parameter from WC94-RLD: (Wells and Coppersmith, 1994). Plots of these estimates are shown in Figure 3-19, which suggests a considerable range in allowable rupture radius for a specified magnitude. For example, for a M 5.0 earthquake, allowable radius values using these parameters range between about 1.1 and 2.1 km. This would suggest that the minimum principal axis of the stimulated volume would need to exceed twice this range (i.e., about 2.2 to 4.2 km) in order for an M 5.0 induced earthquake to occur. This condition appears to be met for the near-well cluster of induced seismicity, but not for the NW cluster.

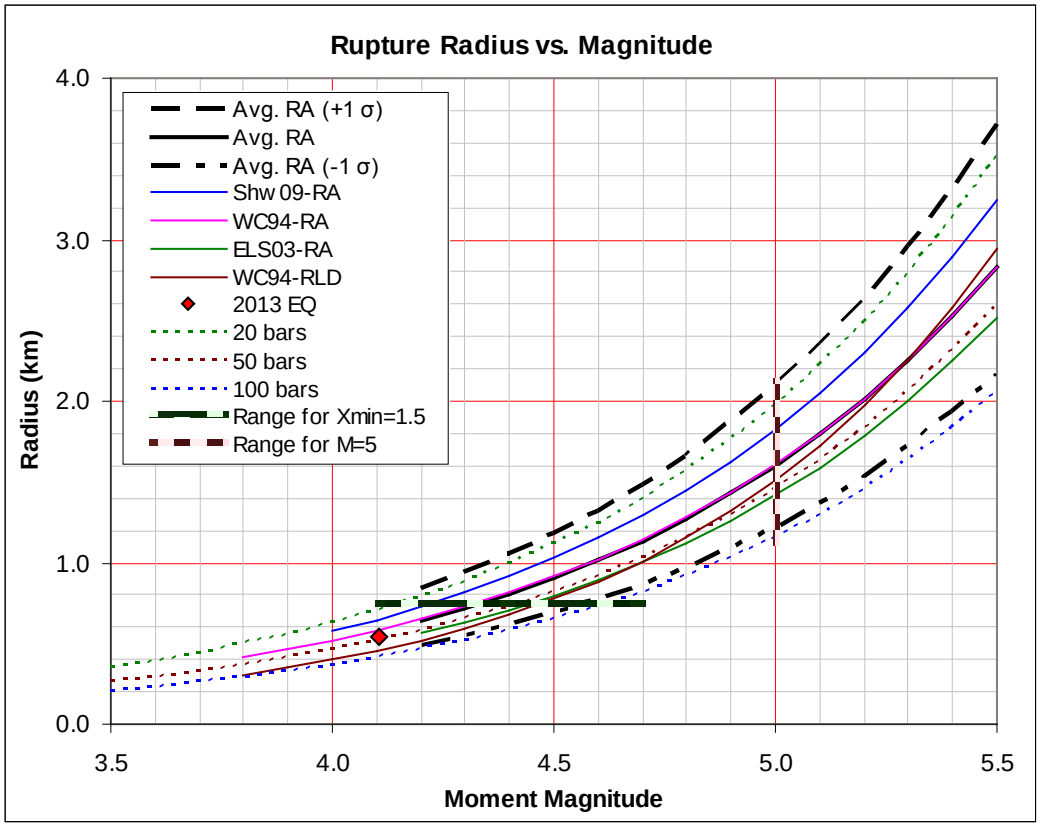

Figure 3-19. Comparison of various measures of fault rupture radius versus moment magnitude for an assumed circular rupture. Solid and dashed lines represent radius estimates using empirical area-versus-magnitude relations – see text for explanation. Dotted lines represent radius estimates using Equation (3.14). The red diamond symbol indicates the PVSN estimate of *M* and *R* for the January, 2013 earthquake. Heavy line patterns indicate: (1) likely range of magnitudes for a maximum radius of 0.75 km (based on the ~1.5 km minimum dimension of the NW cluster); and, (2) likely range of radius values for a M 5.0 earthquake.

For the NW cluster of induced seismicity, the minimum ellipsoid analysis presented in Section 3.1.2 (see Figure 3-5 and Figure 3-6) showed that the dimension of the minimum axis of the seismicity cloud is about 0.7 km (using the north sub-cluster) to about 1.5 km (using the entire NW cluster). To fit a circular fault within this volume, the radius of the fault would need to be about 0.8 km or less, suggesting a maximum magnitude between about M_W 4.1 and 4.7. This range

exceeds the M 3.9-4.1 moment magnitude estimate of the January, 2013 earthquake, but suggests that a significantly larger earthquake (e.g., M 5.0) in the NW cluster would not be expected without a corresponding increase in the size of the stimulated volume to approximately 2.4 km or greater. The dimension of the NW cluster has been fairly stable since 2004 (Figure 3-5). Application of these estimates to Paradox Valley has considerable uncertainty, however, because the model is very simple and relies on a number of assumptions.

3.3.2 Fluid volume scaling of maximum magnitude

A correlation between the cumulative injected fluid volume and maximum-magnitude induced earthquake has been observed at other injection sites (McGarr, 1976; McGarr and others, 2002; Nicol and others, 2011). Such a correlation is also observed at PVU, as shown in Figure 3-20. Each point on the lower plot in Figure 3-20 represents the occurrence of an earthquake having a magnitude larger than all previously-induced earthquakes. All earthquakes within 10 km of the injection well were included in this analysis, but only the last point on the plot (representing the January 24, 2013 M_L 4.4 event) is from an earthquake occurring more than 2.2 km from the injection well.

The PVU maximum observed earthquake magnitudes approximately fit a logarithmic distribution as a function of cumulative injected volume. The least squares fit made to the observed data points is included in Figure 3-20 (solid line), as well as the 95% confidence intervals (dashed lines). Figure 3-21 shows a quantile-quantile (QQ) plot of the residuals of the least-squares fit. The residuals approximate a straight line when plotted against the quantiles of a standard normal distribution, indicating the residuals are normally distributed, and thus that the fit to the data is appropriate.

Since even for naturally occurring earthquakes, the larger-magnitude events occur less frequently than the smaller-magnitude events, the longer the observation time, the more likely it is that a large-magnitude event will be observed. However, for a given time window, the magnitude distribution of earthquakes occurring within that window is usually assumed to be time-independent for naturally-occurring events. In other words, the likelihood of a large-magnitude earthquake occurring early during the observation window is the same as the likelihood that it will be observed late in the window. This is not the case for the PVU-induced seismicity. Rather, the steady increase in earthquake magnitude over time (represented by cumulative volume in Figure 3-20) indicates that during PVU fluid injection, subsurface conditions are changing such that larger-magnitude induced earthquakes become more likely as injection progresses.

The correlation shown in Figure 3-20 indicates a current estimated maximum magnitude of approximately M_L 4.2, based on the cumulative volume of fluid injected to date. This estimate is only slightly less than the observed maximum magnitude of M_L 4.4. The range of uncertainty in the estimated maximum magnitude is about M_L 3.7 to 4.8, based on the 95% confidence intervals.

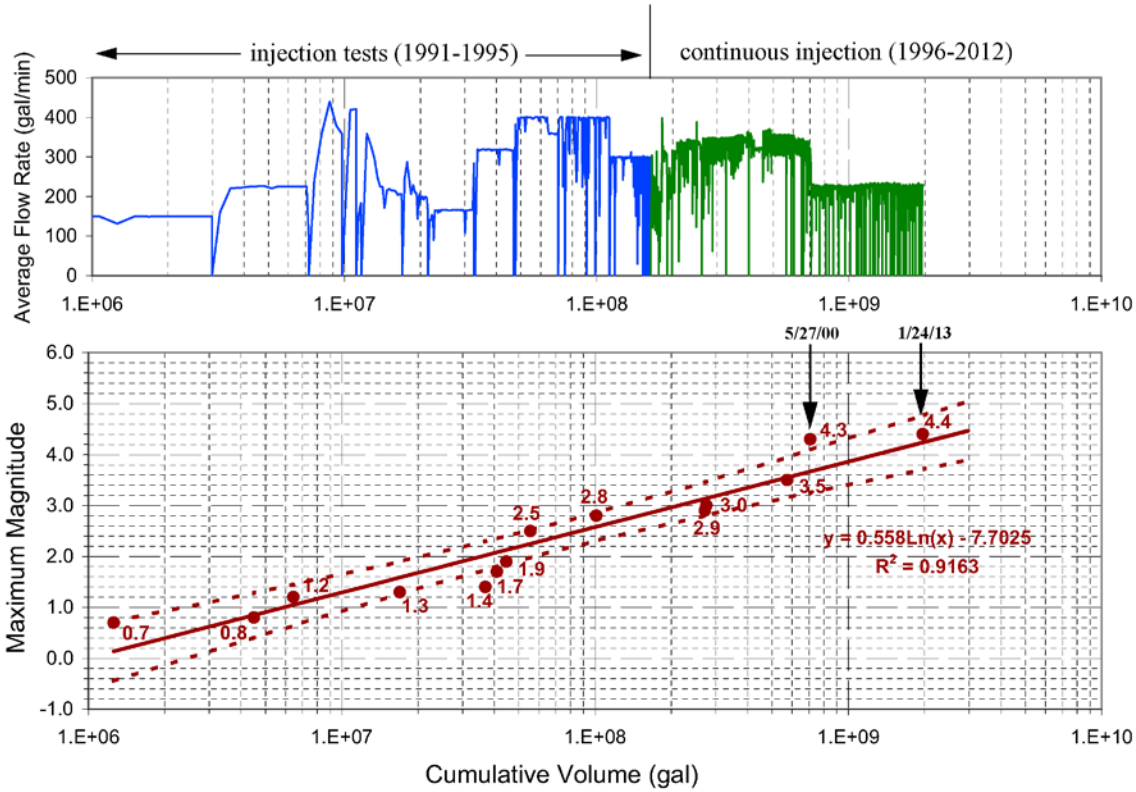

Figure 3-20. Maximum induced earthquake magnitude as a function of (log) cumulative injected fluid volume (lower plot). The solid line is a least squares linear fit to the data. The dashed lines represent 95% confidence intervals. The upper plot shows the daily average injection flow rate as a function of (log) cumulative volume.

Because the volume-magnitude data are plotted in log-linear space in Figure 3-20, time periods early in injection operations have a much greater impact on the plot than later time periods. For example, data from the 5 years of injection tests (1991-1995) are plotted over more than two-thirds of the volume (x) axis, while the subsequent 16 years of continuous injection only cover the last one-third. The last 12 years of injection, since the flow rate was reduced in mid-2000, are represented by only the last two data points on the plot. These last two points represent earthquakes of nearly identical magnitude (the M_L 4.3 event of May, 2000 and the M_L 4.4 event of January, 2013). Because the time span since the injection flow rate was reduced in mid-2000 is represented by such a short segment of the volume-magnitude plot, it is impossible to interpret whether the long-term reduction in flow rate implemented in 2000 has changed the nature of the volume-magnitude correlation. We cannot determine whether the magnitudes are likely to increase at the same rate as a function of injected volume as they did prior to 2000 or whether the rate of magnitude increase has been reduced since 2000.

.

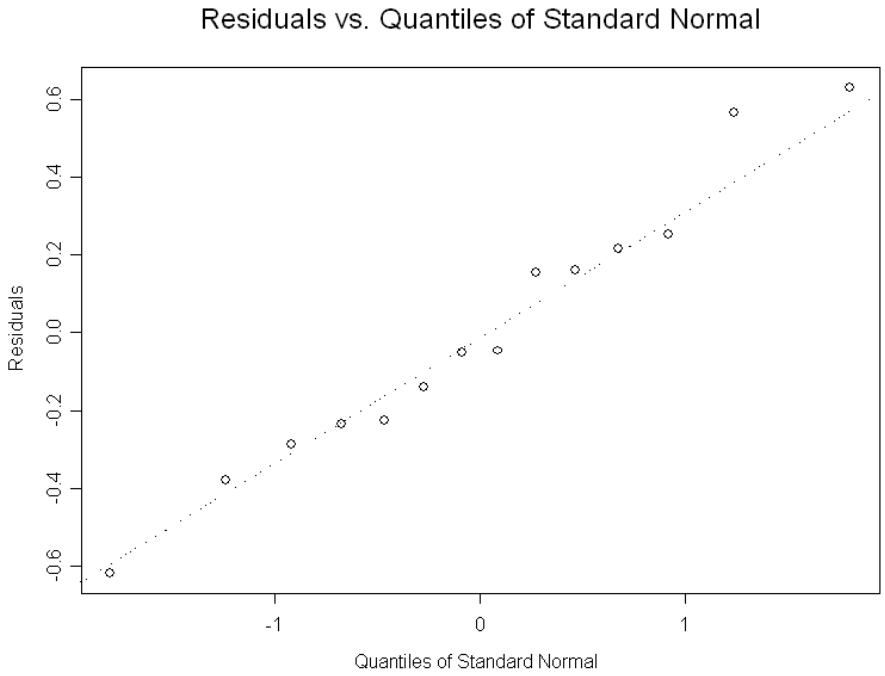

Figure 3-21. Residuals of the least-squares fit to the maximum magnitude versus the log of cumulative injected volume, plotted against the quantiles of standard normal. The linearity of the residuals indicates that they are approximately normally distributed, confirming the validity of the fit shown in Figure 3-20.

A similar relation between maximum magnitude and total fluid volume injected can be seen in Figure 3-22, which summarizes the case histories presented in Nicol and others (2011) and includes a wide range of data from injection sites, as well as extraction and hot dry rock sites. Based on the cumulative volume injected to date at Paradox Valley (7.5×10^6 m^3), the trend line for data incorporating a variety of sites would suggest a mean maximum magnitude of M_W 4.8 for induced earthquakes, with fairly broad 5% and 95% confidence limits of M_W 3.4 and 6.2, respectively. This value of maximum magnitude is significantly greater than that predicted from the Paradox data alone, and the data point for Paradox is also considerably below the trend line.

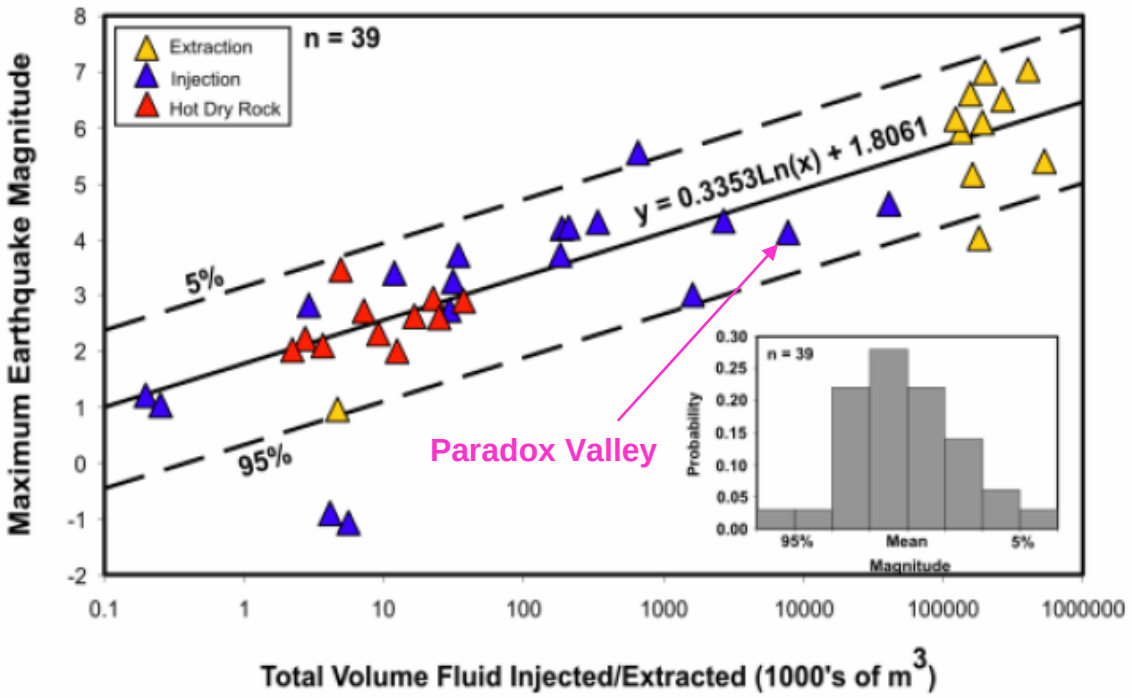

Figure 3-22. Maximum magnitude of induced earthquakes from 39 different sites, from Nicol and others (2011). Data point for Paradox Valley is indicated (although the symbol was plotted for the M_L 4.3 earthquake of May 27, 2000 earthquake, at the scale of the figure it applies equally to the January, 2013 M 4.0 earthquake (injected volume = 7.5×10^6 m^3).

There is much less scatter in the Paradox data (Figure 3-20) than in the fit to the Nicol and others (2011) data from many sites (Figure 3-22), however there are also substantially fewer data points (14 vs. 39). The trend for Paradox data indicates a significantly smaller maximum magnitude (estimated M_L 4.2; observed M_L 4.4) than does the multi-site data.

3.3.3 Effect of Pore Pressure on Earthquake Magnitude

Pore pressures may also affect the magnitudes of induced seismic events. Empirical and theoretical studies suggest that an absolute pore pressure threshold may be needed to trigger large-magnitude events, at least in some cases. Studies also suggest that pore pressure gradients may play a role in the occurrence of large-magnitude induced earthquakes, especially those that occur after injection has ceased.

Empirical PVU data show a general correlation between higher long-term average injection pressures and the occurrence of larger-magnitude earthquakes in the near-well region (within 5 km of the injection well) (Block and Wood, 2009; Block and Wood, 2010). This correlation is shown in the upper two plots of Figure 2-22. The uppermost plot shows injection pressures averaged over different lengths of time, while the middle plot shows the near-well seismicity plotted as a function of date (x axis), earthquake magnitude (y axis), and rate (size

of bubbles). Since we have no means for measuring in-situ pore pressures directly, the long-term averaging of the injection pressures is a simplistic method of accounting for the time delay and amplitude modulation of pressure variations at the injection well as the pressures propagate away from the well. To correlate pressure trends with the seismicity data, the pressure averaging must be done over longer time windows for later periods. The seismicity may take progressively longer to respond to changes in injection pressures both because the seismicity occurs at greater distances from the well for later time periods and because the size and complexity of the reservoir increases over time. While acknowledging that this method is very simplistic, the general correlation between relatively high long-term average injection pressures and increased rates and magnitudes of induced earthquakes in the near-well region suggests that pore pressure affects both the rate and magnitudes of induced seismic events. The lack of near-well induced earthquakes with magnitude greater than 2.5 during periods of time when the long-term average injection pressures are low suggests that a pore pressure threshold must be exceeded to trigger earthquakes of magnitude 2.5 or greater. Recently, Keranen and others (2013) suggested a similar link between the occurrence of large earthquakes in Oklahoma they interpret as injection-induced events and a rise in injection pressure (with a 5-year time delay). The empirical correlation between injection pressures and seismicity for PVU is only observed for earthquakes occurring within 5 km of the PVU injection well; the seismicity occurring at greater distances does not show the same trends (Figure 2-22, lower plot).

Numerical simulations also indicate a correlation between pore pressure and earthquake magnitude. Baisch and others (2010) performed finite element modeling of pressures and induced seismicity for an injection simulation. In their modeling, the largest-magnitude induced earthquakes occurred after the end of injection. While pressures near the simulated wellbore were falling during this time period, pressures were rising along the outer rim of the stimulated area, where the largest-magnitude events occurred. The investigators attribute both the time of occurrence (post-injection) and the location of the largest-magnitude events to shallow spatial gradients of pressure. The post-shut-in pressure rise along the outer rim of the stimulated area has a shallower spatial gradient than the pressure rise that occurs during injection (Figure 3-23). Because of the shallow pressure gradient, many neighboring patches in their model are at a similar level of stress criticality simultaneously. Therefore, only a small amount of stress diffusion is sufficient to cause overcritical conditions over a large area, increasing the likelihood for large-magnitude events. As the authors note, the results of their modeling are consistent with the observation that for many cases of fluid injection, the largest-magnitude events occur during the shut-in period after injection has ceased.

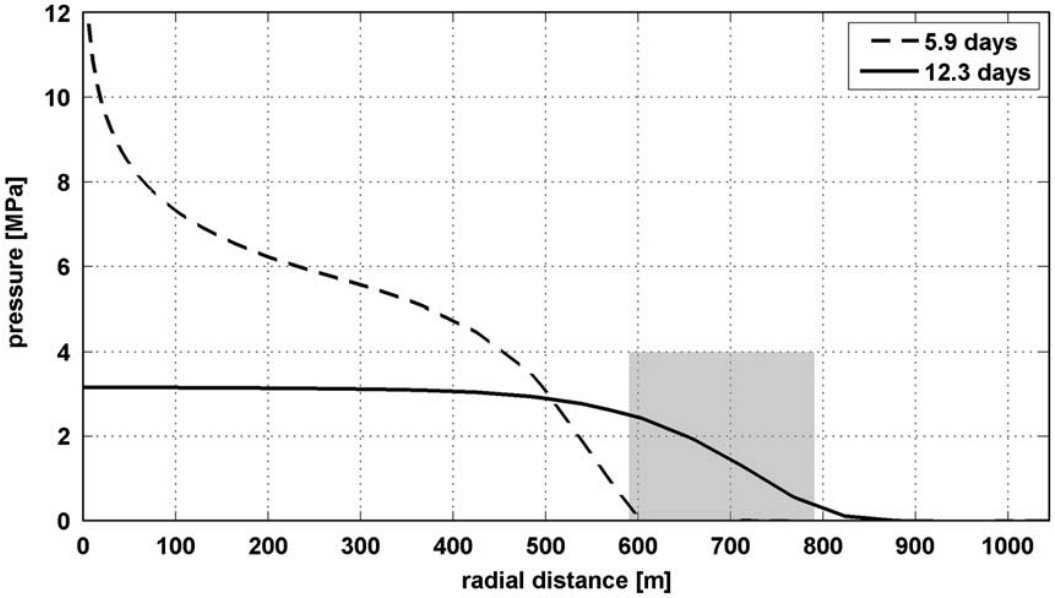

Figure 3-23 Hydraulic overpressures inside a simulated fault zone as a function of radial distance from the injection well at the time of shut-in (dashed line) and 6 days after shut-in, when the largest-magnitude simulated event occurred (solid line). The shaded area marks the patches that slipped during the largest-magnitude event. Figure taken from Baisch and others (2010).

Further insights into the relationship of pore pressure and the occurrence of large-magnitude induced earthquakes come from the work of Garagash and Germanovich (2012). These investigators numerically modeled a pre-stressed fault with a locally peaked, diffusively spreading pore pressure field. They studied the nucleation of dynamic rupture, the rupture run-out distance, and rupture arrest. Their modeling indicates that the largest run-out distances of dynamic slip – corresponding to the largest earthquakes – occur when the pore pressure increases just enough to activate slip on faults that have low shear pre-stress. These are the faults that are not optimally oriented in the background stress field for shear failure. These faults require a larger rise in pore pressure, a larger pressurized region, and a longer nucleation time for slip to occur than the more favorably-oriented faults. Although counterintuitive, the results of this modeling also indicate that as pressure continues to increase to higher values beyond the minimum required for slip activation, the likelihood of inducing large-magnitude earthquakes actually diminishes. This finding is related to mechanisms that act to arrest the nucleation of dynamic rupture under these conditions. In this scenario, then, the occurrence of large-magnitude earthquakes could cease at very high pore pressures and then later resume if injection operations are altered and pore pressures decline.

3.3.4 Maximum magnitude discussion

We have examined only a few of the models presented in the literature. Other models of maximum magnitude include the hypothesis that larger events occur in

places with fully developed, thick faults with cataclasite fault cores. McClure and Horne (2012) developed a degree-of-fault-development factor based on categories of fault development observed on wellbore cores, surface outcrops, and imaging logs. We have not attempted to implement their classification system for Paradox Valley.

3.4 Short-term Earthquake Recurrence Estimates

To estimate seismic hazards arising from PVU induced seismicity, the rate of occurrence of earthquakes with magnitude large enough to potentially cause damage must be determined. Such damage, in turn, depends on earthquake magnitude, distance between the earthquake and the site of interest, faulting type and orientation, site conditions, the fragility of structures throughout the area, and other factors. Insufficient data exists to reliably estimate all (or even most) of these factors. Over the life of the project, both the rates and spatial distribution of induced seismicity have varied considerably, even under conditions of relatively constant average injection rates. Currently, induced seismicity rates do not appear to quickly respond to changes in average injection rate, and we know of no models capable of reliably estimating long-term induced seismicity patterns from historical well-head pressure or injection rate data.

To make a rough estimate of the likelihood of potentially-damaging earthquakes occurring over the next several years, we therefore make the assumption that both injection operations and short-term seismicity rates will not vary greatly from those of the recent past. We select a subset of the observed induced seismicity data, from 2009-2012, to characterize current short-term seismicity rates for both the near-well and NW cluster areas. Gutenberg-Richter *a*- and *b*-values are then calculated from this data using the maximum likelihood method, as described in Section 3.2.2. These results are used to compute a short-term cumulative seismicity rate $\lambda_a\left(m \geq M_{\min}\right)$ assuming no change in average injection rate:

$$\log_{10}\lambda_a\left(m \geq M_{\min}\right) = a + \log_{10}\left(10^{-bM_{\min}} - 10^{-bM_{\max}}\right) \tag{3.15}$$

If instead injection rates may change, then an alternative approach is to use the instantaneous seismogenic index, $\Sigma'\left(t;\Delta t\right)$, defined in Equation (3.12), and computed in Section 3.2.3 for previous time intervals. If the seismogenic index is assumed to remain relatively constant in the short term, and also assumed to be independent of the injection rate, then the short-term seismicity rate under conditions of a change in injection rate can be computed as follows:

$$\begin{aligned}\log_{10}\lambda_a\left(m \geq M_{min}, t;\Delta t\right) &= \Delta N_a\left(M_{min}, t\right)/\Delta t \\ &= \Sigma'\left(t;\Delta t\right) + \log_{10}\overline{q}(t;\Delta t') - \overline{b}\left(M_{min}, t;\Delta t\right)\cdot M_{min}\end{aligned} \tag{3.16}$$

where $\bar{q}(t;\Delta t) = \Delta Q\left(t;\Delta t'\right)\big/\Delta t'$ is the average injection rate assumed for the next time interval $\Delta t'$. However, if the long-term average rate of injection does not change significantly over the next several years of injection, then these results would not differ from those estimated using Equation (3.15).

Once the cumulative seismicity rate $\lambda_a\left(m \geq M_{\min}\right)$ has been estimated, using either Equation (3.15) or Equation (3.16), the cumulative rate of earthquakes with magnitude $m \geq M$ can be obtained using Equation (3.2) as follows:

$$\lambda(m \geq M) = \begin{cases} \lambda_a & for\ M \leq M_{\min} \\ \lambda_a \cdot \dfrac{1-10^{-b(M_{\max}-M)}}{1-10^{-b(M_{\max}-M_{\min})}} & for\ M_{\min} < M < M_{\max} \\ 0 & for\ M \geq M_{\max} \end{cases} \qquad (3.17)$$

where the symbols are the same as in Equation (3.2).

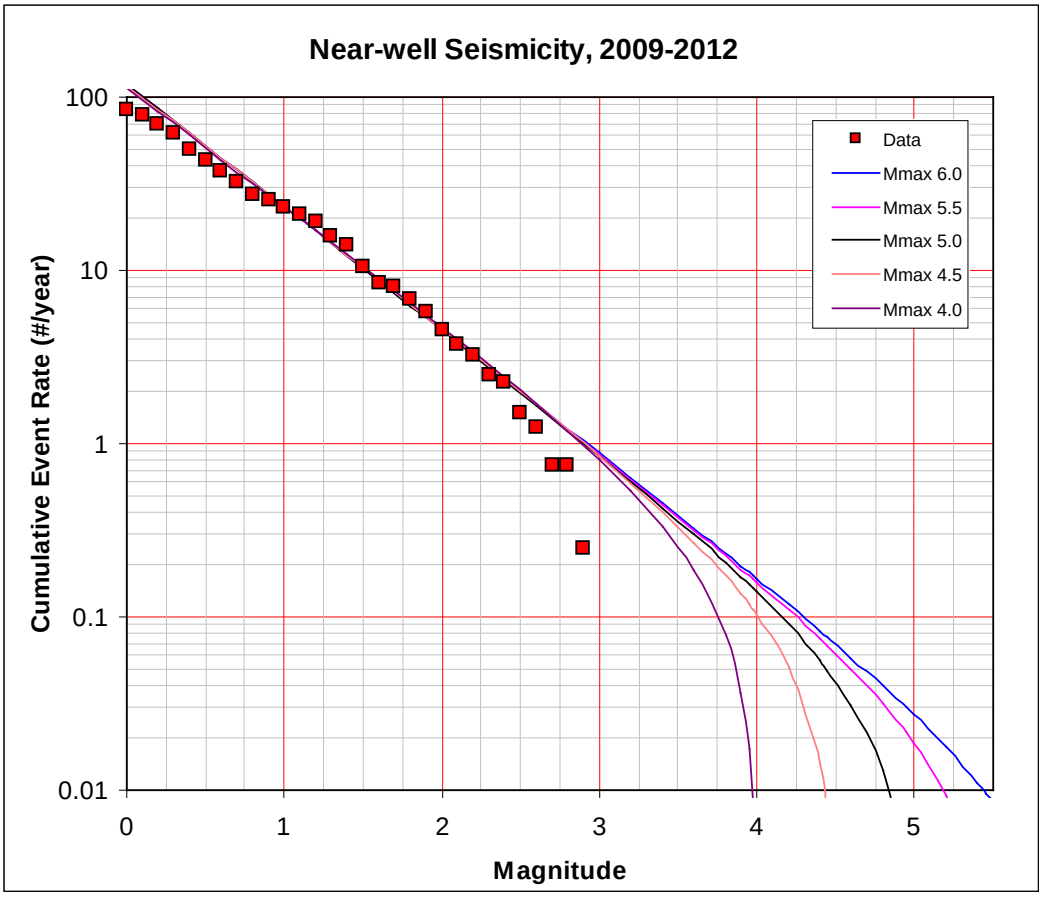

Figure 3-24. Magnitude recurrence data for 2009 through 2012 for the near-well area, with calculated Gutenberg-Richter relation assuming M_{min} = 1.0 and M_{max} = 4.0 through 6.0, in 0.5 magnitude increments.

Figure 3-24 shows the magnitude-recurrence data from the near-well area for the four-year period 2009-2012, along with Gutenberg-Richter fits determined using the maximum-likelihood method and Equation (3.17). Similar data and fits for the NW cluster are shown in Figure 3-25. For both areas, a value of M_{min} = 1.0 was selected, and recurrence estimates were made for M_{max} values ranging between 4.0 and 6.0. Since $M \geq 4.0$ earthquakes have already been observed at PVU, a choice of M_{max} = 4.0 as an upper magnitude limit is inconsistent with the total data set, but is shown in these figures because it visually appears to provide a better fit to the recent data.

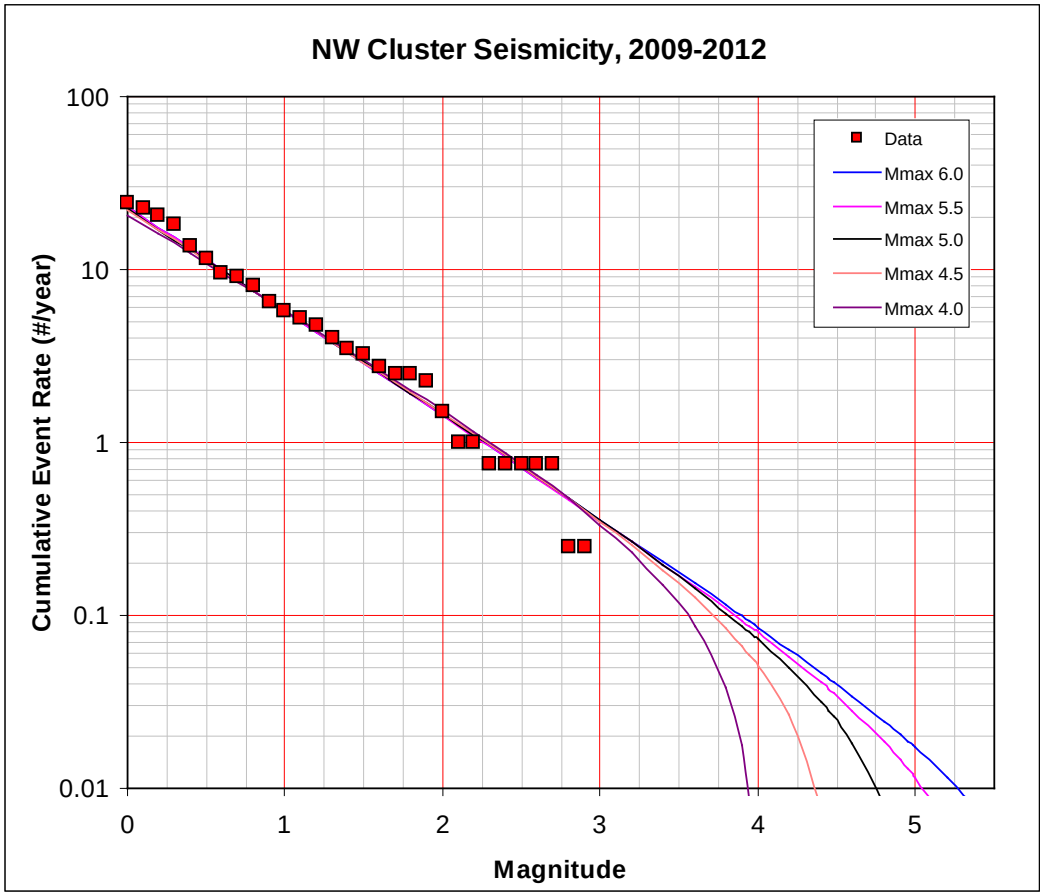

Figure 3-25. Magnitude recurrence data for 2009 through 2012 for the NW cluster area, with calculated Gutenberg-Richter relation assuming M_{min} = 1.0 and M_{max} = 4.0 through 6.0, in 0.5 magnitude increments.

The Gutenberg-Richter fits to the recurrence data overestimate the observed events rates for magnitudes greater than about M 2.5 for any choice of $M_{\min} \geq 4.0$, as illustrated in Figure 3-24 (near-well area) and Figure 3-25 (NW cluster). The discrepancy is greatest for the near-well area. This result is consistent with the poor fit of Gutenberg-Richter models to PVU induced event data seen for most time periods, as discussed in Section 3.2.2. This misfit may be due to factors such as potential saturation of the duration magnitude scale used for

PVU earthquakes, as well as deviation of the PVU data from Gutenberg-Richter statistics. Until the detailed nature of the misfit is determined, the Gutenberg-Richter fits to the data can be treated as a conservative estimate of short-term seismicity rates.

If induced seismicity at PVU is assumed to follow a Poisson process, then the short-term earthquake rates determined from the Gutenberg-Richter fits to the data can be used to estimate a probability of occurrence for earthquakes with a magnitude larger than have been observed in the data. For earthquakes following a Poisson process with a time-independent seismicity rate $\lambda(m \geq M)$, the probability of occurrence of at least one earthquake with magnitude $m \geq M$ in the next Δt years is given by:

$$P(n \geq 1; \Delta t) = 1 - e^{-\lambda(m \geq M)\Delta t} \tag{3.18}$$

We select a time period Δt of 3 years for these estimates, since we have little confidence that reasonable results can be obtained for longer time periods, given the observed variation in seismicity rates over the lifetime of the project.

The seismicity rates determined from Equation (3.17) are used in Equation (3.18) to estimate the probabilities of one or more earthquakes occurring within the next 3 years, and having a magnitude greater than 3.0, 3.5, 4.0, 4.5, 5.0, and 5.5. Short-term earthquake occurrence probabilities are computed independently for both the near-well area (Table 3-1) and the NW cluster (Table 3-2). The estimated short-term earthquake probability results indicate a 20 to 40 % probability of another $M \geq 4$ earthquake occurring within the next 3 years, and a 5 to 10 % probability of an $M \geq 5$ earthquake in the case that $M_{max} \geq 5.0$.

Table 3-1. Estimated probability of occurrence of earthquakes over the next 3 years for the near-well area.

	Probability of earthquake $m \geq M$ within the next 3 years				
M	$M_{\max} = 4.0$	$M_{\max} = 4.5$	$M_{\max} = 5.0$	$M_{\max} = 5.5$	$M_{\max} = 6.0$
3.0	0.91	0.92	0.92	0.93	0.93
3.5	0.53	0.63	0.66	0.68	0.68
4.0		0.26	0.34	0.38	0.39
4.5			0.12	0.17	0.19
5.0				0.05	0.08
5.5					0.02

Table 3-2. Estimated probability of occurrence of earthquakes over the next 3 years for the NW cluster area.

	Probability of earthquake $m \geq M$ within the next 3 years				
M	$M_{\max} = 4.0$	$M_{\max} = 4.5$	$M_{\max} = 5.0$	$M_{\max} = 5.5$	$M_{\max} = 6.0$
3.0	0.63	0.65	0.66	0.65	0.66
3.5	0.29	0.37	0.40	0.40	0.41
4.0		0.14	0.20	0.21	0.23
4.5			0.07	0.10	0.11
5.0				0.03	0.05
5.5					0.02

Formally, the assumptions of a Poisson process are not met for this data set since no attempt was made to decluster the earthquake catalog to remove aftershocks or otherwise account for dependent events. The estimated rates and probabilities therefore are higher than would be obtained otherwise. In addition, the Gutenberg-Richter model used to estimate the rates of larger-magnitude earthquakes overestimates the observed rates of seismicity. Finally, the probabilities were calculated for the NW cluster and the near-well area, assuming that seismicity in the two areas is independent, however since seismicity in both areas is ultimately the product of the same injection sequence, the assumption of independence may not be warranted. The calculated probabilities therefore are order-of-magnitude, and possibly conservative estimates of short-term earthquake recurrence.

3.5 Discussion

A thorough analysis of seismic risk posed by induced seismicity at PVU would consider the rates at which damaging ground motions are likely to occur in the populated surrounding areas, and the likelihood of damage, economic loss, and potential life-loss given those loadings. Such an analysis is beyond the scope of this report, and many of the required input parameters are not currently known. However, some of the necessary inputs required for such an analysis have been discussed in this section.

A probabilistic seismic hazard analysis (PSHA) estimates the average rate $\bar{\lambda}(a > A)$ of exceeding a specified ground motion A given an average earthquake rate $\bar{\nu}(EQ)$ and a conditional probability of exceeding ground motion A given the earthquake (Cornell, 1968):

$$\begin{aligned} \bar{\lambda}(a > A) &= \bar{\nu}(EQ) \Pr(a > A \mid EQ) \\ &= \iint_{M,R} \bar{\nu}_{m,r}(m,r) \Pr(a > A \mid m,r)\, dm dr \end{aligned} \tag{3.19}$$

In order to make the calculations which are implicit in Equation (3.19) we need to know the average seismicity rates, maximum magnitudes, and the magnitude distributions for the areas of induced seismicity. As shown earlier in this section, these parameters have changed substantially at PVU over the lifetime of the project, making estimates for future behavior highly uncertain. An even bigger problem is that the precise relation between the seismicity rate and injection parameters that can be controlled (e.g., average flow rate, maximum injection pressure, shut-in duration, etc.) is poorly known. Additional required parameters include the attenuation of ground motions with distance, site-response properties (e.g., V_{S30} and basin depth), and the density and fragility of residences and other structures.

Recent studies have attempted to estimate the probability of earthquake occurrence (Bachmann and others, 2011; Barth and others, 2013) and its relation to injection parameters in an attempt to devise methods for controlling seismic hazards from enhanced geothermal systems (EGS). Other studies of EGS injection have estimated seismic hazard for induced seismicity using a standard PSHA approach (Convertito and others, 2012; Mena and others, 2013). The long-term behavior of EGS injection likely differs substantially from injection-only operations such as PVU, since fluids are withdrawn in EGS systems, and since there is a much closer correlation between induced seismicity and recent injection.

Long-term seismic hazard estimates will be difficult to make at PVU without developing models that are capable of relating induced seismicity to injection operations. Such models have not yet been developed for PVU, although it is possible that recent numerical modeling approaches could be used to estimate both the pressure response and the seismicity response to injection (e.g., Wang, 2008; Baisch and others, 2010; Lee and Ghassemi, 2010; Lee and Ghassemi, 2011; Wang and Ghassemi, 2012). Short-term seismic hazard estimates can be made by extrapolating recent seismicity parameters, however even these estimates are likely to include substantial uncertainty.

4 Injection Pressures and Flow Rates

In order to predict the PVU reservoir response to future injection, it is necessary to understand the reservoir characteristics and their evolution over time. We have found that industry-standard well-test analysis methods based on idealized models of the reservoir provide a relatively simple way to determine these characteristics, and can reasonably accurately predict the observed pressure response at the PVU wellhead; however, both the determination of the parameters and their interpretation in terms of the actual behavior of the reservoir are subject to significant uncertainty. This section describes the history of PVU injection, examines previous modeling work, reviews the theoretical models used, shows the results of the modeling, and uses the models obtained to predict well-head pressures under various changes in injection operations.

4.1 Injection History

Between 1991 and 1995, PVU conducted a series of 7 injection tests, an acid stimulation test, and a reservoir integrity test. The purpose of these tests was to qualify for a permit for long-term injection from EPA. Continuous injection of brine began in July 1996, after EPA granted the permit. Since continuous injection began, PVU has instituted and maintained three major changes in injection operations. Each change was invoked to mitigate the potential for unacceptable seismicity or to improve injection economics. These injection phases are described below. Plots of the daily average injection flow rate, surface injection pressure, and downhole pressure at a depth of 14,100 ft (4.3 km) throughout the history of PVU injection operations are shown in Figure 4-1.

4.1.1 Phase I (July 22, 1996 – July 25, 1999)

During this initial phase of continuous injection, PVU injected at a nominal flow rate of 345 gpm (~1306 l/min), at about 4,950 psi (~34.1 MPa) average surface pressure. This corresponds to approximately 11,800 psi (~81.4 MPa) downhole pressure at 14,100 ft (4.3 km) depth. To maintain this flow rate, 3 constant-rate pumps were used with each operating at 115 gpm. The surface pressure on occasion approached the wellhead pressure safety limit of 5,000 psi. At these times PVU would shut down 1 or 2 injection pumps, reducing the injection rate and allowing the pressure to drop a few hundred psi, before returning to 3-pump injection. These shutdowns occurred frequently and lasted for minutes, hours, or a few days. Maintenance shutdowns lasted for 1 to 2 weeks and, in mid-1997, a 71-day shutdown was needed when replacing the operations contractor. The shutdowns resulted in an overall average injection rate for phase I of ~300 gpm

(1136 l/min). The injectate during phase I was 70% Paradox Valley Brine (PVB) and 30% fresh water.

Due to concerns about corrosion, the decision was made in 1997 to switch from using an O_2 scavenger to a rust inhibitor, as the O_2 scavenger was found to be insufficient as a corrosion inhibitor. While the rust inhibitor was substantially more effective at inhibiting corrosion, it also increased the risk of precipitation of elemental sulfur.

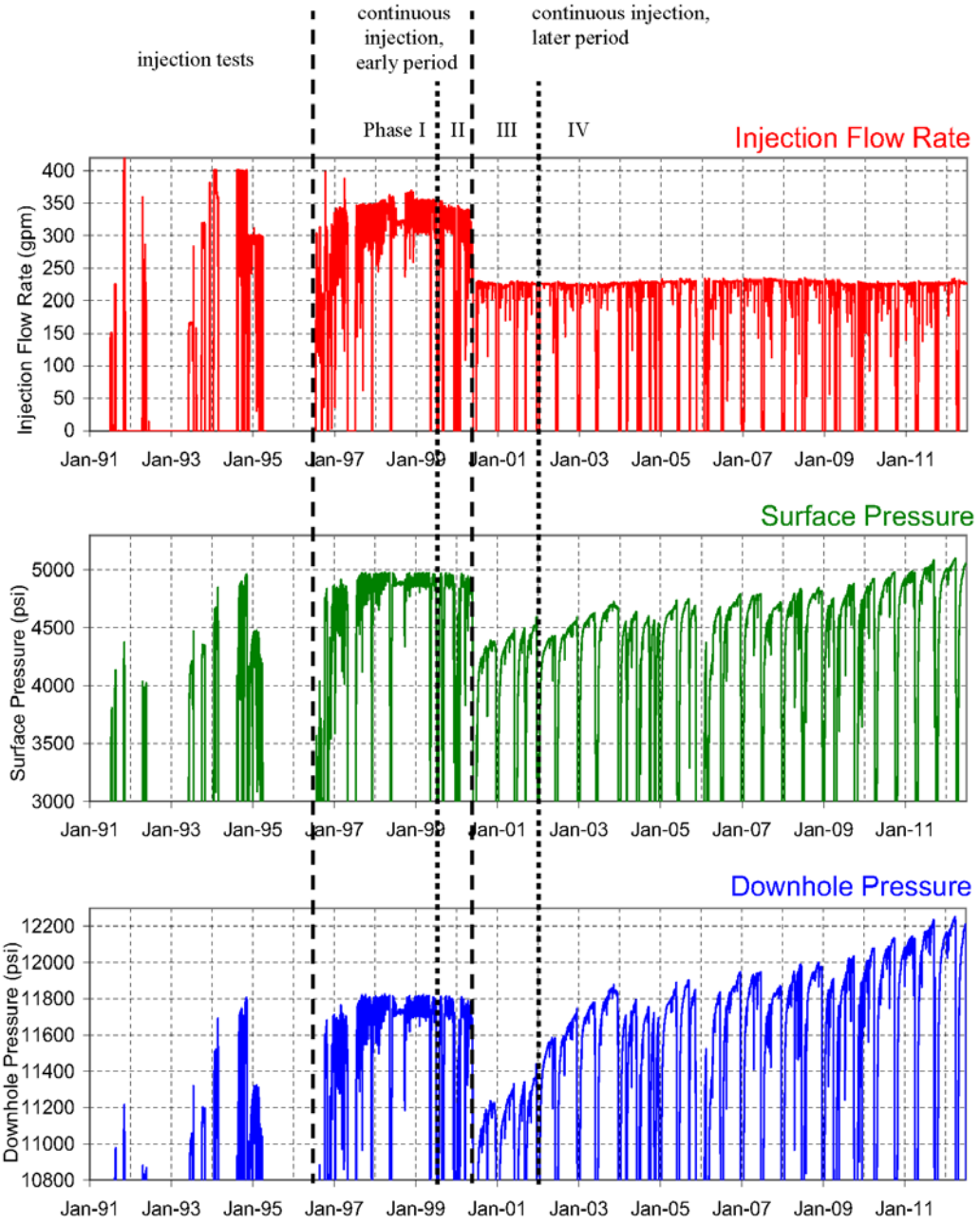

Figure 4-1. Daily average injection flow rate (top), daily average surface injection pressure (middle), and daily average downhole pressure at 14,100 ft (4.3 km) depth (bottom) during PVU injection operations.

4.1.2 Phase II (July 26, 1999 – June 22, 2000)

Following two M_L 3.5 induced earthquakes in June and July, 1999, PVU augmented injection to include a 20-day shutdown (i.e., a "shut-in") every 6 months. Prior to these events, it was noted that the rate of seismicity in the near-wellbore region (i.e., within about a 2-km radius from the wellbore) decreased during and following unscheduled maintenance shutdowns and during the shutdowns following the injection tests of 1991 through 1995. It was thought that the biannual shutdowns might reduce the potential for inducing felt seismicity by allowing extra time for the injectate to diffuse from the pressurized fractures and faults into the formation rock matrix. When injecting during this phase, the injection pressure and flow rate were the same as during Phase I.

4.1.3 Phase III (June 23, 2000 – January 6, 2002)

Immediately following a M_L 4.3 earthquake on May 27, 2000, PVU shut down for 28 days. During this shutdown period, PVU evaluated the existing injection strategy and its relationship to induced seismicity. PVU decided to reduce the injection flow rate in order to reduce the potential for inducing felt seismicity. On June 23, 2000, PVU resumed injection using two pumps rather than alternating between 2 and 3 pumps. The biannual 20-day shutdowns were maintained. The nominal flow rate during Phase III, while injecting using two pumps, was 230 gpm (~871 l/min). Accounting for the two 20-day shut-ins per year, the average injection flow rate was approximately 205 gpm (776 l/min), a decrease of about 32% compared to Phase I. The 70:30 ratio of brine to fresh water was maintained.

4.1.4 Phase IV (January 7, 2002 – present)

Beginning with continuous injection operations in 1996, the injectate had been diluted to 70% PVB and 30% Dolores River fresh water. A geochemical study had predicted that if 100% PVB were injected, it would interact with connate fluids and the dolomitized Leadville limestone at downhole (initial) temperatures and pressures, and that PVB would then precipitate calcium sulfate, which in turn would lead to restricted permeability (Kharaka and others, 1997). During October 2001, with the decreased injection volume discussed above, the injectate concentration concerns were reconsidered. Temperature logging in the injection interval documented substantial near-wellbore cooling, indicating that a significant displacement of connate brine away from the wellbore had occurred by this time, reducing the potential for 100% PVB and connate brine to mix, and therefore that if precipitation occurred, it would not be near the wellbore perforations where clogging would be a concern. Further discussions indicated that, if precipitation occurred, its maximum expected rate would be ~8 tons of calcium sulfate per day. To put this amount into perspective, injecting at ~230 gpm, assuming a density of 9.86 lbs/gal (17% more dense than fresh water), results in a daily injection of ~1633 tons. The maximum expected precipitate is ~0.5% of the daily injection mass.

After considering this new information, Reclamation decided to begin injecting 100% PVB, in order to increase the amount of salt disposed with the reduced injection rate initialized in Phase III. Injecting 100% PVB began on January 7, 2002, following the December-January 20-day shutdown, and has been maintained since. The same reduced injection rate as in Phase III (230 gpm) and biannual 20-day shutdowns have been maintained. The only noticeable effect of the change to 100% PVB injectate has been increasing bottom hole pressure because of the increased density of 100% PVB (by about 5%) over the 70% PVB to 30% fresh water mix.

4.2 Previous Work

One of the key parameters that defines reservoir behavior is the effective permeability. Previous estimates of permeability have varied widely. Drill stem tests using a variable flow rate gave an original permeability of 7.97 mD (Harr, 1989). However, Horner analysis performed at the same time indicated a permeability between 1.3 and 1.5 mD (Harr, 1989). Additionally, analysis of core samples from the Conoco-Scorup well located approximately 4.6 km to the northeast yielded permeabilities ranging from 0.03 to 1.3 mD (Harr, 1989), which could suggest significant regional variations in permeability.

A series of 7 injection tests were performed between 1991 and 1995. Permeabilities were only calculated for the first 3 tests, which took place between July 11, 1991 and June 18, 1992, primarily due to equipment failures in later tests. The permeabilities for the first injection and falloff periods were calculated as 4-5 mD and 2 mD, respectively. The second injection and falloff periods yielded 7.8 mD and 2.2 mD, respectively. The third falloff period yielded a permeability of 1.6 mD, while the third injection period was determined to be unanalyzable due to numerous flow rate changes caused by equipment failure. The lower permeabilities calculated during falloff periods, as compared with injection periods, were assumed to indicate fracture closure (Envirocorp Services and Technology Inc., 1995).

An early model of the injection test data attempted to fit the data from the seventh and final injection test, which took place from August 14, 1994 to April 3, 1995, using a fracture network model with 5% porosity and a permeability of 3 mD (Envirocorp Services and Technology Inc., 1995). While they obtained reasonable fits to the data from this injection test, their model predicted future pressures that were significantly lower than observed pressures. While the modeled injection scenarios differ from the actual injection scenarios, preventing a direct comparison, their model predicted that surface pressure would not exceed 4500 psi after 10 years of continuous injection at a flow rate of 300 gpm, whereas the observed pressures exceeded 4500 psi after less than 4 months of injection at an average flow rate of 163 gpm. This suggests that the effective permeability-thickness and/or porosity-thickness may have been overestimated in this early modeling.

In 2001, Reclamation funded USGS to perform fluid-flow modeling of the 1996-2000 pressure and flow data, and a draft report was received in 2009 (Roeloffs and Denlinger, 2009). The USGS model consisted of a radially-symmetric finite element grid with 20 layers based on stratigraphy, each characterized by four parameters (shear modulus, Poisson ratio, Skempton's coefficient, and hydraulic diffusivity). The model was calibrated by trial-and-error matching of the predicted flows and pressures with those measured at the wellhead. For the layer representing the Leadville formation, a porosity of 10% and a permeability of 28 mD were assumed for a thickness of 146 meters (479 feet), with significantly lower values for other layers. In contrast, Bremkamp and Harr (1988) determined a porosity in the Leadville of ≥10% for only 2 feet of its 416-foot thickness, using sonic logging, or 18 feet, using visual binocular examination of recovered core. Hydraulic diffusivity (calculated from permeability, formation thicknesses, porosity, and shear modulus), was found to be the parameter most strongly effecting pressure distribution in the model. The USGS model apparently did not incorporate skin factor or wellbore storage parameters.

The USGS model provides a reasonably good fit to the flow rate data for approximately the first 500 days, but then the modeled flow rates begin to decrease, while the measured flow rates remain approximately constant. Roeloffs and Denlinger (2009) suggest that formation permeability may have increased, or that the flow may have reached a zone of higher permeability away from the well.

The permeability of intact limestone and dolomite generally varies from 0.01 to 0.1 mD (Bear, 1972). The permeability value for intact rock is known as primary, or matrix, permeability, and is generally only applicable to laboratory samples, as rocks over larger scales will contain at least some degree of fracturing. Limestones may also have increased permeability due to vugular porosity. The permeability due to fracturing and secondary porosity is known as secondary permeability and can vary by several orders of magnitude, even exceeding 10^5 mD in some highly fractured locations (Cox and others, 2000). Thus, the estimated permeabilities of a few mD, while higher than would be expected to be measured under laboratory conditions, are reasonable for a moderately fractured reservoir.

4.3 Fitting of Pressure/Flow Data to Idealized Models

It was unclear initially if complicated numerical models were required to fit the pressure-flow data at the wellhead, or instead if simple idealized models could suffice. In the absence of monitoring wells or other independent means of verifying predicted pressures within the injection reservoir at distances away from the wellbore, we were concerned that use of excessively complex models might result in overfitting of the wellhead data, and yield a correspondingly poor predictive capability of the models in evaluating potential injection scenarios. We therefore tried fitting the wellhead data for individual injection and shut-in cycles using several simple, idealized models commonly employed in the well-testing

and reservoir-modeling industry. F.A.S.T. WellTest software v.7.6.0, described in Fekete (2012), was used for this analysis.

Biot (1941) developed a model of a fluid-filled porous material based on a conceptual model of a coherent solid skeleton and freely moving pore fluid (Detournay and Cheng, 1993). Under this model, for the case of an isotropic applied stress tensor σ, the constitutive equations are

$$\begin{aligned} \varepsilon &= a_{11}\sigma + a_{12}p \\ \varsigma &= a_{21}\sigma + a_{22}p \end{aligned} \tag{4.1}$$

where ς is the increment of fluid content, p is the fluid pressure, and ε is the volumetric strain (Wang, 2000). This model includes full coupling between the solid and fluid components. Substituting physically meaningful constants, the most general form of the linear constitutive equations for isotropic material response is

$$\begin{aligned} \varepsilon_{ij} &= \frac{\sigma_{ij}}{2G} - \left(\frac{1}{6G} - \frac{1}{9K}\right)\delta_{ij}\sigma_{kk} + \frac{1}{3H}\delta_{ij}p \\ \varsigma &= \frac{\sigma_{kk}}{3H} + \frac{p}{R} \end{aligned} \tag{4.2}$$

where K and G are the bulk modulus and shear modulus of the drained elastic solid, and H, and R are constitutive constants characterizing the coupling between the solid fluid stress and strain (Detournay and Cheng, 1993).

At reservoir depths, the rock compressibility is generally small, and thus a simplifying assumption may be made in order to uncouple the solid and fluid components. This is a common simplification in reservoir modeling applications, and is used in our analysis.

For the uncoupled system, and assuming incompressible rock, the governing equation for radial flow in cylindrical coordinates is

$$\frac{\partial^2 p}{\partial r^2} + \frac{1}{r}\frac{\partial p}{\partial r} = \frac{\phi c_t \mu}{k}\frac{\partial p}{\partial t} \tag{4.3}$$

where r is the radial distance from the well in centimeters, t is time in seconds, p is the reservoir pressure in atmospheres at distance r and time t, ϕ is the formation porosity as a fraction of bulk volume, k is the formation permeability in Darcies, μ is the fluid viscosity in centipoises, and c_t is the total compressibility in volumes per volume per atmosphere (Horner, 1951).

For a point source, the change in pressure resulting from an applied flow is

$$p - p_0 = \frac{q\mu}{4\pi kh}\mathrm{Ei}\left(\frac{r^2\phi\mu c_t}{4kt}\right) \tag{4.4}$$

where p_0 is the initial reservoir pressure in atmospheres at $t = 0$, q is a constant rate of production of the well (starting at $t = 0$) in cubic centimeters of subsurface volume per second, h is the layer thickness in centimeters, $\mathrm{Ei}(x); x > 0$ is the exponential integral (Abramowitz and Stegun, 1964), and other variables are the same as in Equation (4.3). This solution assumes an infinite reservoir and an infinitely small wellbore radius (Horner, 1951).

For sufficiently small $x > 0$, $\mathrm{Ei}(x)$ may be accurately approximated by $\mathrm{Ei}(x) \approx \gamma + \log(x)$, where γ is Euler's constant (Abramowitz and Stegun, 1964). Thus if the parameters of the model are homogeneous and constant over time, then Equation (4.4) may be approximated as

$$p - p_0 = -\frac{q\mu}{4\pi kh}\log\left(\frac{4kt}{r^2\phi\mu c_t}\right) + const. \tag{4.5}$$

which shows that for continuous injection $q < 0$, the pressure change at the wellbore radius r_w is asymptotic to $\log(t)$, and with a slope proportional to the flow rate q and inversely proportional to the permeability-thickness product kh.

Typical well-testing procedures consider a period of constant production starting at time $t = 0$, followed by a shut-in period starting at time $t_0 > 0$, then the well pressure during the shut-in period at time $t_0 + \tau$, can be obtained by superimposing two equations of the form of Equation (4.4). Using the wellbore radius r_w for *r*, this leads to the equation

$$p_w - p_0 = \frac{q\mu}{4\pi kh}\left[\mathrm{Ei}\left(\frac{r_w{}^2\phi\mu c_t}{4k(t_0+\tau)}\right) - \mathrm{Ei}\left(\frac{r_w{}^2\phi\mu c_t}{4k\tau}\right)\right] \tag{4.6}$$

where p_w is the pressure at the wellbore in atmospheres and r_w is in centimeters. Using the previous approximation for $\mathrm{Ei}(x)$ at small $x > 0$, the pressure change during the shut-in period described by Equation (4.6) may be approximated as

$$p_w - p_0 = -\frac{q\mu}{4\pi kh}\log\left(\frac{t_0+\tau}{\tau}\right) \tag{4.7}$$

For continuous injection $q < 0$, Equation (4.7) shows that the pressure fall-off at the wellbore radius following shut-in is asymptotic to $\log\left(\frac{t_0 + \tau}{\tau}\right)$, where t_0 is the injection duration, τ is the time since shut-in, and where the slope is proportional to the flow rate q and inversely proportional to the permeability-thickness product kh. Horner (1951) demonstrates that the error introduced by this approximation typically drops to 0.25% within seconds of closing the well.

In dimensionless variables, the governing equation equivalent to Equation (4.3) is

$$\frac{\partial^2 p_D}{\partial r_D^{\,2}} + \frac{1}{r_D}\frac{\partial p_D}{\partial r_D} = \frac{\partial p_D}{\partial t_D} \tag{4.8}$$

where, in arbitrary units, $r_D = r/r_w$ is the dimensionless radial distance from the well, $t_D = \frac{kt}{r_w^{\,2}\phi\mu c_t}$ is dimensionless time, and $p_D = \frac{kh}{q\mu}(p - p_0)$ is the dimensionless pressure change on the formation side at distance r_D and time t_D (Agarwal and others, 1970). Using the previously defined units, the equations for r_D and t_D are unchanged, while the equation for p_D becomes $p_D = 0.0689\frac{kh}{q\mu}(p - p_0)$. All model properties are assumed to remain constant with time, and pressure is calculated based on the observed injection rate, which varies over time.

In solving Equation (4.8) for a finite wellbore, two additional variables, the wellbore storage constant and skin factor, are introduced in the inner boundary conditions, in order to ensure continuity across the wellbore boundary. In dimensionless variables, the boundary conditions are

$$C_D\frac{dp_{wD}}{dt_D} - \left(\frac{\partial p_D}{\partial r_D}\right)_{r_D=1} = 1 \tag{4.9}$$

and

$$p_{wD} = \left[p_D - s\left(\frac{\partial p_D}{\partial r_D}\right)\right]_{r_D=1} \tag{4.10}$$

where p_{wD} is the dimensionless pressure drop within the wellbore, C_D is the dimensionless wellbore storage constant, s is the dimensionless skin factor, and other parameters are the same as in Equation (4.8) (Agarwal and others, 1970). All fluid and rock properties are assumed to remain constant.

This analysis used injection flow rates and surface pressures recorded at the wellhead since continuous injection began in 1996. The sample rate of that data is non-uniform over time. Injection data prior to 2003 were recorded on an older SCADA system in a format that is currently inaccessible. For this period, only daily average pressures and flow rates are available. Starting in 2003, a newer SCADA system was installed, and that data is available at much higher sample rates (up to 1 sample every 2 seconds). We found that mixing data at the two sample rates created artificial trends in the data. For example, a large apparent decrease in the wellbore storage constant occurred when mixing the daily-average with the high-frequency data. While misfits were lower using data with the higher sample rate, and the absolute values obtained for parameters were likely more accurate, we are more interested in trends in the parameters rather than in their particular values. We therefore decided to use the daily average data over the entire well operating history for this analysis.

Reservoir temperature is a significant factor affecting the modeling, primarily because of its effect on the fluid viscosity, as the temperature of the injectate is generally assumed to be equal to the undisturbed reservoir temperature. While this assumption is probably adequate for short-term injection testing, the volume of fluid that has been injected into the PVU injection well has likely led to cooling a significant distance from the well, and thus the reservoir temperature varies in both time and space. However, as our model cannot account for temperature variations, and as we have no data to constrain temperatures away from the well, a single temperature was used for the modeling. A temperature of 37.8˚C was used, corresponding to the temperature measured 3 days into a shut-in that occurred in March 1994 (Subsurface Technology, 2001).

Other input parameters include a reservoir thickness of 100 feet (30.5 meters), porosity of 3%, and salinity of 2.6 kg/L after January 8, 2002, when injection of 100% brine began, and 1.82 kg/L prior to this date, when the injectate was a mixture of 70% brine and 30% fresh water. The salinity of the fresh water was assumed to be negligible relative to the brine, and therefore a salinity 70% that of the brine was used for the mixture. The assumed thickness of 100 feet is approximately equal to the thickness of the perforated interval of the upper Leadville, as logging has indicated that the middle and lower Leadville perforations are covered with fill (Subsurface Technology, 2001), and it is unknown to what extent fluid is able to migrate vertically outside of the perforated interval. Note that this is significantly smaller than the value of 479 feet used by Roeloffs and Denlinger (Roeloffs and Denlinger, 2009), which is approximately equal to the entire thickness of the Leadville formation.

Viscosity and fluid compressibility are calculated using the mean temperature and salinity. The calculated viscosity is 1.030 cP during injection of 70% brine and 1.348 cP during injection of 100% brine. The calculated fluid compressibility is 1.933×10^{-6} psi^{-1} during the injection of 70% brine and 1.731×10^{-6} psi^{-1} during the injection of 100% brine.

While the input parameters have a significant effect on the absolute values of the permeability, the effect on the relative values is minimal, and thus we do not expect our interpretations or the results of the forward modeling performed in Section 4.5 to be significantly affected by the choice of input parameters. For example, if we had used the value of 479 feet chosen by Roeloffs and Denlinger (Roeloffs and Denlinger, 2009) rather than 100 feet for the layer thickness, the calculated permeabilities would be reduced by a factor of 4.79, but the ratios of permeabilities between cycles would not be affected, nor would the pressures obtained in forward modeling. Variations in input parameters in space or time, such as a change in the thickness of the Leadville away from the well or reservoir cooling over time, could potentially have more significant effects, but our model cannot account for changes in these parameters, nor do we have data to constrain potential changes.

Downhole pressures were calculated by adding a constant value to the surface pressures, accounting for the weight of the brine and the frictional effect due to flow, assuming new pipe conditions with no scale buildup inside the tubing (Mahrer and others, 2004). The friction term is negligible for the injection rates and tubing size used at PVU. It is possible that the friction term becomes more significant over time due to scale build-up, but as we have no way of determining this, we are unable to incorporate the potential changes in friction into our analysis. A constant pressure difference between the wellhead and downhole pressure of 6822 psi was used for continuous injection Phases I-III, and 7133 psi for injection Phase IV, when injectate density increased as a result of the switch to 100% brine.

After comparisons of several different models, a vertically stratified, radially symmetric model with no-flow boundaries in the vertical direction and infinite-acting boundaries in the horizontal directions was selected. Models with finite no-flow or constant pressure boundaries in the x- and/or y-directions were considered, as well as radial composite models and models incorporating fractures and anisotropic permeability, but these models provided either a worse fit or an insignificant improvement in the fit to the data, and so the simplest model that adequately fit the data was selected. This model does not incorporate individual fractures, and so we assume that the near wellbore region is sufficiently fractured so that it can be adequately represented as a porous medium for the purpose of this simplified pressure-flow modeling.

There are 3 free parameters in our model: the effective permeability, k, skin due to damage, s_d, and dimensionless wellbore storage constant, C_D. While the entire flow rate history is incorporated into the calculation of modeled pressures, the parameters are fit individually for each build-up period. This approach is used to assess whether these parameters have changed over time, and because there was no clear reason for assuming that a single set of parameters would be adequate to fit all the data.

For Phases II-IV, when two 20-day shut-ins were scheduled every year, a cycle is defined to be the build-up period between two scheduled shut-ins. Unscheduled 11-day and 17-day shut-ins occurred in the cycles beginning July 26, 1999 and January 21, 2006, respectively, so these flow periods were each split into two cycles for the purpose of analysis. All cycles contain unscheduled shut-ins, which range in length from a few hours to 10 days, primarily due to equipment issues. In order to analyze the 6-month cycles as a single flow period despite the short shut-ins, it is necessary to input a small but non-zero flow rate for the short shut-in periods.

For Phase I, cycles are defined as the flow periods between two unscheduled multi-day shut-ins, which range in length from 4 to 70 days. Cycles range from 47 to 345 flow days in length; build-up periods of only a few days are excluded from analysis.

Defining cycles in this matter leads to a total of 38 cycles: 7 in Phase I, 3 in Phase II, 4 in Phase III, and 24 in Phase IV.

4.4 Results of Pressure/Flow Model Fitting

Model parameters were fit simultaneously for each injection cycle, using a Simplex automatic parameter estimation procedure to find a local minimum in the misfit between the data and the model. All parameters for each injection cycle were fit independently from the other injection cycles. Section 4.4.1 describes how the computed model parameters have evolved over the various phases of injection. Section 4.4.2 describes the quality of the model fits to the pressure-flow data.

4.4.1 Changes in Model Parameters over Time

In Phase I, values for k range from 9.06 to 10,200 mD, and values for s_d range from -5.82 to 2000, with a strong positive correlation between these two parameters. Values for C_D range from 6.27×10^5 to 1.46×10^6. The magnitude of variations in k and s_d is believed to be an artifact of attempts by the model to fit data that includes factors that the model cannot account for. In particular, the model seems to be unable to fit periods of frequent flow rate changes.

In Phase II, the variation in model parameters is much smaller than found in Phase I, with k ranging from 13.64 to 21.93, s_d ranging from 6.05 to -3.99, and C_D ranging from 8.80×10^5 to 1.37×10^6.

In Phases III and IV, for 27 of the 28 cycles in these phases, effective permeabilities range from 10.39 to 29.21 mD, with a mean of 18.03 mD and median of 16.74 mD, and skin values range from -5.98 to -1.98, with a mean of -

4.35 and median of -4.47. In these phases, neither of these parameters shows any clear trends with time, as shown in Figure 4-2.

The remaining cycle was initially a significant outlier, with a permeability of 140 and skin value of 26.31. There are no obvious differences in the build-up curves between this cycle and the other cycles, so as in early phases, it is likely that these differences are not real, but are due to the method of model fitting. For this reason, the permeability and wellbore storage constants was re-fit after fixing the value of s_d at the mean of the preceding and following cycles. This led to a permeability of 20.72, with a minimal increase in the misfit.

Dimensionless wellbore storage constants for Phases II-IV vary from 9.01×10^5 to 1.74×10^6, which correspond to dimensional wellbore storage constants of 4.17 to 8.03 ft^3/psi. This is significantly larger than the number expected from considering only the actual wellbore volume, suggesting that the fractured area around the well may essentially be acting as an enlarged wellbore or an extension of the wellbore (Fekete, 2012). The wellbore storage constants are somewhat higher prior to 2003, with a decrease of about 21% between the mean values from September 1999 to January 2002 (the beginning of Phase IV, when the change from injection of 70% brine to injection of 100% brine occurred) and the mean values beginning with June 2002 (Figure 4-2b). The magnitude of the decrease between the mean of the cycles in these two time periods is approximately 2.94×10^5, which is 2.6 times the standard deviation of the wellbore storage constants beginning in June 2002, indicating that the decrease is statistically significant. It is possible that the decrease in the wellbore storage constant indicates a decrease in the perforated interval of the wellbore due to narrowing of the wellbore and/or precipitation of elemental sulfur, both of which have been observed in past wireline logs (Subsurface Technology, 2001).

There is significant tradeoff between the parameters, leading to concern that the resulting parameters may not be robust, as evidenced by the two cycles with outlying values of both k and s_d. The values of k and s_d have a strong positive correlation (Figure 4-3). In order to minimize the tradeoff, the values for k and C_D are refit after fixing s_d at a value of -4.35. This value for s_d corresponds to the mean of the calculated values for the cycles in Phase III and Phase IV.

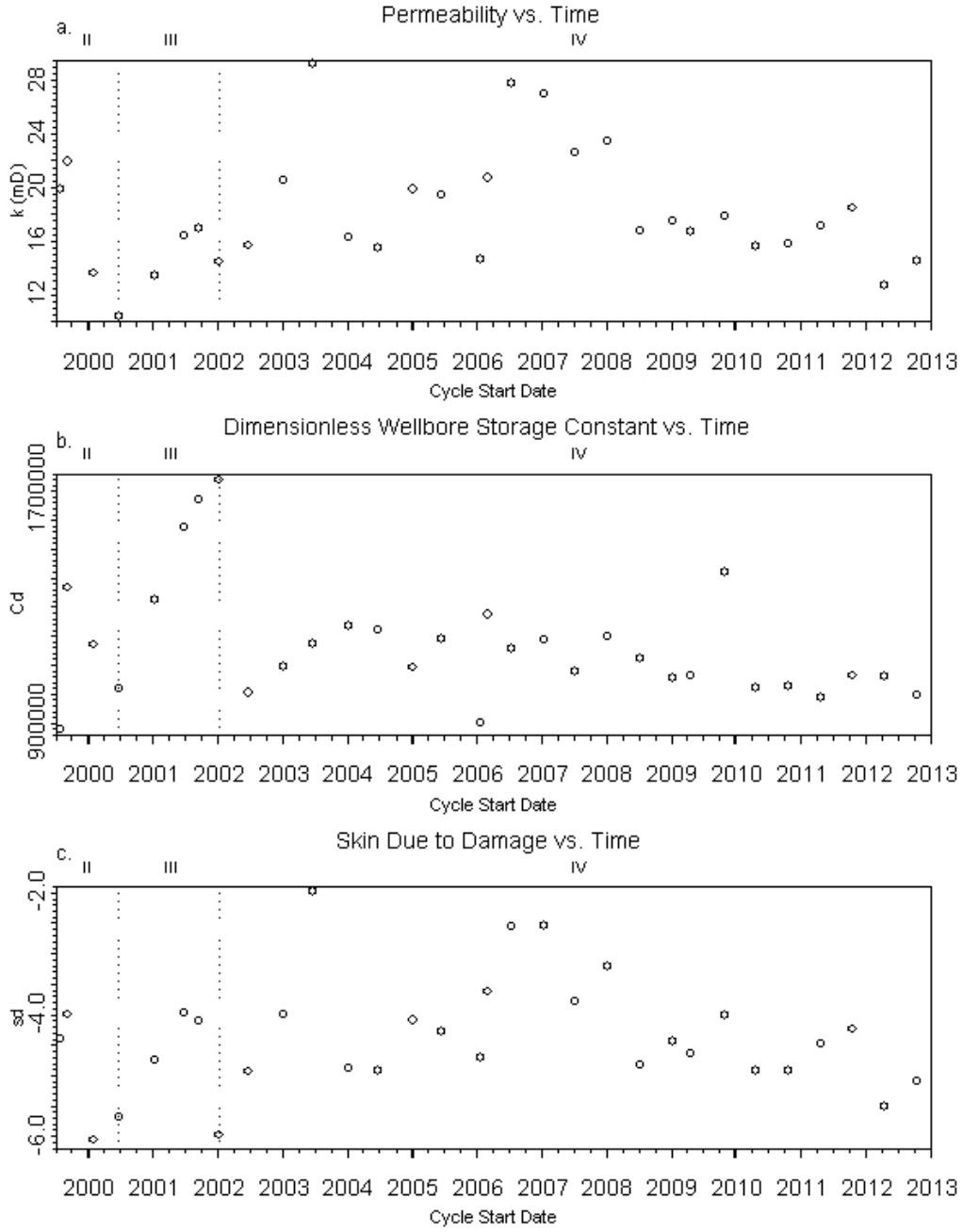

Figure 4-2. Effective permeability (a), dimensionless wellbore storage constant (b), and skin due to damage (c) versus time for pressure build-up cycles in Phases II-IV. Dashed lines indicate boundaries of the injection phases.

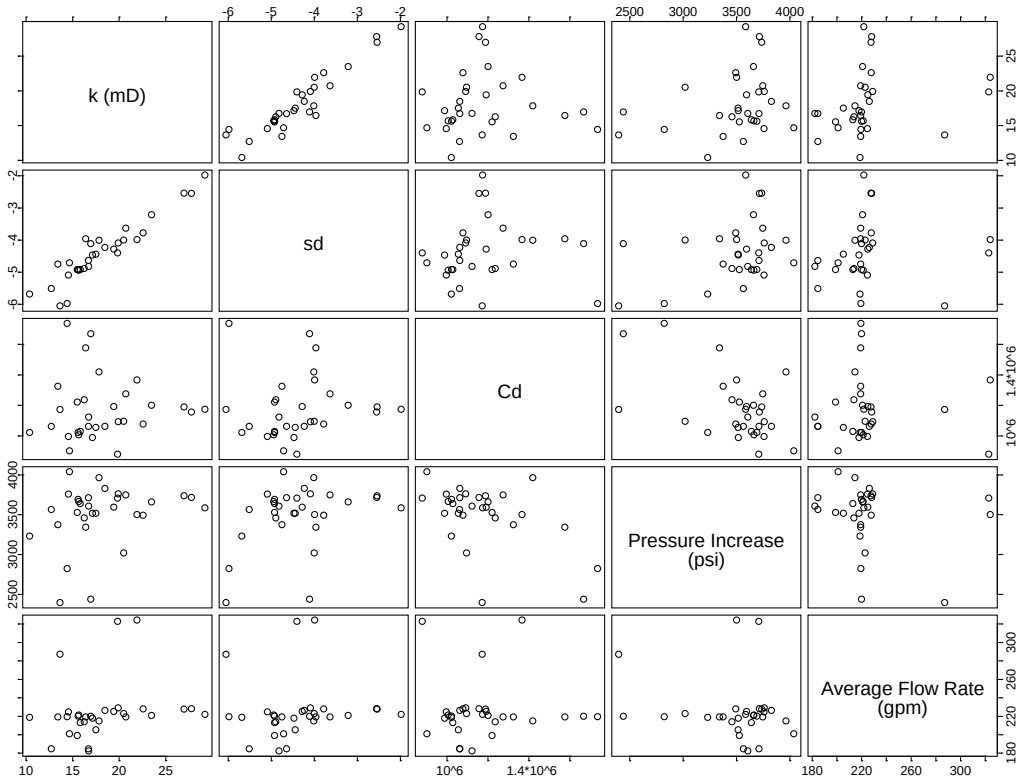

Figure 4-3. Scatter-plot matrix showing pairwise correlations between permeability (*k*), skin due to damage (s_d), dimensionless wellbore storage constant (C_D), pressure increase, and average flow rate for all pressure build-up cycles in Phases II-IV. Note the strong correlation between permeability and skin.

Fixing s_d leads to much less variation in the values obtained for *k*, particularly those in Phase I and Phase II. The values for all cycles vary from 14.02 to 27.12, with a mean of 18.76 and median of 18.36. With the exception of an outlying cycle in 2002, the values are highest during Phases I and II, when the injection rate was higher, then lowest during Phase III, and have remained relatively constant since Phase IV began in 2002 (Figure 4-4).

The decrease in *k* between Phase II and Phase III may be an effect of fracture closure due to the decrease in flow rate and resultant decrease in reservoir pressure. Over time, the pressures have gradually increased to the pressures seen in Phase II, even surpassing these pressures in recent years. This increase in pressure could cause fractures to re-open and permeabilities to return to the values seen in Phase II. However, the permeabilities have remained lower than they were in Phase I, which could be an effect of precipitation in the near wellbore area, which could limit fluid flow and decrease the average effective permeability.

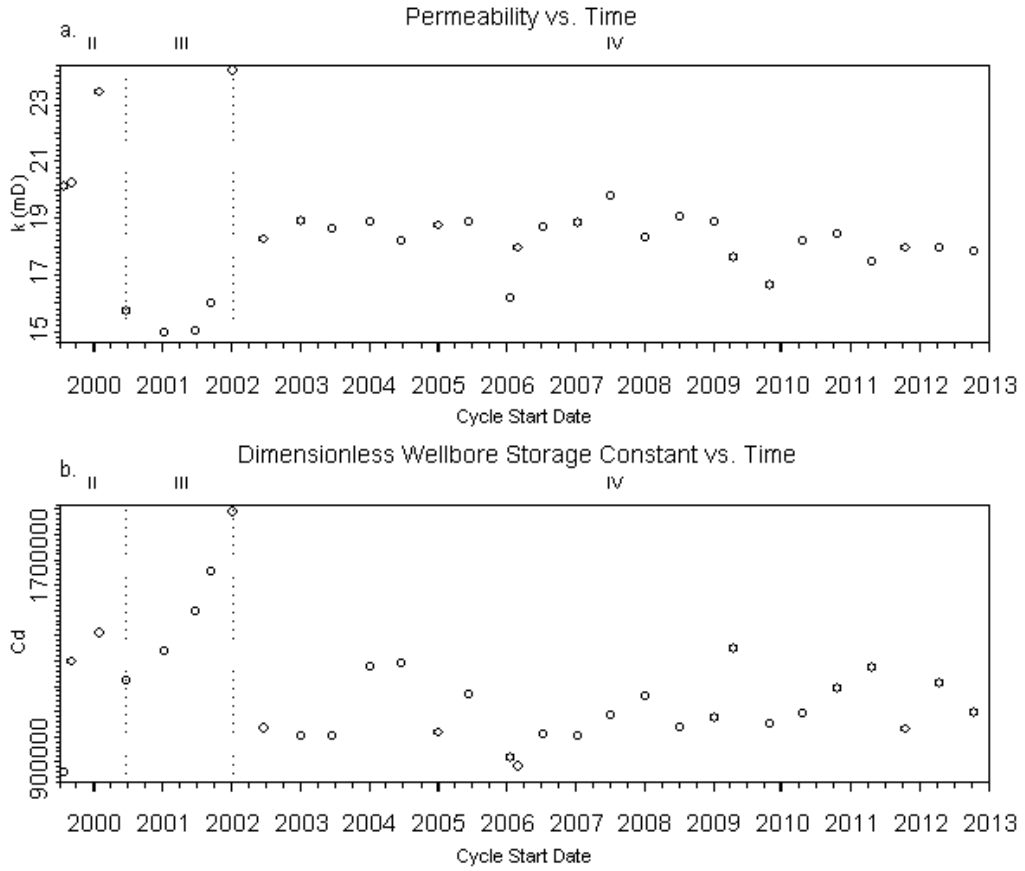

Figure 4-4. Effective permeability (a) and dimensionless wellbore storage constant (b) versus time for all pressure build-up cycles during Phases II-IV, fixing the value of s_d to -4.35. Dashed lines indicate boundaries of the injection phases.

The dimensionless wellbore storage constant varies from 4.70×10^5 to 1.89×10^6, corresponding to a dimensional wellbore storage constant varying from 2.18 to 8.73 ft^3/psi. For Phases II- IV, the wellbore storage constant shows a similar trend to the values fit without fixing s_d, with the highest values occurring prior to 2002, a 25% decrease from the mean values prior to June 2002 and the mean values beginning in June 2002, and relatively constant values since 2003. The decrease in the mean wellbore storage constant between January, 2002 and June, 2002 is 3.1 times the standard deviation of the data beginning in June, 2002, again indicating that the decrease appears to be statistically significant.

With the skin value fixed, the permeability, wellbore storage constant, pressure increase during the cycle, and average flow rate all appear to be independent of one another (Figure 4-5).

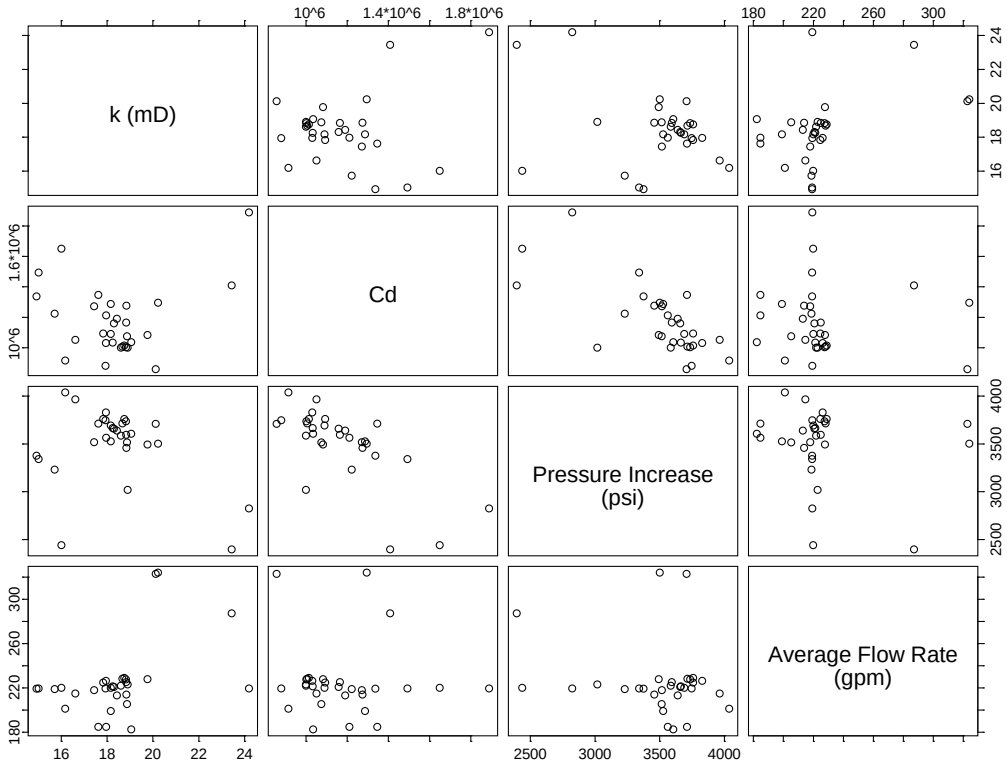

Figure 4-5. Scatter-plot matrix showing pairwise correlations between permeability (*k*), dimensionless wellbore storage constant (C_D), pressure increase, and average flow rate for all pressure build-up cycles in Phases II-IV, holding s_d fixed at -4.35.

The degree of tradeoff between the permeability and skin value demonstrates that we are unable to uniquely resolve the values for both parameters with the current dataset. It is possible, though not certain, that injecting at a fixed flow rate for a longer time period could allow the observation of boundary effects, which could help to resolve these parameters.

4.4.2 Model Pressure-History Plots and Type Curves

For each injection cycle, the free parameters of the model were fit simultaneously, using automatic parameter estimation to find a local minimum in the misfit between the "observed" and modeled pressure at the bottom of the well. Bottom-hole pressures ("observed") were calculated from the measured surface pressures by accounting for the weight of the brine in the wellbore, and for frictional effects of the flow. Interruptions in injection during an injection cycle were handled using superposition to account for the variable rate history. The results of this modeling are a series of pressure-history plots and type curves, one for each injection cycle, which illustrate the modeled flow regime and how well it fits the data.

Pressure-history modeling results from a typical injection cycle in Phase I are shown in Figure 4-6. This figure includes results for the case when all 3 model parameters are allowed to vary (upper plot), and for the case when s_d is held fixed (lower plot). These plots suggest that an idealized radial-flow model can provide a reasonable fit to this data, with errors of less than about 5 %. The model using 3 free parameters fits the data significantly better than the model using two free parameters. The corresponding type curves (pressure change and derivative) are shown in Figure 4-7 and suggest that a radial-flow model fits the data reasonable well.

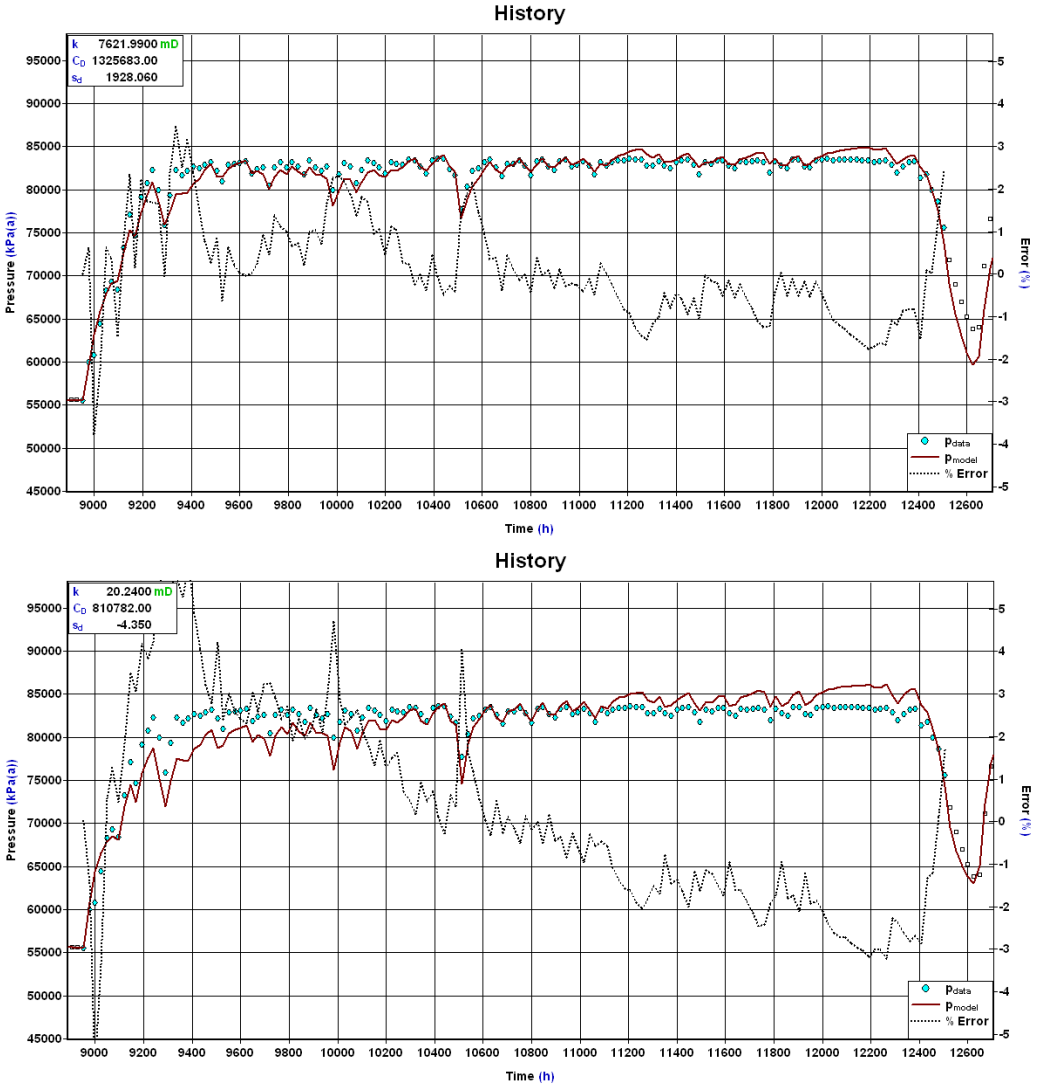

Figure 4-6. Recorded (blue dots) and modeled (red line) downhole pressures and percent error (dashed line) for an example Phase I cycle, beginning July 10, 1997, allowing all 3 parameters to vary (top) and fixing s_d at -4.35 (bottom). Recorded downhole pressures are calculated by adding a constant value of 6822 psi to measured surface pressures.

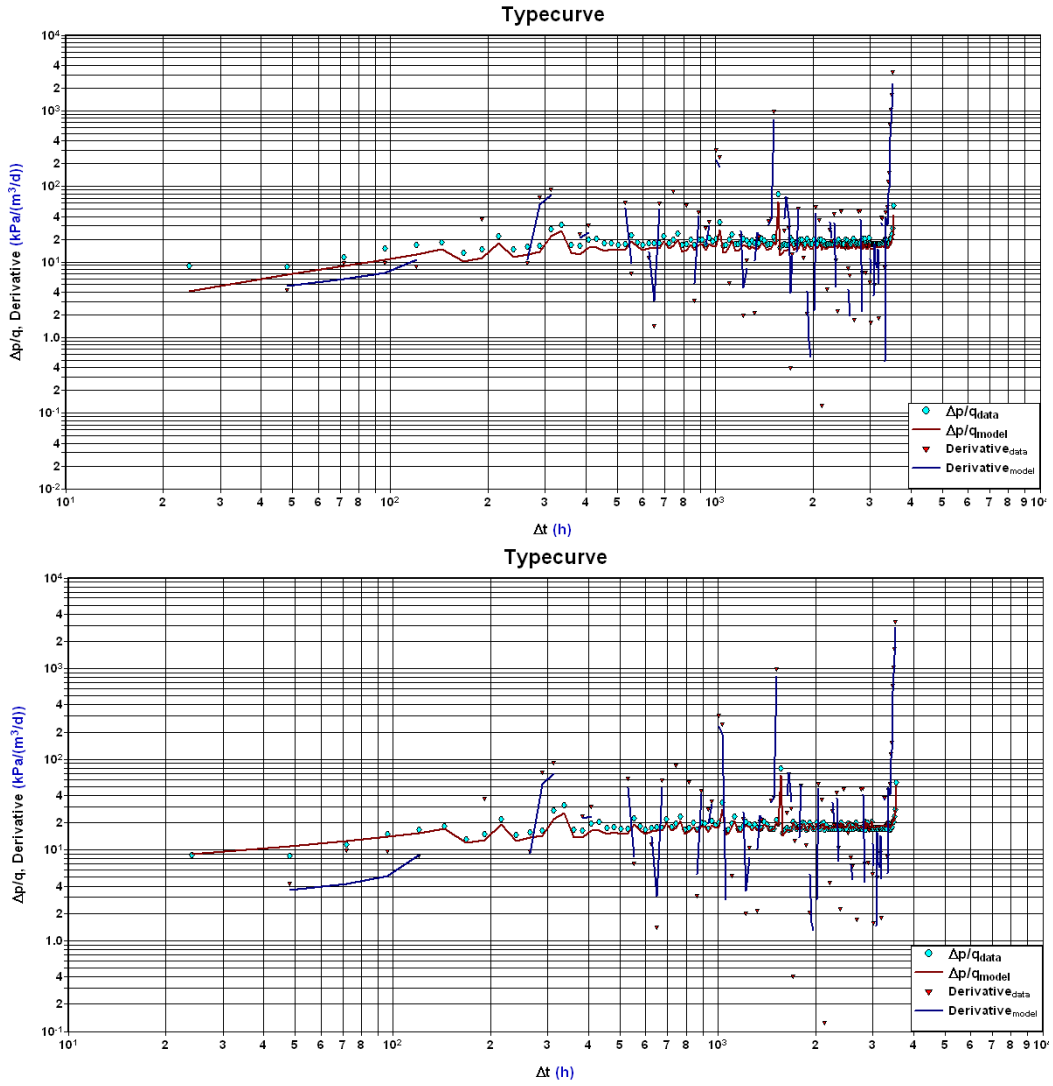

Figure 4-7. Recorded (blue dots) and modeled (red line) values for change in pressure (*Δp*) divided by flow rate (*q*), and the recorded (red triangles) and modeled (blue lines) values for the time derivative of *Δp/q* for an example Phase I cycle, beginning July 10, 1997, allowing all 3 parameters to vary (top) and fixing s_d at -4.35 (bottom).

Modeling results for typical injection cycles in the remaining phases are shown as follows: Phase II – pressure history (Figure 4-8) and type curve (Figure 4-9); Phase III – pressure history (Figure 4-10) and type curve (Figure 4-11); Phase IV – pressure history (Figure 4-12) and type curve (Figure 4-13). For each phase, the cycle shown is reasonably representative of all cycles in that phase. Unlike the Phase I cycle, model results from the later phases do not show a significantly greater misfit when s_d is fixed rather than allowed to vary.

The fits in the later phases are generally better than in Phase I, particularly compared to the time prior to 1998 when there were more variations in flow rate,

with large variations in the estimated parameters. In Phase I, the modeling produced large variations in the estimated parameters and errors in the predicted pressures at times exceed 5%. In Phase II, the fits are significantly improved with errors mostly within 2%. In Phases III and IV, the errors are generally less than 1 to 2%. While the magnitude of the pressure falloff during the shut-ins is matched relatively well, the shapes of the falloff curves are not well-matched in the later phases, which suggests an effect that is not accounted for in the model, such as closing of fractures during shut-in periods.

Whether or not s_d is fixed, the models generally fit the data within 1-2% error for the build-up cycles in Phases III and IV, with slightly higher errors in Phase II and significantly higher errors in Phase I. Errors tend to be lowest in periods of continuous flow, and highest at the beginning of cycles and around mid-cycle shut-ins.

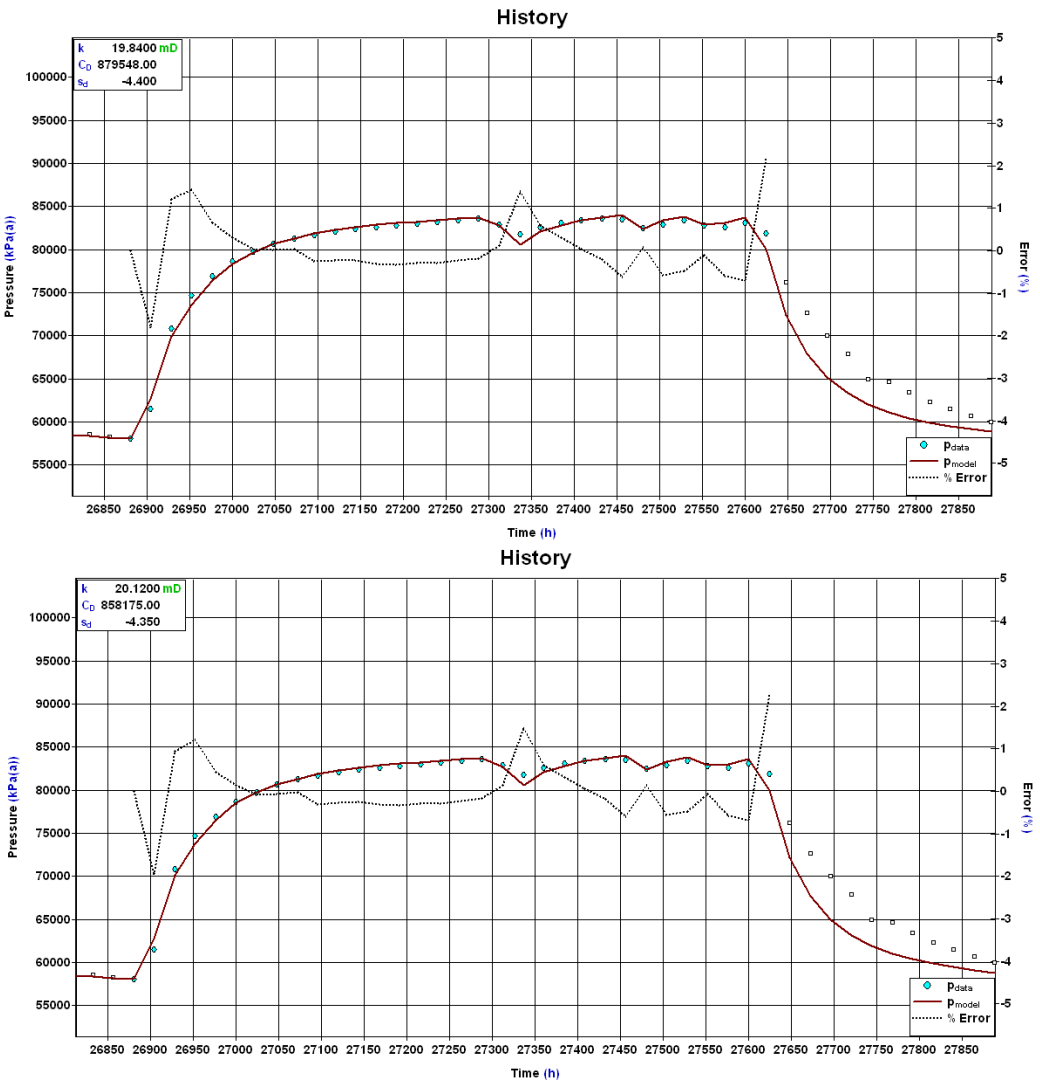

Figure 4-8. Recorded (blue dots) and modeled (red line) downhole pressures and percent error (dashed line) for an example Phase II cycle, beginning July 26, 1999, allowing all 3 parameters to vary (top) and fixing s_d at -4.35 (bottom). Recorded downhole pressures are calculated by adding a constant value of 6822 psi to measured surface pressures.

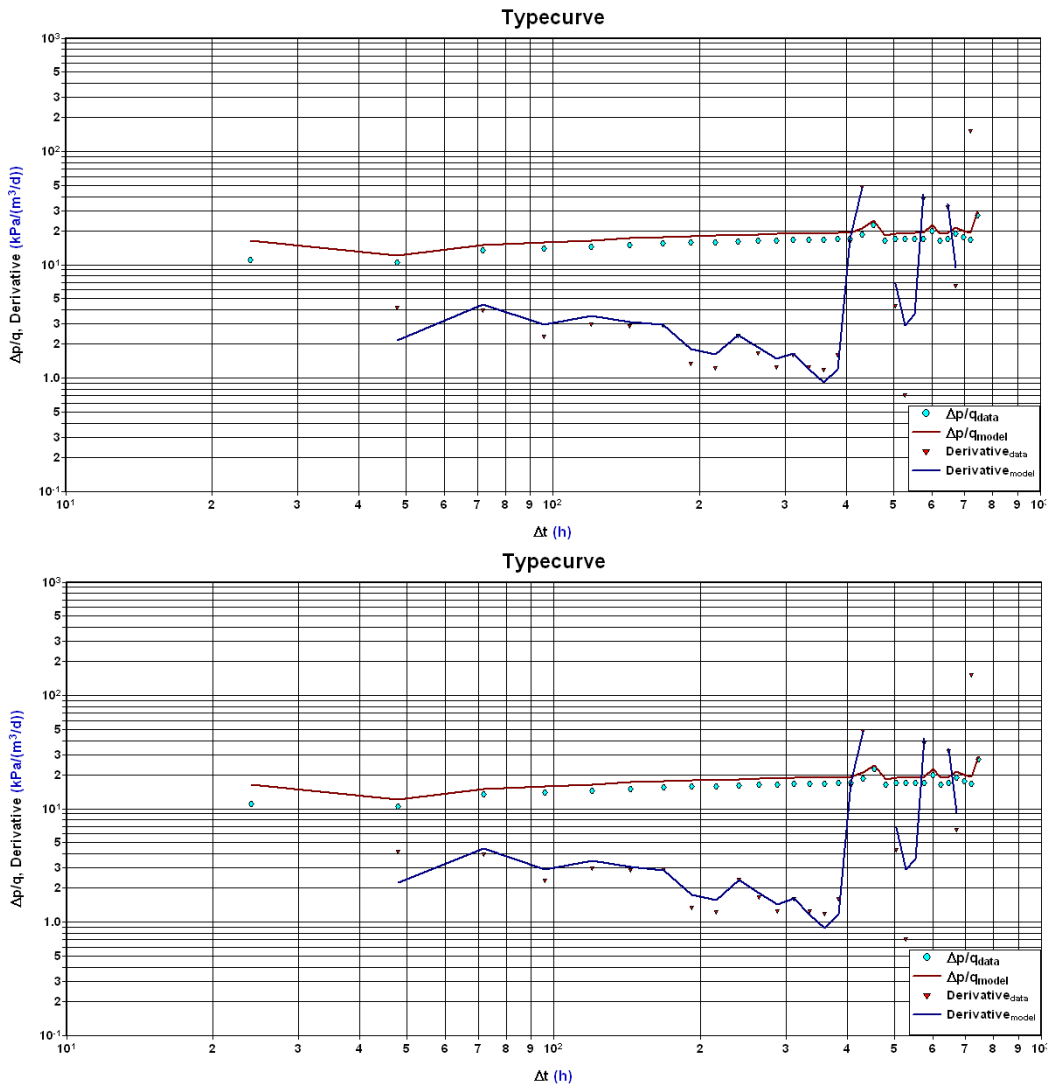

Figure 4-9. Recorded (blue dots) and modeled (red line) values for change in pressure (Δp) divided by flow rate (q), and the recorded (red triangles) and modeled (blue lines) values for the time derivative of Δp/q for an example Phase II cycle, beginning July 26, 1999, allowing all 3 parameters to vary (top) and fixing s_d at -4.35 (bottom).

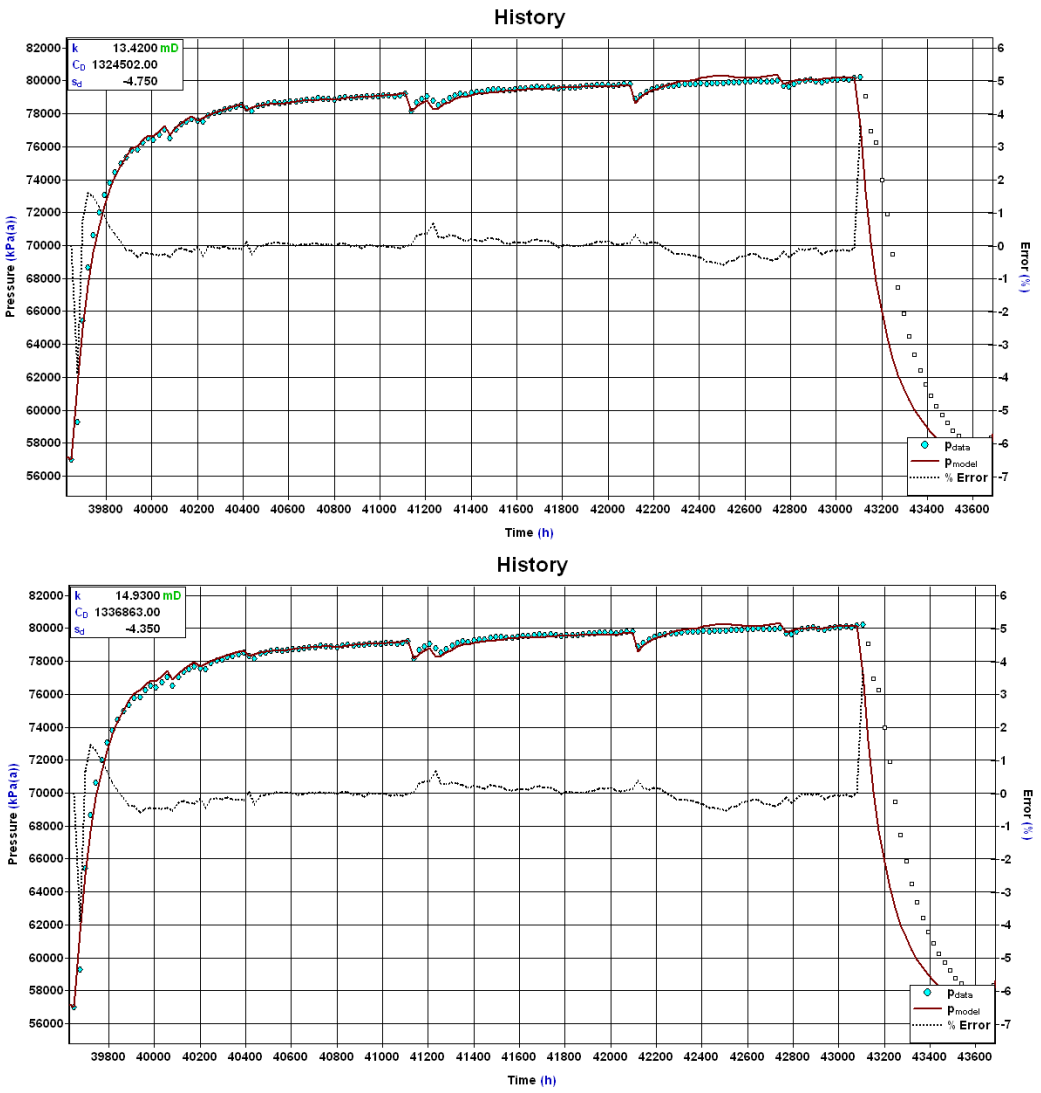

Figure 4-10. Recorded (blue dots) and modeled (red line) downhole pressures and percent error (dashed line) for an example Phase III cycle, beginning January 8, 2001, allowing all 3 parameters to vary (top) and fixing s_d at -4.35 (bottom). Recorded downhole pressures are calculated by adding a constant value of 6822 psi to measured surface pressures.

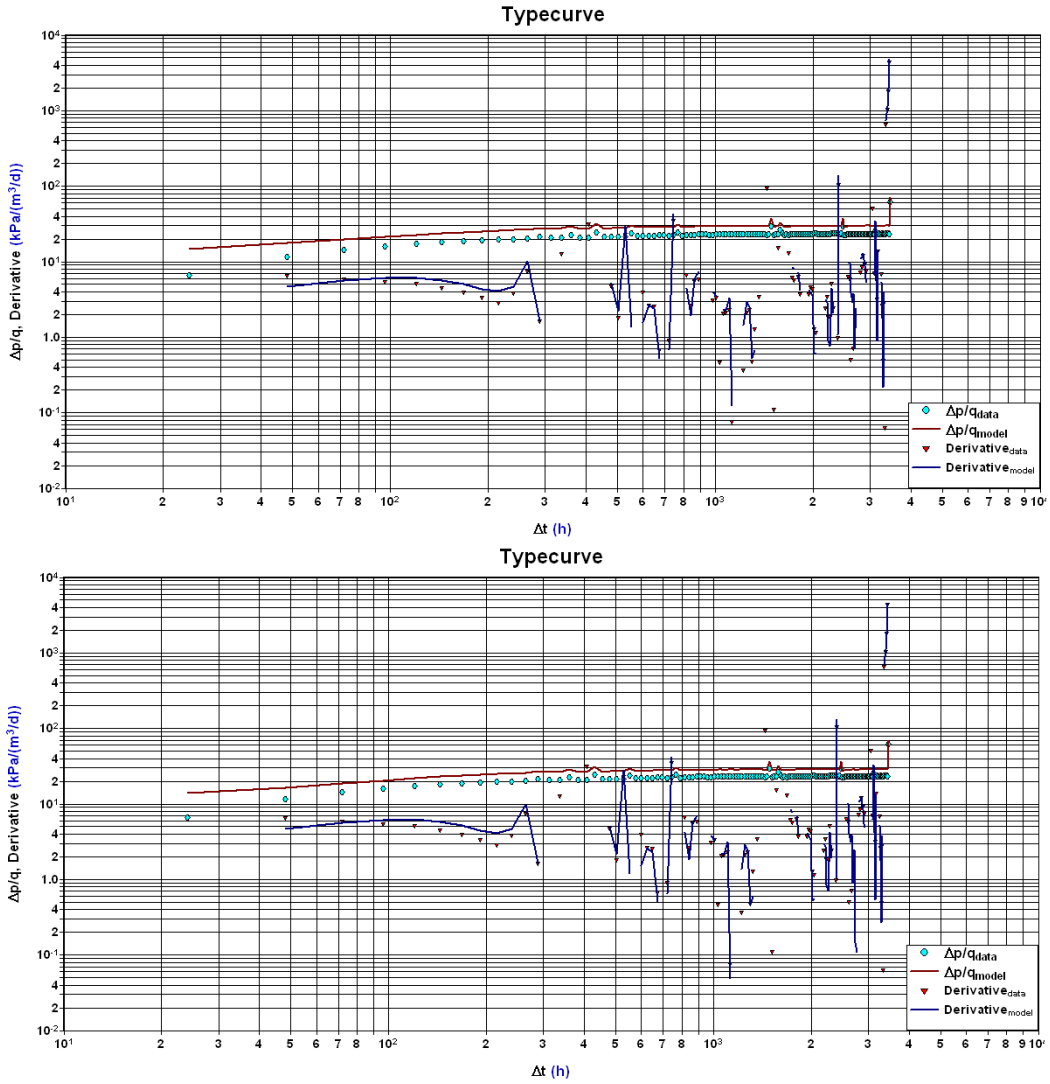

Figure 4-11. Recorded (blue dots) and modeled (red line) values for change in pressure (Δp) divided by flow rate (q), and the recorded (red triangles) and modeled (blue lines) values for the time derivative of Δp/q for an example Phase III cycle, beginning January 8, 2001, allowing all 3 parameters to vary (top) and fixing s_d at -4.35 (bottom).

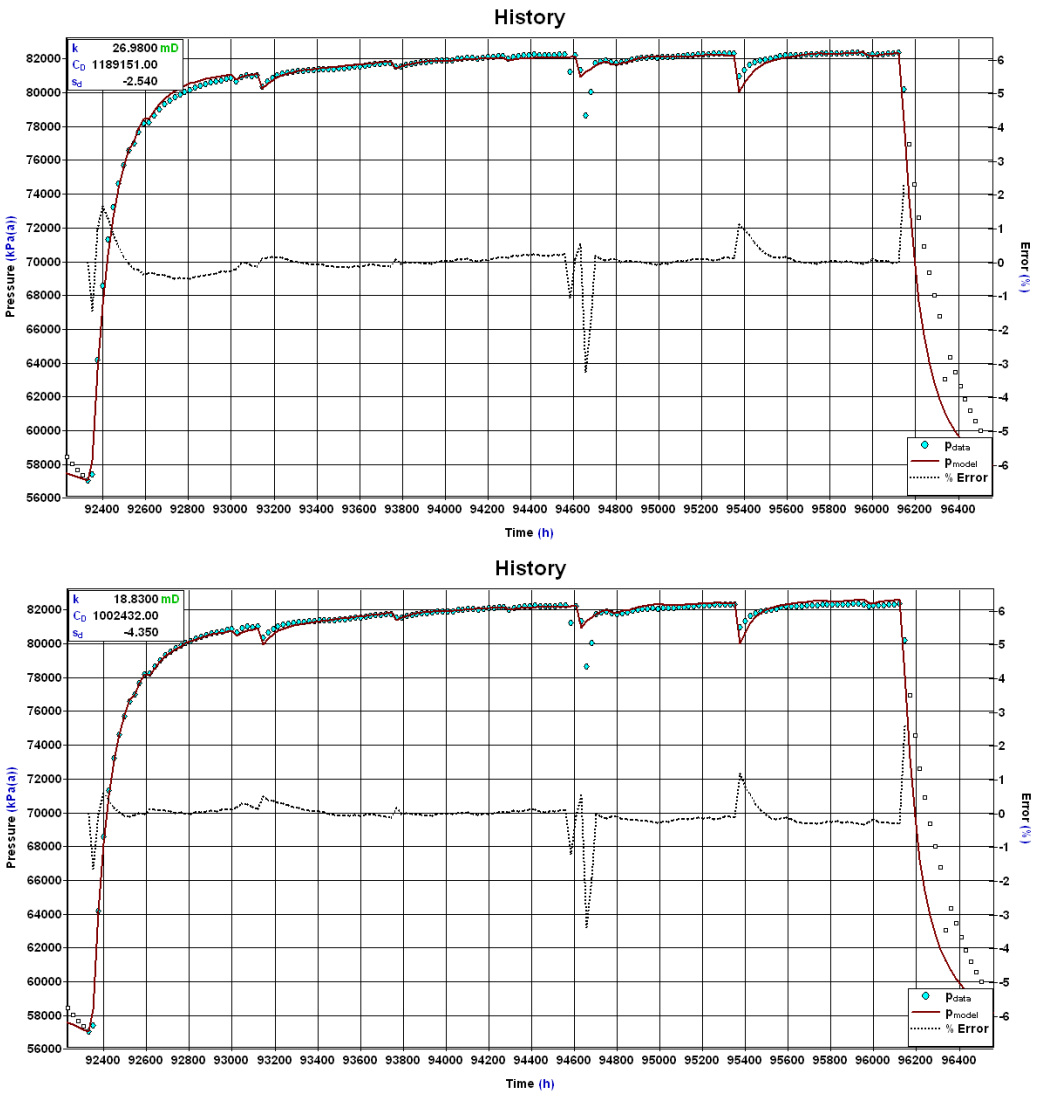

Figure 4-12. Recorded (blue dots) and modeled (red line) downhole pressures and percent error (dashed line) for an example Phase IV cycle, beginning January 14, 2007, allowing all 3 parameters to vary (top) and fixing s_d at -4.35 (bottom). Recorded downhole pressures are calculated by adding a constant value of 7133 psi to measured surface pressures.

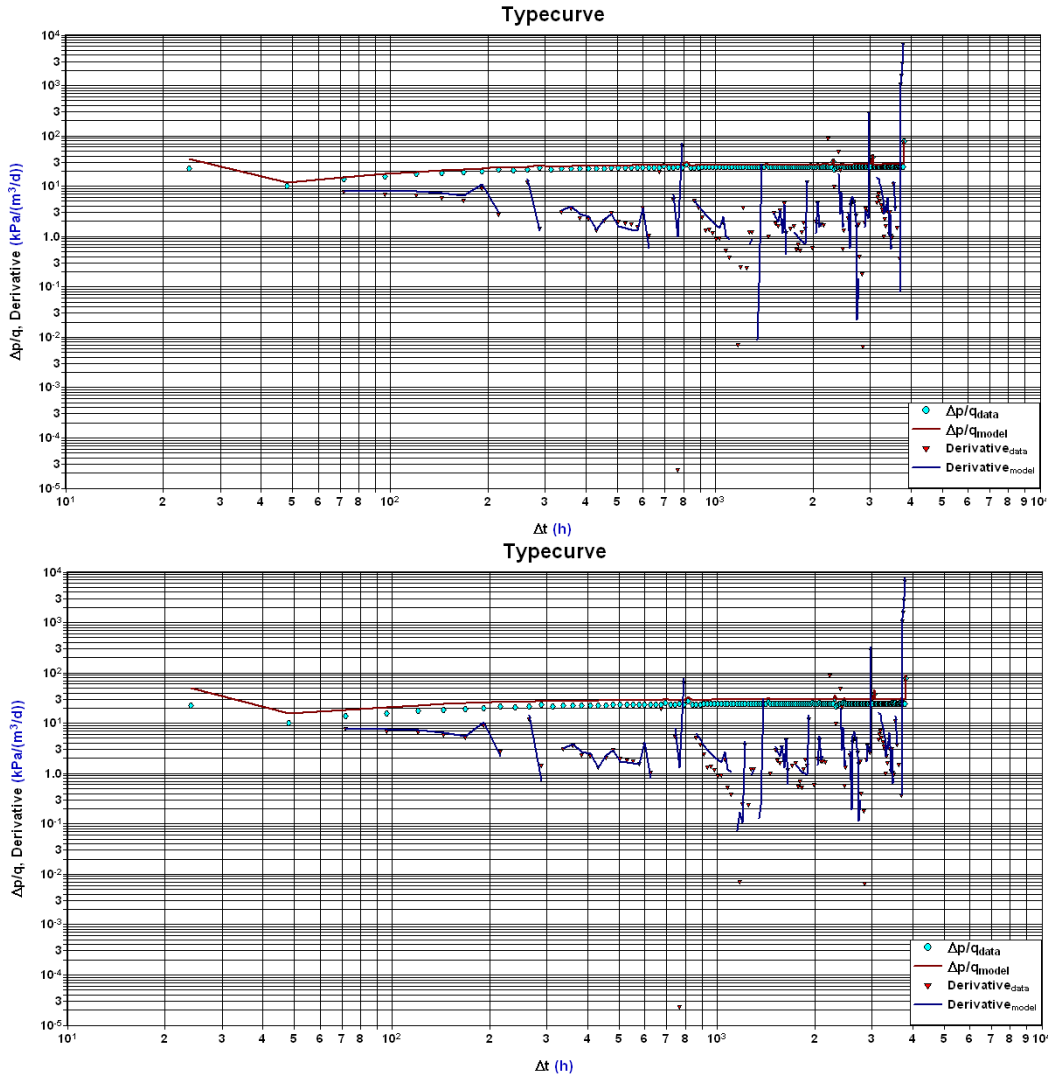

Figure 4-13. Recorded (blue dots) and modeled (red line) values for change in pressure (Δp) divided by flow rate (q), and the recorded (red triangles) and modeled (blue lines) values for the time derivative of Δp/q for an example Phase IV cycle, beginning January 14, 2007, allowing all 3 parameters to vary (top) and fixing s_d at -4.35 (bottom).

The earlier portions of the type curves shown above appear to indicate primarily the transition from wellbore storage to radial flow, with radial flow (identifiable as a flat spot on the derivative curve) emerging around 1000 hours in Phases II-IV, and possibly earlier in Phase I. However, the amount of scatter in the derivative for all phases, much of which is related to changes in flow rate, makes it difficult to resolve the precise times that these transitions occur. Boundary effects, which cause an increase in the derivative following the radial flow period, are not observed.

Daily-averaged pressure-flow data were used in these simulations because the pre-2003 high-resolution data are presently not in an accessible format. The modeling results suggest that daily-averaged data are insufficient to resolve the wellbore storage period, and that the high-resolution data will be needed.

It has been noted that the rate of increase in the maximum pressure during each cycle appears to be greater since 2010 than previously (Figure 4-1), which has led to speculation that the pressures are being affected by a reservoir boundary or a zone of decreased permeability. Figure 4-14 shows actual and modeled pressures for a single set of parameters for the cycles from April 2009 through March 2013. The mismatch between the observed and modeled maximum pressures is relatively small for all cycles, suggesting that a radially symmetric model with infinite-acting boundaries is adequate to model the data at this time. It is likely that the increase in maximum pressure in recent years is related to a decrease in the number of unscheduled maintenance shut-ins, leading to a decrease in the total shut-in time per cycle.

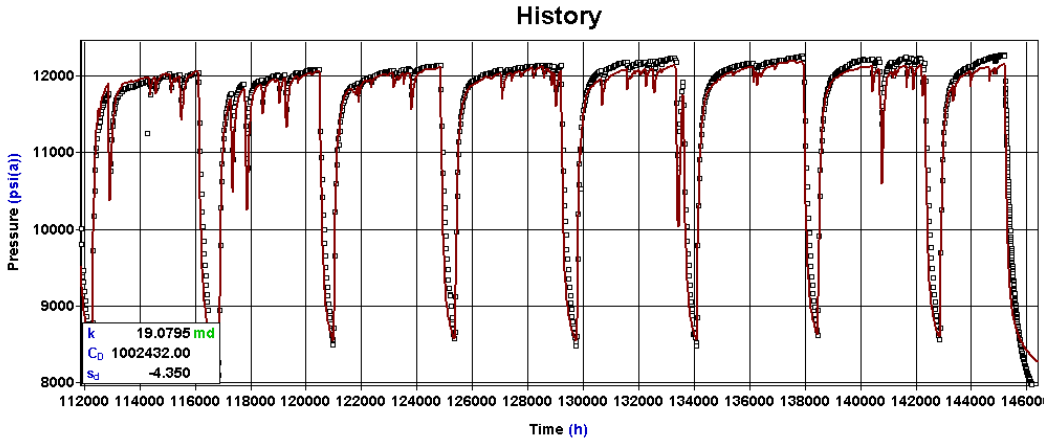

Figure 4-14. Recorded (open squares) and modeled (red lines) downhole pressures for the time period from April 2009 to March 2013. The model uses a single set of input parameters, as shown in the bottom left corner. Recorded downhole pressures are calculated by adding a constant value of 7133 psi to measured surface pressures.

4.5 Evaluation of Pressures for Alternative Injection Scenarios

If we assume that the current reservoir characteristics will remain constant in the near future, it is possible to model the maximum pressures for a range of injection scenarios. While it is difficult to determine the precise relationship between seismic hazard and pressures near or away from the well, a highly simplified assumption is that higher maximum pressures at the well correlate with increased seismic hazard. Thus, it follows that for a given injection volume per unit time, the injection scenario that produces the lowest pressure (maximum and/or average) during that time is preferable, subject to logistical constraints.

To explore the relative differences of various injection scenarios, we use the radially symmetric model with boundary conditions developed in the preceding

section. The parameters used for the forward modeling are k=18.47, s_d=-4.23, and C_D=1.06×10^6. These parameters are obtained from the fit to the cycle beginning October 19, 2011, allowing k, s_d, and C_D to all vary simultaneously. The parameters from this cycle were chosen because it was the most recent full-length cycle with good data for the entire cycle, as the cycle beginning April 16, 2012 had a period near the beginning of the cycle where data was not recorded consistently, degrading the quality of fits, and the most recent cycle was substantially shorter than the other cycles, due to the premature shut-in that followed the earthquake of January 24, 2013. The entire flow history up to January 24, 2013 is used in the modeling, and a shut-in time of 83 days is assumed before resuming flow. The starting pressure is adjusted to constrain the modeled pressure to match the observed pressure at the end of the 83-day shut-in.

In deciding how to proceed with future injection, there are several factors that could be adjusted, including the flow rate and the frequency and duration of shut-ins.

The first range of scenarios involved fixing the flow rate and total shut-in duration during a 1-year period, and adjusting the duration of individual shut-ins. The flow rate was fixed at 230 gpm and the total shut-in time per year was fixed at 40 days, in line with the past shut-in schedule. Scenarios varied from one 40-day shut in at the end of the year to 40 one-day shut-ins distributed evenly throughout the year. Both the maximum and average pressures increase as the shut-in length increases, suggesting that a large number of short shut-ins may be more effective than a small number of long shut-ins at controlling pressures at the well, as illustrated in Figure 4-15.

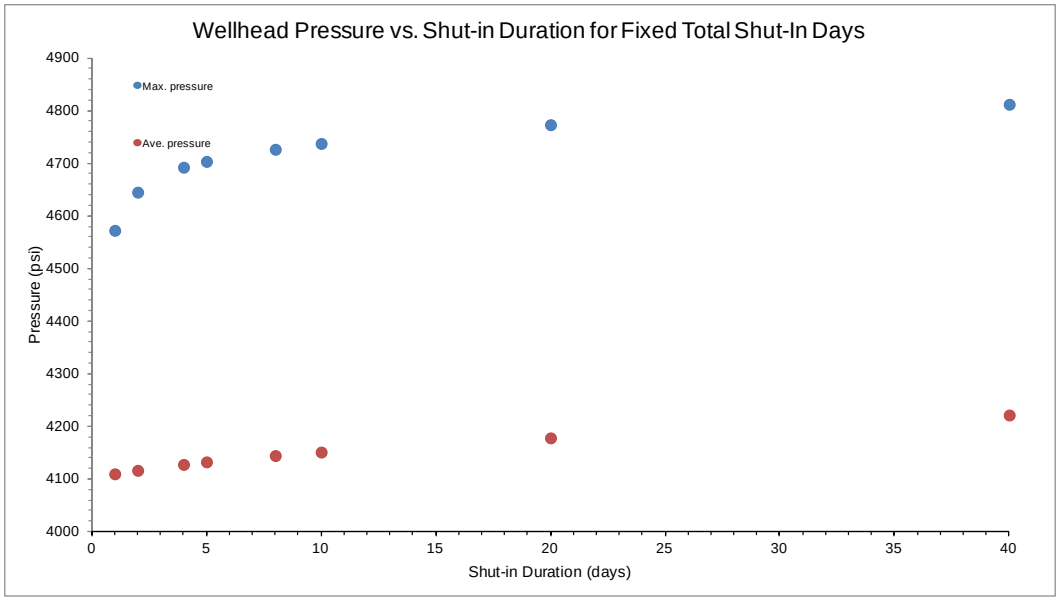

Figure 4-15. Maximum and average pressures for a variety of 1-year scenarios with varying shut-in schedules. Flow rate is fixed at 230 gpm and total shut-in time is fixed at forty days. Scenarios range from one 40-day shut-in to 40 one-day shut-ins.

We consider a number of scenarios to compare the effect of variable shut-in duration on pressures. In these scenarios, shut-in durations are varied between 1 and 40 days, but the total annual number of shut-in days and amount of fluid injected is kept fixed. All shut-ins for a particular scenario are evenly-spaced and of equal-length. The reason for keeping the same number of total shut-in days for all scenarios is to account for the assumption that a certain number of maintenance days each year are required for operations. For this idealized case, we further assume that maintenance can be carried out in 1-day increments, and that 40 days of maintenance per year is a reasonable average total number. The general results do not depend on the specific increment or the total number of shut-in days.

The modeling results shown in Figure 4-15 suggest that shorter, more frequent shut-ins result in a lower pressure increase, given a specified yearly total volume of injection total and a total number of shut-in days. To understand the basis for this result, it is useful to consider the limiting case of an infinite number of shut-ins of infinitely short duration, and equivalent to injection at a constant rate such that the total yearly volume of fluid injected remains the same as the scenarios with shut-ins. For a constant injection rate q, injection duration t_I, and shut-in duration t_S, injecting at the average injection rate $\bar{q} = q\,t_I / (t_I + t_S)$ produces the same total injection volume over the full injection cycle $t_I + t_S$. As an example, if we consider a typical 6-month injection cycle with a single 20-day shut-in, and a constant injection rate of 230 gpm, then the same total volume could be injected using an average injection rate of 205 gmp and no shut-ins. Using the simple Horner (1951) model described by Equation (4.3), and ignoring wellbore storage and skin effects, the pressure increase for these two cases is quite different because the model predicts that the change in pressure is proportional to the product of injection rate and the logarithm of injection duration. For this model, the difference in injection rate for these two cases has a much stronger effect than the difference in injection duration, and therefore the scenario with the lowest injection rate results in the lowest pressure increase. This effect is illustrated in Figure 4-16.

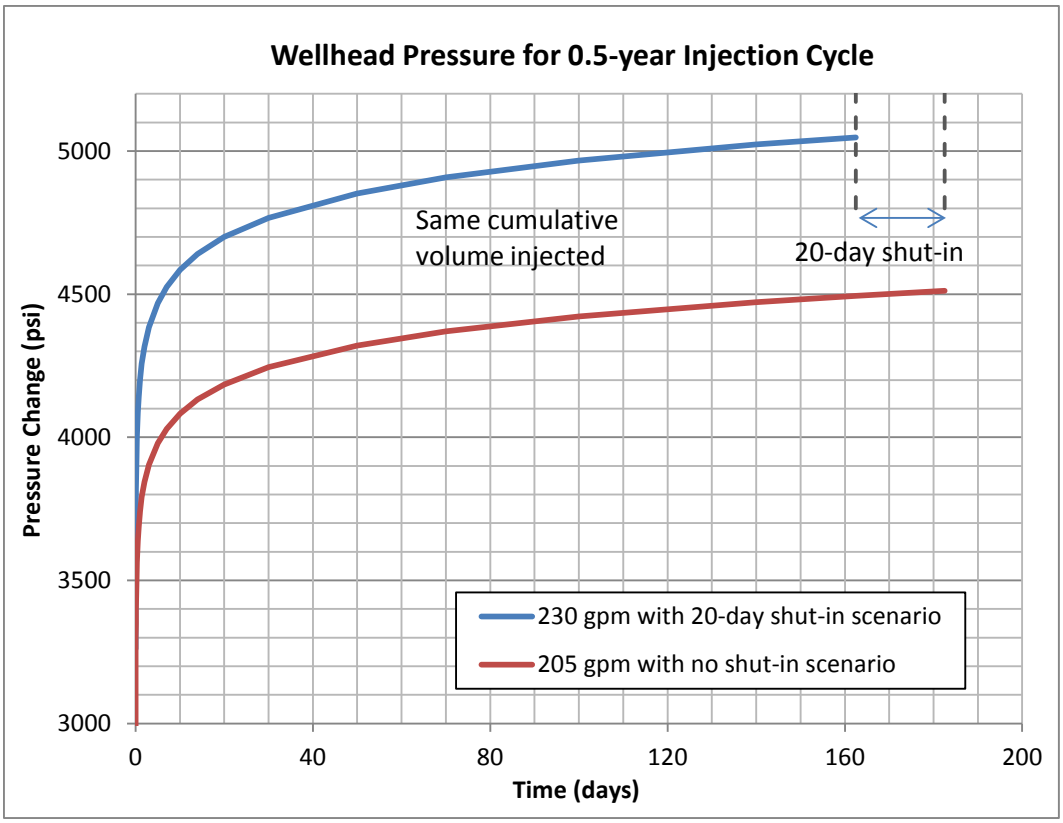

Figure 4-16. Pressure increases predicted by the simple Horner (1950) model for the cases of a 6-month injection cycle with either a 20-day shut and an injection rate of 230 gpm, or no shut in and an injection rate of 205 gpm. In each case the total amount injected over the 6-month period is the same, but injecting at the lower flow rate produces a lower pressure increase even though the duration of injection is longer. This results because the slope of the pressure curve is greatest at the start of injection, and continues to decrease with time, and because the pressure increase is scaled by flow rate. For this illustration we assumed the following model parameters: k = 18 md, h = 100 ft, φ = 0.03, μ = 1.03 cP, and $c_t = 1.93\times10^{-6}$ psi^{-1}. For simplicity, the pressure fall-off curve for the 20-day shut-in scenario is not shown. This model is for illustration only and is not a prediction of actual PVU surface pressures.

To further investigate the effects of reducing the flow rate on injection pressures, several scenarios with varying average flow rates and shut-in lengths are modeled. In these scenarios, we assume a constant average yearly injection rate (or equivalently, a constant injection volume). The scenarios last for 1 year, with a single shut-in occurring after the total injection volume has been reached. The injection volume is fixed at 10^8 gallons, which is near the average volume per year injected in recent years. Scenarios range from continuous injection for the entire year at a flow rate of 190.26 gpm to injection at a flow rate of 380.52 gpm for half the year followed by a shut-in for the remainder of the year.

The scenarios with a higher flow rate reached significantly higher maximum pressures during the year, as illustrated in Figure 4-17. This suggests that for a given injection volume, reducing the flow rate is a more effective way of reducing

the maximum pressures than increasing the shut-in time. The average pressures also increase as the flow rate increases, although by a much smaller amount.

However, this interpretation relies on the assumption that effective permeability is independent of flow rate, which may not be valid. As discussed in Section 4.4.1, modeled effective permeabilities appear to have been higher during the period when flow rate was higher, so it is plausible that if flow rate were to be decreased, effective permeability would also decrease. However, the potential magnitude of this decrease, if it occurs at all, is unknown.

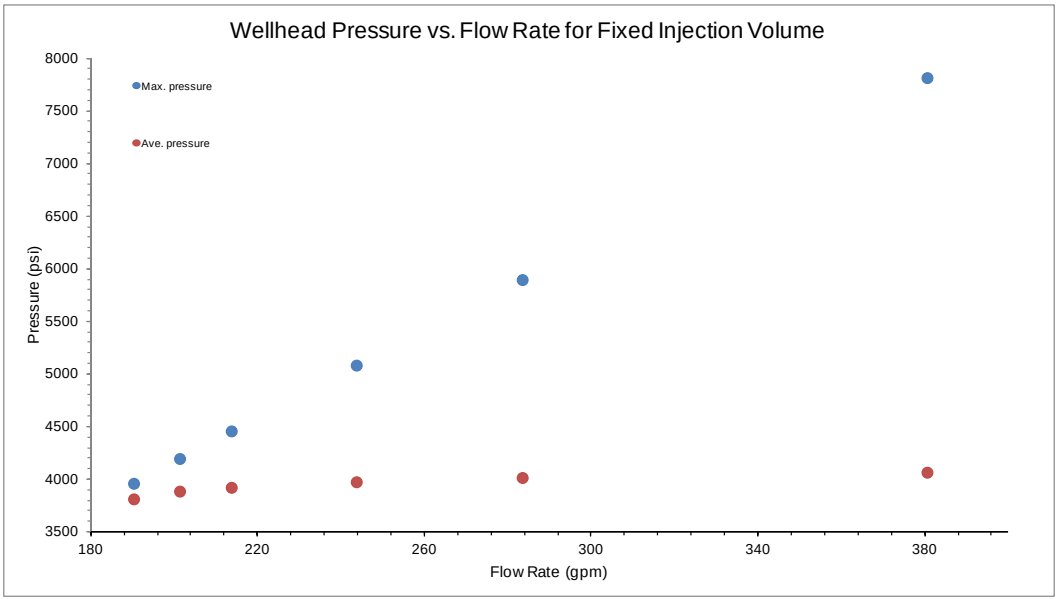

Figure 4-17. Maximum and average pressures for a variety of 1-year scenarios with varying flow rates, with a shut-in occurring for the remainder of the year once a fixed volume of 10^8 gallons is reached.

Since not all of these scenarios are logistically feasible, scenarios are also created using the four available plunger sizes of 2.125", 2.000", 1.875", and 1.750", which correspond to injection rates of 230 gpm, 204 gpm, 180 gpm, and 156 gpm, respectively. The values of k and C_D obtained by fitting the cycle beginning October 19, 2011 with s_d fixed at -5.028 were used. Several injection scenarios are considered, including shut-ins of 5, 10, 15, and 20 days every 3 or 6 months, and no shut-ins.

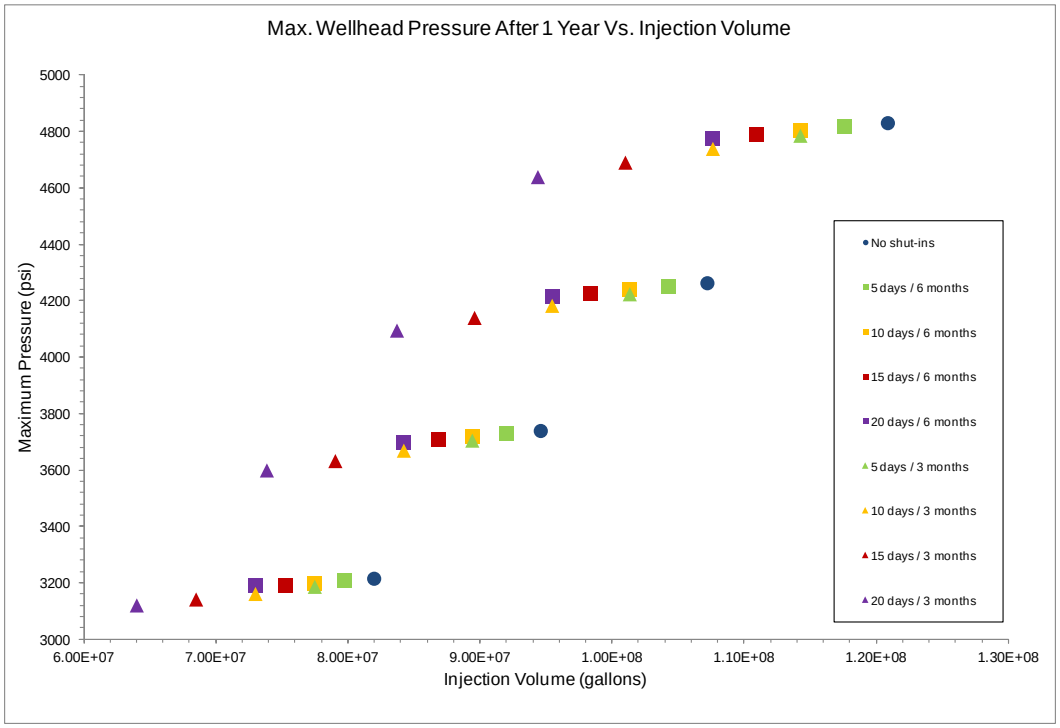

Figure 4-18. Maximum pressure vs. injection volume for a variety of injection scenarios with varying shut-in schedules and flow rates. In each data series, the data points indicate flow rates from left to right of 156 gpm (1.750" plungers), 180 gpm (1.875" plungers), 204 gpm (2.000" plungers), and 230 gpm (2.125" plungers).

Maximum pressures obtained after 1 year were compared for the four plunger-size scenarios, and the results are shown in Figure 4-18. For a given injection volume, schedules with fewer shut-in days appear to have a smaller maximum pressure, confirming the results found in the previous set of scenarios. If we chose a maximum pressure not to be exceeded in a year of injection, this graph could be used to select the injection scenario that injected the greatest volume while staying below that pressure.

To investigate the effects of possible changes in effective permeability, models were also created using a fixed injection schedule and varying the effective permeability and flow rate, using the four available plunger sizes. The fixed schedule was comparable to the past injection schedule, with two 20-day shut-ins per year. Three permeabilities are considered: 16.18 mD, 24.19 mD, and 18.47 mD, corresponding to the minimum and maximum permeabilities fit in Phase IV with s_d fixed at -4.35 and the permeability considered in the previous model, respectively. The values for s_d and C_D from the previous model were maintained. The maximum pressures obtained over 1 year of injection are shown in Figure 4-19, which shows that even with a range of only about 8 mD, the effective permeability has a significant effect on the maximum pressure.

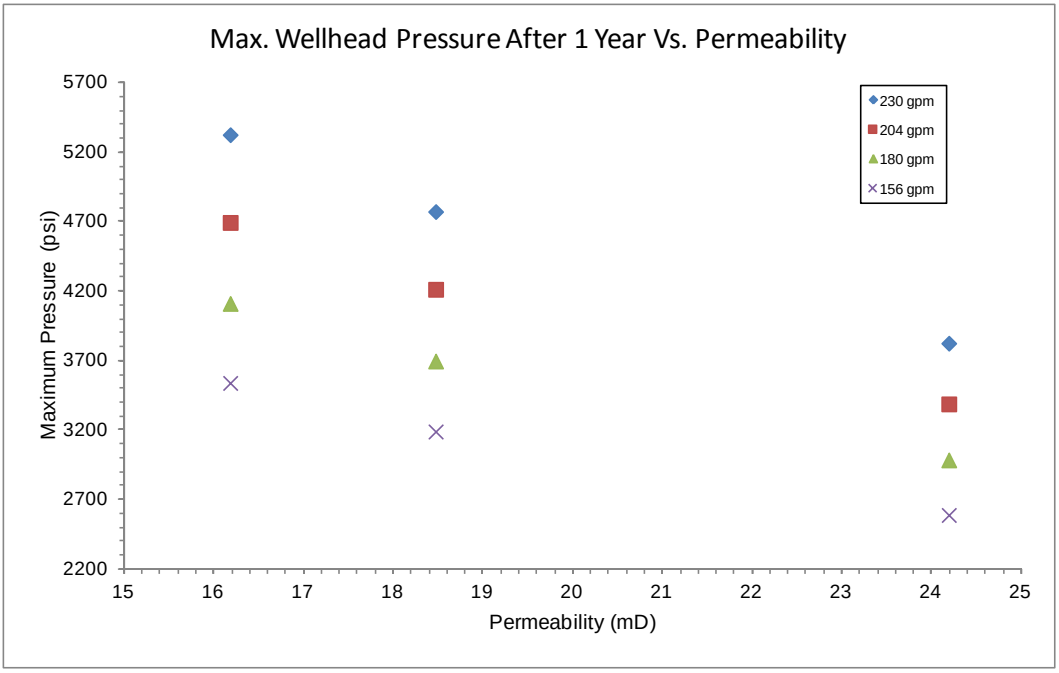

Figure 4-19. Maximum pressures obtained over one year of injection for 3 different permeabilities and 3 flow rates, with 2 evenly spaced 20-day shut-ins per year.

4.6 Pressure-Flow Modeling Discussion

If we assume both that the current reservoir model is correct and that it will remain valid for projecting future system responses, even in the case of significant changes to the flow rate and injection schedule, then it follows that injection at a lower flow rate, with shut-ins that are significantly shorter than the current 20-day shut-ins, would be the most effective scenario evaluated for the reduction of both maximum and average wellhead pressures.

However, both these assumptions are subject to significant uncertainty. While a model with infinite-acting boundaries is adequate to fit the present data, it is possible that boundary effects may become significant in the future, which would lead to higher pressures. Also, temperature effects likely play a significant role in holding open fractures in the near wellbore region, and it is unknown whether these phenomena due to temperature would be sufficient to hold open these fractures if a lower injection flow rate were to be used, or whether decreasing the injection rate would lead to fracture closure, reducing the effective permeability.

Additionally, even if changes to the flow rate and schedule are successful in reducing the pressures at the well, it is unknown how these pressures correlate with pressures away from the well, or more importantly, with seismic risk.

5 Discussion

We interpret the shallow seismicity occurring in the vicinity of the PVU injection well as induced by fluid injection and occurring in response to a decrease in the effective normal stress on pre-existing fracture surfaces. Fracture initiation is assumed to be adequately described by a Coulomb fracture criterion (Jaeger, 1969), and the observed seismicity is interpreted to be the result of frictional failure due to shearing. Focal mechanisms analyzed to date are consistent with simple shear failure; tensile-failure events have not been recognized in the recorded data (Ake and others, 2005).

During fluid injection, the effective normal stress on pre-existing fractures can decrease as a result of the following effects: increasing pore pressure, redistribution of stress (from accommodation of the injected fluid into the rock or from the occurrence of previously induced earthquakes), or cooling and shrinking of the rock matrix. The latter thermodynamic effect is important in geothermal areas but is unlikely to be a dominant factor at PVU, except possibly in the near vicinity of the injection well. Changes in pore pressure and stress redistribution are likely the major triggering mechanisms for the earthquakes induced by fluid injection at PVU.

Simple correlation of PVU injection pressure and earthquake data suggests that pore pressure increase is a dominant factor contributing to the rate and magnitude of induced seismicity occurring within 5 km of the injection well, but no clear correlation is observed for earthquakes occurring at greater distances, as shown in Figure 2-22, and discussed in greater detail in Block and Wood (2009; 2010). Since there are no observation wells for measuring in-situ pore pressures directly at PVU, we use long-term averaging of the injection pressures as a simplistic method of accounting for the time delay and amplitude modulation of pressure variations at the injection well as the pressures propagate away from the well. To correlate pressure trends with the near-well seismicity data, the pressure averaging must be done over longer time windows for later periods. The seismicity may take progressively longer to respond to changes in injection pressures both because more of the seismicity occurs at greater distances from the well for later time periods and because the size and complexity of the reservoir increases over time. While acknowledging that this method is very simplistic, the general correlation between relatively high long-term average injection pressures and increased rates and magnitudes of induced earthquakes in the near-well region suggests that pore pressure affects both the rate and magnitudes of induced seismic events occurring within 5 km of the well (Figure 2-22). The same analysis, however, does not show a correlation between injection pressure and the rates and magnitudes of earthquakes occurring at distances greater than 5 km, such as within the NW cluster (Figure 2-22).

Roeloffs and Denlinger (2009) suggested that seismicity was initially triggered in the NW cluster by stress redistribution. This hypothesis stems from the fact that the seismicity in the NW cluster began only one year after the start of long-term injection operations, too soon for significant pore pressure changes to have propagated 6 to 8 km from the well, based on results from their axisymmetric porous-medium fluid flow model.

Ake and others (2005) suggested an alternative explanation for the early onset of the NW-cluster seismicity: one or more northwest-trending faults allow for fluid flow, and relatively rapid propagation of pore pressure, from the vicinity of the injection well to the NW cluster. The concept of northwest-trending, relatively high-permeability fault zones acting as fluid and pore pressure conduits is consistent with the mapped geology and the local stress field. A series of deep, northwest-trending normal faults was mapped during early PVU geophysical investigations (Block and others, 2012; King and others, 2014). The subparallel alignment of these faults (~N55°W), the P axes of N64°W-N67°W determined from the focal mechanisms of induced events (Ake and others, 2005; Block and others, 2015), and the direction of maximum horizontal stress of N84°W interpreted from borehole televiewer data (Steve Hickman, personal communication, 2003) suggests that the northwest-trending basement fault zones may tend to dilate and accommodate fluid flow during PVU injection. In this model, earthquakes occurring in the NW cluster, such as the January 2013 event, are inferred to be induced primarily by pore pressure changes.

The lack of correlation between the average injection pressures at the well and the rates and magnitudes of earthquakes occurring in the NW cluster, as well as the lack of correlation between the near-well and NW-cluster seismicity patterns (as shown in Figure 2-22), is difficult to explain using a simple model of relatively rapid pore pressure response between the well and the NW cluster. A possible explanation for this discrepancy is that, if the basement fault zones are acting as conduits for fluid flow and pore pressure propagation to the NW cluster, then perhaps these pathways are pressure-sensitive. When the pore pressures in the vicinity of the well increase to sufficiently high levels, the conduits for fluid flow and pore pressure propagation to the northwest may open, and pore pressures may then increase relatively quickly in the NW cluster. When pore pressures in the vicinity of the injection well fall to sufficiently low levels, the conduits may close and the pressures in the NW cluster may then be relatively isolated from further pressure reductions at or near the injection well. Studies of the local geology and the spatial and temporal patterns of PVU-induced seismicity indicate that the NW cluster may be partially surrounded by impermeable boundaries (King and others, 2014), and therefore elevated pore pressures in the NW cluster may require an unusually long time to decay. This type of pressure-sensitive response may help explain the lack of correlation between the seismicity pattern in the NW cluster and both the seismicity pattern in the near-well region and the temporal variation in average injection pressure.

The occurrence of the January 2013 M_L 4.4 earthquake, at a distance from the injection well nearly four times greater than the radial distances of previous PVU-induced earthquakes of comparable size, is part of a broader trend of recently changing seismicity patterns related to PVU fluid injection. Patterns of PVU-induced seismicity largely stabilized for a decade following a decrease in the injection flow rate by one-third in mid-2000. Since 2010, however, the seismicity patterns have been changing, with seismicity rates increasing in some areas and seismicity occurring in previously aseismic areas. For example, a distinct group of earthquakes, now referred to as the SE cluster, developed in 2010 about 6 km southeast of the injection well. While the first detected SE cluster event occurred in 2004, a total of only 3 SE cluster events were recorded prior to 2010. From 2010 through 2012, 53 SE cluster events were recorded. Seismicity rates within the northern-valley areas have also changed in recent years. The number of northern-valley earthquakes recorded each year from 2000 (when the northern valley seismicity was first detected) to 2009 ranges from 2 to 33. In 2010, the rate increased markedly: 557 northern-valley earthquakes were recorded, with the majority occurring in a single swarm lasting just 16 days. Northern-valley seismicity rates remained elevated during 2011, with 113 earthquakes recorded, but declined back to pre-2010 rates during 2012, with just 10 events recorded. Beginning in mid-2010 and continuing through the present, several shallow earthquakes have been detected in the center of Paradox Valley. Three earthquakes were detected in 2010; two in 2011; and five in 2012. Although the total number of events is small (10 in 3 years), no earthquakes were detected beneath the floor of Paradox Valley in the 25 years of seismic monitoring prior to 2010. The renewed spatial expansion of seismicity and increased seismicity rates in recent years may be related to the trend of increasing injection pressures at the well.

The January 2013 earthquake did not occur on any of the subsurface normal faults that were mapped with seismic reflection surveys during early PVU geophysical investigations. As discussed above, most of these faults trend close to the estimated direction of maximum horizontal stress (Ake and others, 2005), and therefore they are not now optimally oriented for shear slip. Instead, most of the induced earthquakes observed at PVU, including the January 2013 event, appear to occur on favorably oriented pre-existing fractures that have been reactivated by injection (Block and others, 2015). Because these faults may not have significant vertical offset, they may be difficult to resolve on deep seismic reflection data. The distribution of precise relative-relocated hypocenters as well as focal-mechanism analyses provides a way to identify these faults (Block and others, 2014; Block and others, 2015).

A thorough analysis of seismic risk from induced seismicity at PVU would consider the rates at which damaging ground motions are likely to occur in the populated surrounding areas, and the likelihood of damage, economic loss, and potential life-loss given those loadings. Such an analysis is beyond the scope of

this report, and many of the required input parameters are not known with any degree of confidence. Necessary inputs to a typical seismic hazard analysis include mean seismicity rates, maximum magnitudes, and the magnitude distribution for induced seismicity, but these parameters have changed substantially at PVU over the lifetime of the project, making estimates for future behavior highly uncertain. An even bigger problem is that the precise relation between the seismicity rate and injection parameters which can be controlled (e.g., average flow rate, maximum injection pressure, shut-in duration, etc.) is poorly known. Additional unknown parameters include the attenuation of ground motions with distance, site-response properties (e.g., V_{S30} and basin depth), and the density and fragility of residences and other structures.

Long-term seismic hazard estimates will be difficult to make at PVU without developing models that are capable of relating induced seismicity to injection operations. Such models have not yet been developed for PVU, although it is possible that recent numerical modeling approaches could be used to estimate both the pressure response and the seismicity response to injection. Short-term seismic hazard estimates can be made by extrapolating recent seismicity parameters, however even these estimates are likely to include substantial uncertainty.

Simple pressure-flow modeling suggest some operational steps that could be taken to reduce the wellhead pressures observed in recent years, and to potentially reduce the rate of occurrence of induced earthquakes. If we assume that this model is valid and can provide useful predictions of future pressure response to injection, then it follows that injection at a lower flow rate, with shut-ins that are significantly shorter than the current 20-day shut-ins, would be the most effective scenario evaluated for the reduction of both maximum and average wellhead pressures.

However, the model assumptions are subject to significant uncertainty. While a model with infinite-acting boundaries is adequate to fit the present data, it is possible that boundary effects may become significant in the future, which would lead to higher pressures. The model assumes that reservoir permeability is independent of wellhead pressure, but it is possible that reduced injection pressure would result in reduced effective permeability, which could substantially reduce the amount of pressure reduction obtained from reducing the flow rates. Temperature effects may also play a significant role in holding open fractures in the near wellbore region, and it is unknown whether these phenomena due to temperature would be sufficient to hold open these fractures if a lower injection flow rate were to be used, or whether decreasing the injection rate would lead to fracture closure, reducing the effective permeability. Additionally, even if changes to the flow rate and schedule are successful in reducing the pressures at the well, it is unknown how these pressures correlate with pressures away from the well, or more importantly, with seismic risk

Results presented in this TM are primarily from analyses in progress before the January 24, 3013 earthquake, or that were done in the weeks immediately following it. The purpose of these analyses was to fulfill requirements of the Emergency Action Plan for operation of the PVU injection well, and to develop alternatives for operations to minimize the potential for additional felt earthquakes. Hence, this TM mostly contains analyses that could be completed quickly after the earthquake. Following completion of the initial draft of this report in April, 2013, more detailed analyses were conducted and submitted for publication in peer-reviewed scientific journals (Block and others, 2014; King and others, 2014; Yeck and others, 2014; Block and others, 2015), and results have been incorporated into the current draft of this TM where appropriate. Detailed analysis of a few remaining topics are in progress, including pressure-flow modeling and seismic hazard analysis, and are expected to be documented in peer-reviewed journal articles.

.

6 Conclusions

6.1 Analysis of the January 24, 2013 M_L 4.4 Earthquake

Our analysis indicates that the M_L 4.4 earthquake that occurred on January 24, 2013 (UTC; January 23, 2013 MST) was induced by long-term fluid injection into PVU injection well #1. This event is slightly larger than the M_L 4.3 earthquake of May 27, 2000, making it the largest PVU-induced event to date. It locates 8.2 km northwest of the injection well, a radial distance nearly four times greater than other PVU-induced earthquakes of comparable magnitude.

Because this event occurred closer to northern Paradox Valley - where much of the local population resides - than previous large induced earthquakes, strong ground shaking was experienced by many local residents. Ground motion recordings from a strong motion instrument located at the Paradox Community Center indicate a peak horizontal acceleration of 0.28 g. For frequencies above 2.5 Hz, the horizontal accelerations recorded in the town of Paradox were nearly 2 standard deviations higher than the mean value estimated by standard ground motion prediction equations for an earthquake of this size and distance. Possible reasons for the unusually large ground vibrations in northern Paradox Valley produced by this earthquake include: (1) site effects resulting form the local geologic structure, consisting of a thick salt section and soft soil layer overlying bedrock; (2) unusual diffraction effects related to the “salt wall”; or, (3) decreased attenuation of high-frequency ground motions resulting from the shallow focal depth.

The peak particle velocity generated by this earthquake in the town of Paradox was 6.2 cm/sec (2.4 in/sec, horizontal component). To put this in perspective, this ground vibration level is more than 3 times the 1.9 cm/sec (0.75 in/sec) limit set in the Department of Interior, Office of Surface Mining (OSM) regulations for control of vibrations from mine blasting. As a result, minor damage to structures located in northern Paradox Valley may have occurred.

6.2 Potential Future Seismicity

6.2.1 Short-Term Seismicity

The apparent insensitivity of NW-cluster seismicity to past injection operations suggests that either the response time of this seismicity to injection operations is very long (several years), or that the threshold for triggering earthquakes on the pre-existing faults in this area is low (earthquakes over a range of magnitudes may occur with very little stress or pore pressure perturbation). Hence, we must

conclude that the risk of additional felt earthquakes in the NW cluster, some comparable in magnitude to (or even larger than) the January event, will be significant regardless of any changes in injection operations that may occur.

6.2.2 Seismic Hazard Factors

Reliably forecasting the long-term behavior of induced seismicity at PVU is extremely difficult because of the large uncertainties involved. Here we summarize a few of the factors that we have examined in this report that relate to the long-term seismic hazard.

6.2.2.1 Geographical Distribution of Seismicity

PVU-induced seismicity has expanded spatially over time. Most of the earthquakes induced during the injection tests (1991-1995) occurred within 2.5 km of the injection well. During continuous injection operations (1996-present), clusters of induced earthquakes have developed in areas much farther from the injection well, with shallow, potentially-induced earthquakes now occurring as far as 16 km from the injection well. The geographical expansion of seismicity slowed markedly after the injection flow rate was reduced in mid-2000, and seismicity rates simultaneously declined. However, over the last 3 years, new areas of seismicity have appeared and the seismicity rates in other areas have increased. Some of the recent seismicity is occurring closer to the more-populated northern end of Paradox Valley than earlier seismicity.

The volume of the stimulated rock mass, as indicated by the clouds of induced seismicity, is orders of magnitude larger than the cumulative volume of fluid injected. One possible explanation for this, which is consistent with the dominance of clear linear patterns within the induced seismicity, is that the majority of the injected fluid is traveling through a network of discrete, pre-existing fractures and that very little of the fluid is entering the pore space within the larger volume of rock surrounding the well. This hypothesis is consistent with the natural low permeability of the target reservoirs. An implication of this hypothesis is that the pore pressures within these fractures may be substantially increased at large distances from the injection well, while pressures within the pore spaces in isolated sections of the rock mass not connected to the fracture network may be considerably lower. Pore pressure increase within fractures at large distances from the injection well may contribute to the occurrence of induced seismicity distant from the well, such as that in the NW cluster.

6.2.2.2 Seismicity Rates

Both the overall rate and magnitude distribution of PVU-induced seismicity has varied substantially over time. These characteristics also vary spatially, with, for example, the near-well region and NW cluster showing distinctly different trends. The temporal variation in rate and magnitude distribution makes it difficult to predict the future behavior of the induced seismicity. Any quantitative measures

of seismicity rates based on current characteristics or historical trends may not be extrapolated with confidence very far into the future. Also, because the seismicity appears to have a long response time to changes in injection operations, variations in the rates or magnitudes of induced earthquakes related to changes in injection operations may not be noticeable until several years after those operational changes occur.

6.2.2.3 Maximum Earthquake Magnitude

Studies indicate that the maximum magnitude of induced earthquakes may be related to several factors, including the cumulative volume of fluid injected, the volume of rock stimulated by injection, and both the magnitude of pore pressure and the spatial pore pressure gradient. The models considered here for examining the question of the maximum magnitude earthquake likely to be induced for a given injection site are simplistic, considering the effect of one of these variables at a time. An evaluation of the combined effects of multiple parameters is complex and beyond the scope of this report.

The maximum magnitudes of earthquakes induced at PVU over time show a general correlation with the cumulative volume of injected fluid. This correlation indicates that, as of the end of 2012, enough fluid has been injected to trigger a maximum earthquake with magnitude between 3.7 and 4.8. This model suggests that the maximum earthquake magnitude will increase as additional fluid is injected. However, because this relationship is logarithmic, the trend is largely determined by the early history of injection operations, including the fluid volume injected during the tests conducted between 1991 and 1995. This type of analysis does not provide enough resolution to evaluate whether the rate of increase in event magnitude as a function of fluid volume injected changed when the injection flow rate was decreased in 2000. If we assume that the same trend is valid for all periods of time, and if injection were to continue at the same average flow rate (as in 2000-2012) for an additional 5 years, then the relationship implies a maximum earthquake magnitude of between 3.8 and 4.9 at the end of 2017. After 10 years (end of 2022), the maximum magnitude estimate increases to 3.9 - 5.05.

A model that correlates maximum earthquake magnitude with volume of stimulated rock (as estimated by the spatial distribution of induced seismicity) indicates generally similar results as that above but allows for separate analyses for the near-well region and NW cluster. This model indicates a maximum earthquake magnitude of about 5.2 for the near-well area and about 4.4 for the NW cluster. According to this model, the majority of the risk for generating earthquakes of this size is due to the volume of rock mass that was stimulated by fluid injected prior to 2001. Since the spatial extent of the induced seismicity in the near-well and NW cluster areas has not expanded substantially since 2001, the corresponding estimates of volume of stimulated rock mass and maximum earthquake magnitude have not increased much since that time. This type of model suggests that the maximum earthquake magnitude will not increase

substantially beyond these current estimates unless the near-well or NW-cluster seismicity clouds expand in the future (either during or after additional injection). This model provides estimates of maximum earthquake magnitudes due to fluid injection that has already occurred at PVU, but it does not predict when these events may occur. Because of the potentially long time period over which pore pressure diffusion takes place, the largest induced earthquake could occur years after the risk has been elevated, and potentially after injection has ceased.

A general correlation between high average injection pressures and the rate and magnitudes of earthquakes induced within 5 km of the PVU injection well has been noted previously (Block and Wood, 2009). When long-term average injection pressures fall to sufficiently low levels, the occurrence of M 2.5+ near-well induced earthquakes ceases while smaller-magnitude events continue to occur. This analysis implies that the local pore pressure may need to exceed some threshold level in order for the largest-magnitude events to occur. A higher pore pressure perturbation for larger-magnitude earthquakes is also indicated by numerical modeling of pore pressure diffusion on a pre-stressed fault (Garagash and Germanovich, 2012). The empirical observations and numerical model imply that the risk of inducing large-magnitude earthquakes can be reduced if pore pressures are sufficiently lowered. While no such empirical correlation between injection pressures and the occurrence of seismicity at distances greater than 5 km from the well (such as in the NW cluster) has been observed, the numerical modeling nonetheless suggests that a reduction in pore pressure could potentially reduce the seismic risk in this area as well. The response of pore pressures in fractures located several km from the well to changes in injection operations is unknown however, both in terms of the magnitude of pressure change and the time delay for changes to occur.

The spatial gradient of the pore pressures may also play a role in triggering large-magnitude earthquakes. Finite element modeling of pressures and induced seismicity for an injection simulation shows a correlation between the largest-magnitude induced earthquakes and shallow spatial pressure gradients (Baisch and others, 2010). Results from this modeling are consistent with the observation that in many instances the largest injection-induced earthquakes occur after injection operations cease. Under this situation, pore pressure continues to rise in some areas after shut-in but with a shallower spatial gradient than during injection. The results are also consistent with the observation that in many cases the largest-magnitude events tend to occur near the edges of the stimulated region rather than closer to the injection well. Such a pattern is observed at PVU, with the largest induced earthquakes occurring near the edges of the near-well and NW-cluster regions. The implication of this modeling is that the magnitudes of PVU-induced earthquakes could continue to increase after injection operations are stopped at some point in the future, and that these large events are most likely to occur around the edges of the stimulated regions (including the NW cluster).

6.3 Injection Operations

Simple pressure-flow modeling performed using industry-standard well testing software does not indicate any measurable change in reservoir properties in recent years. Permeability and near-wellbore storage values appear to be stable. This modeling implies that the increase in injection pressures (and expanding seismicity) may be a natural consequence of long-term injection into a (potentially unbounded) reservoir with limited permeability.

The modeling also indicates that the current pattern of injection may not be the most efficient in terms of injecting a given volume of fluid with the least amount of pressure rise. In model simulations, the current injection scenario, in which 2 20-day shut-ins occur each year, causes a greater pressure rise than scenarios where the same volume of fluid is injected at the same rate but more frequent, shorter shut-ins are used. Simulations also suggest that the same volume could be injected with even less pressure rise if no shut-ins are used and instead the flow rate is decreased. However, because permeability may change substantially when flow rate or pressures decline (and fractures potentially close), these model simulations have significant uncertainties.

Pressure modeling indicates that keeping the same shut-in schedule and decreasing the flow rate from 230 gpm to 204 gpm, a decrease of approximately 11%, would decrease the maximum pressure seen in a 1-year period by about 570 psi relative to maintaining the same flow rate, assuming no change in permeability. The corresponding decrease in the annual average pressure is estimated to be 480 psi. Keeping the same flow rate and number of shut-in days but changing the shut-in schedule from 2 20-day shut-ins per year to 40 1-day shut-ins per year would decrease the maximum pressure by approximately 250 psi, and decrease the annual average pressure by about 70 psi, with no change in the injected volume. We expect that the combined effect of implementing both of these changes would be greater than either of the individual effects.

References

Abrahamson, N., and Silva, W., 2008, Summary of the Abrahamson & Silva NGA Ground-Motion Relations: Earthquake Spectra, v. 24, no. 1, p. 67-97.

Abramowitz, M., and Stegun, I.A., 1964, Handbook of Mathematical Functions with Formulas, Graphs, and Mathematical Tables: Washington, D.C., United States Department of Commerce, National Bureau of Standards.

Agarwal, R.G., Al-Hussainy, R., and Jr., H.J.R., 1970, An Investigation of Wellbore Storage Constant and Skin Effect in Unsteady Liquid Flow: I. Analytical Treatment: Society of Petroleum Engineers Journal, v. 10, no. 3, p. 279-290.

Ake, J., Mahrer, K., O, C.D., and Block, L., 2005, Deep-injection and closely monitored induced seismicity at Paradox Valley, Colorado: Bulletin of the Seismological Society of America, v. 95, no. 2, p. 664-683.

Aki, K., 1965, Maximum Likelihood Estimate of b in the Formula logN=a-bM and its Confidence Limits: Bulletin of the Earthquake Research Institute, v. 43, p. 237-237.

Alt, B., Henry, S., Kraeger-Rovey, C., Paulin, I.J., Ellison, D.T., Javernick, H.J., and Nelligan, M.T., 1980, Regulations of the Colorado Mined Land Reclamation Board for Coal Mining: Colorado Division of Minerals and Geology, 469 p.

Anderson, J.G., 1979, Estimating the seismicity from geological structure for seismic-risk studies: Bulletin of the Seismological Society of America, v. 69, no. 1, p. 135-158.

Anderson, J.G., and Luco, J.E., 1983, Consequences of slip rate constraints on earthquake occurrence relations: Bulletin of the Seismological Society of America, v. 73, no. 2, p. 471-496.

Bachmann, C.E., Wiemer, S., Woessner, J., and Hainzl, S., 2011, Statistical analysis of the induced Basel 2006 earthquake sequence: introducing a probability-based monitoring approach for Enhanced Geothermal Systems: Geophysical Journal International, v. 186, no. 2, p. 793-807.

Baisch, S., Vörös, R., Rothert, E., Stang, H., Jung, R., and Schellschmidt, R., 2010, A numerical model for fluid injection induced seismicity at Soultz-sous-Forêts: International Journal of Rock Mechanics and Mining Sciences, v. 47, no. 3, p. 405-413.

Barth, A., Wenzel, F., and Langenbruch, C., 2013, Probability of earthquake occurrence and magnitude estimation in the post shut-in phase of geothermal projects: Journal of Seismology, v. 17, no. 1, p. 5-11.

Bear, J., 1972, Dynamics of Fluids in Porous Media, Dover Publ.

Bender, B., 1983, Maximum likelihood estimation of b values for magnitude grouped data: Bulletin of the Seismological Society of America, v. 73, no. 3, p. 831-851.

Berrill, J.B., and Davis, R.O., 1980, Maximum entropy and the magnitude distribution: Bulletin of the Seismological Society of America, v. 70, no. 5, p. 1823-1831.

Biot, M.A., 1941, General Theory of Three-Dimensional Consolidation: Journal of Applied Physics, v. 12, no. 2, p. 155-164.

Block, L., and Wood, C., 2009, Overview of PVU-Induced Seismicity from 1996 to 2009 and Implications for Future Injection Operations: Bureau of Reclamation, 16 pps. p.

Block, L., Yeck, W., King, V., Derouin, S., and Wood, C., 2012, Review of Geologic Investigations and Injection Well Site Selection, Paradox Valley Unit, Colorado: Bureau of Reclamation, 62 p.

Block, L.V., and Wood, C.K., 2010, Evolving characteristics of seismicity induced by long-term fluid injection at Paradox Valley, Colorado, American Geophysical Union Fall Meeting abstract #S13B-2000.

Block, L.V., Wood, C.K., Yeck, W.L., and King, V.M., 2014, The 24 January 2013 ML 4.4 Earthquake near Paradox, Colorado, and Its Relation to Deep Well Injection: Seismological Research Letters, v. 85, no. 3, p. 609-624.

Block, L.V., Wood, C.K., Yeck, W.L., and King, V.M., 2015, Induced seismicity constraints on subsurface geological structure, Paradox Valley, Colorado: Geophysical Journal International, v. 200, no. 2, p. 1170-1193.

Boore, D.M., and Atkinson, G.M., 2008, Ground-Motion Prediction Equations for the Average Horizontal Component of PGA, PGV, and 5%-Damped PSA at Spectral Periods between 0.01 s and 10.0 s: Earthquake Spectra, v. 24, no. 1, p. 99-138.

Bremkamp, W., and Harr, C.L., 1988, Area of Least Resistance to Fluid Movement and Pressure Rise, 49 p. p.

Brune, J.N., 1970, Tectonic Stress and the Spectra of Seismic Shear Waves from Earthquakes: J. Geophys. Res., v. 75, no. 26, p. 4997-5009.

Brune, J.N., 1971, Correction [to “Tectonic stress and the spectra, of seismic shear waves from earthquakes”]: Journal of Geophysical Research, v. 76, no. 20, p. 5002-5002.

Campbell, K.W., and Bozorgnia, Y., 1987, Campbell-Bozorgnia NGA Ground Motion Relations for the Geometric Mean Horizontal Component of Peak and Spectral Ground Motion Parameters: Pacific Earthquake Engineering Research Center, University of California UCB/PEER 2007/02 [Technical report through June 2006].

Campbell, K.W., and Bozorgnia, Y., 2008, NGA Ground Motion Model for the Geometric Mean Horizontal Component of PGA, PGV, PGD and 5% Damped Linear Elastic Response Spectra for Periods Ranging from 0.01 to 10 s: Earthquake Spectra, v. 24, no. 1, p. 139-171.

Chiou, B.S.J., and Youngs, R.R., 2008, An NGA Model for the Average Horizontal Component of Peak Ground Motion and Response Spectra: Earthquake Spectra, v. 24, no. 1, p. 173-215.

Chung, D.H., and Bernreuter, D.L., 1981, Regional relationships among earthquake magnitude scales: Reviews of Geophysics and Space Physics, v. 19, no. 4, p. 649-663.

Convertito, V., Maercklin, N., Sharma, N., and Zollo, A., 2012, From Induced Seismicity to Direct Time-Dependent Seismic Hazard: Bulletin of the Seismological Society of America, v. 102, no. 6, p. 2563-2573.

Cornell, C.A., 1968, Engineering seismic risk analysis: Bulletin of the Seismological Society of America, v. 58, no. 5, p. 1583-1606.

Cornell, C.A., and Vanmarcke, E.H., 1969, The Major Influences on Seismic Risk, in Proceedings of the 4th World Conference on Earthquake Engineering, Santiago, Chile, p. 69-83.

Cox, D.O., Stinson, S.H., and Stellavato, J.N., 2000, Well Testing in Ultra-High Permeability Formations, SPE Annual Technical Conference and Exhibition: Dallas, Texas, Copyright 2000, Society of Petroleum Engineers Inc.

Detournay, E., and Cheng, A.H.-D., 1993, Fundamentals of Poroelasticity, *in* Fairhurst, C., ed., Comprehensive Rock Engineering: Principles, Practice and Projects, Vol. II, Analysis and Design Method: Pergamon Press, p. 113-171.

Ellsworth, W.L., 2003, Magnitude and Area Data for Strike Slip Earthquakes, Working Group on California Earthquake Probabilities, Earthquake probabilities in the San Francisco Bay region - 2002-2031, U.S. Geological Survey Open-file Report 03-214: U.S. Geological Survey, p. 6.

Envirocorp Services and Technology Inc., 1995, Report of Evaluation of Injection Testing for Paradox Valley Injection Test No. 1: Durango, CO, Bureau of Reclamation, p. 67 p.

Fekete, 2012, WellTest User Manual (7.6.0 ed.): Calgary, Fekete Associates Inc.

Frohlich, C., 1989, The Nature of Deep-Focus Earthquakes: Annual Review of Earth and Planetary Sciences, v. 17, no. 1, p. 227-254.

Frohlich, C., and Davis, S.D., 1993, Teleseismic b values; Or, much ado about 1.0: Journal of Geophysical Research: Solid Earth, v. 98, no. B1, p. 631-644.

Garagash, D.I., and Germanovich, L.N., 2012, Nucleation and arrest of dynamic slip on a pressurized fault: Journal of Geophysical Research: Solid Earth, v. 117, no. B10, p. 27 pps.

Goertz-Allmann, B.P., Goertz, A., and Wiemer, S., 2011, Stress drop variations of induced earthquakes at the Basel geothermal site: Geophysical Research Letters, v. 38, no. 9, p. L09308.

Gutenberg, B., and Richter, C.F., 1954, Seismicity of the Earth and Associated Phenomena (2nd ed.): Princeton, New Jersey, Princeton University Press, 310 p.

Hanks, T.C., and Bakun, W.H., 2002, A bilinear source-scaling model for M-log A observations of continental earthquakes: Bulletin of the Seismological Society of America, v. 92, no. 5, p. 1841-1846.

Hanks, T.C., and Kanamori, H., 1979, A moment magnitude scale: Journal of Geophysical Research: Solid Earth, v. 84, no. B5, p. 2348-2350.

Harr, C., 1989, Proposed Location for Injection Well No. 2: Grand Junction, CO, Bureau of Reclamation, p. 33 p.

Horner, D.R., 1951, Pressure Build-up in Wells, 3rd World Petroleum Congress: The Hague, Netherlands, World Petroleum Congress, p. 25-43.

Jaeger, J.C., 1969, Elasticity, Fracture and Flow with Engineering and Geological Applications (Third ed.): London, Chapman & Hall, 268 p.

Jahr, T., Jentzsch, G., Gebauer, A., and Lau, T., 2008, Deformation, seismicity, and fluids: Results of the 2004/ 2005 water injection experiment at the KTB/ Germany: Journal of Geophysical Research, v. 113, no. B11, p.; Citation B11410.

Jahr, T., Jentzsch, G., Letz, H., and Gebauer, A., 2007, Tilt observations around the KTB-site, Germany; monitoring and modelling of fluid induced deformation of the upper crust of the Earth, *in* Tregoning, P., and Rizos, C., eds., Dynamic planet; monitoring and understanding a dynamic planet with geodetic and oceanographic tools.: Springer-Verlag. Berlin - Heidelberg, Federal Republic of Germany. 2007.

Kaklamanos, J., Baise, L.G., and Boore, D.M., 2011, Estimating Unknown Input Parameters when Implementing the NGA Ground-Motion Prediction Equations in Engineering Practice: Earthquake Spectra, v. 27, no. 4, p. 1219-1235.

Kanamori, H., and Anderson, D.L., 1975, Theoretical basis of some empirical relations in seismology: Bulletin of the Seismological Society of America, v. 65, no. 5, p. 1073-1095.

Keranen, K.M., Savage, H.M., Abers, G.A., and Cochran, E.S., 2013, Potentially induced earthquakes in Oklahoma, USA: Links between wastewater injection and the 2011 Mw 5.7 earthquake sequence: Geology.

Kharaka, Y.K., Ambats, G., Thordsen, J.J., and Davis, R.A., 1997, Deep well injection of brine from Paradox Valley, Colorado; potential major precipitation problems remediated by nanofiltration: Water Resources Research, v. 33, no. 5, p. 1013-1020.

King, V., Block, L., Yeck, W., Wood, C., and Derouin, S., submitted, Geological Structure of the Paradox Valley Region, Colorado, and Relationship to Seismicity Induced by Deep Well Injection: Journal of Geophysical Research: Solid Earth.

King, V.M., Block, L.V., Yeck, W.L., Wood, C.K., and Derouin, S.A., 2014, Geological structure of the Paradox Valley Region, Colorado, and relationship to seismicity induced by deep well injection: Journal of Geophysical Research: Solid Earth, v. 119, no. 6, p. 4955-4978.

Lee, S.H., and Ghassemi, A., 2010, A Three-Dimensional Thermo-Poro-Mechanical Finite Element Analysis of a Wellbore On Damage Evolution, 44th U.S. Rock Mechanics Symposium and 5th U.S.-Canada Rock Mechanics Symposium: Salt Lake City, Utah, American Rock Mechanics Association.

Lee, S.H., and Ghassemi, A., 2011, Three-Dimensional Thermo-Poro-mechanical Modeling of Reservoir Stimulation and Induced Microseismicity in Geothermal Reservoir Stanford Geothermal Workshop.

Lee, W.H.K., and Stewart, S.W., 1981, Principles and Applications of Microearthquake networks: New York, Academic Press, v. Supplement 2.

Lei, X., Yu, G., Ma, S., Wen, X., and Wang, Q., 2008, Earthquakes induced by water injection at approximately 3 km depth within the Rongchang gas field, Chongqing, China: Journal of Geophysical Research, v. 113, no. B10, p.; Citation B10310.

Mahrer, K., Ake, J., O'Connell, D., and Block, L., 2004, 2003 Status Report - Paradox Valley Seismic Network, Paradox Valley Unit, Southwestern Colorado: Bureau of Reclamation Technical Memorandum No. D8330-2004-04, 126 p.

Mahrer, K., Block, L., and Wood, C., 2008, 2007 Status Report, Paradox Valley Seismic Network, Paradox Valley Project, Colorado: Bureau of Reclamation, 96 p.

Majer, E., Nelson, J., Robertson-Tait, A., Savy, J., and Wong, I., 2012, Protocol for Addressing Induced Seismicity Associated with Enhanced Geothermal Systems: U. S. Department of Energy Geothermal Technologies Program, 46 p.

Marzocchi, W., and Sandri, L., 2003, A review and new insights on the estimation of the b-value and its uncertainty: Annals of Geophysics, v. 46, no. 6, p. 1271-1282.

McClure, M., and Horne, R., 2012, The Effect of Fault Zone Development on Induced Seismicity in Stanford Geothermal Workshop.

McGarr, A., 1976, Seismic moments and volume changes: Journal of Geophysical Research, v. 81, no. 8, p. 1487-1494.

McGarr, A., Simpson, D., and Seeber, L., 2002, Case histories of induced and triggered seismicity, *in* William H.K. Lee, H.K.P.C.J., and Carl, K., eds., International Geophysics: Academic Press, p. 647-661.

Mena, B., Wiemer, S., and Bachmann, C., 2013, Building Robust Models to Forecast the Induced Seismicity Related to Geothermal Reservoir Enhancement: Bulletin of the Seismological Society of America, v. 103, no. 1, p. 383-393.

Molnar, P., 1979, Earthquake recurrence intervals and plate tectonics: Bulletin of the Seismological Society of America, v. 69, no. 1, p. 115-133.

Nicholls, H.R., Johnson, C.F., and Duvall, W.I., 1971, Blasting Vibrations and Their Effects on Structures: U. S. Department of the Interior, Office of Surface Mining, Reclamation and Enforcement, 110 p.

Nicol, A., Carne, R., Gerstenberger, M., and Christophersen, A., 2011, Induced seismicity and its implications for CO2 storage risk: Energy Procedia, v. 4, no. 0, p. 3699-3706.

Power, M., Chiou, B., Abrahamson, N., Bozorgnia, Y., Shantz, T., and Roblee, C., 2008, An Overview of the NGA Project: Earthquake Spectra, v. 24, no. 1, p. 3-21.

Richter, C.F., 1935, An instrumental earthquake magnitude scale: Bulletin of the Seismological Society of America, v. 25, no. 1, p. 1-32.

Roeloffs, E., and Denlinger, R., 2009, An Axisymmetric Coupled Flow and Deformation Model for Pore Pressure Caused by Brine Injection in Paradox Valley, Colorado: Implications for the Mechanisms of Induced Seismicity, Preliminary Peport to the Bureau of Reclamation: U.S. Geological Survey, 31 p.

Shapiro, S.A., and Dinske, C., 2009, Scaling of seismicity induced by nonlinear fluid-rock interaction: Journal of Geophysical Research: Solid Earth, v. 114, no. B9, p. B09307.

Shapiro, S.A., Dinske, C., and Kummerow, J., 2007, Probability of a given-magnitude earthquake induced by a fluid injection: Geophysical Research Letters, v. 34, no. 22, p.; L22314.

Shapiro, S.A., Dinske, C., Langenbruch, C., and Wenzel, F., 2010, Seismogenic index and magnitude probability of earthquakes induced during reservoir fluid stimulations: The Leading Edge, v. 29, no. 3, p. 304-309.

Shapiro, S.A., Huenges, E., and Borm, G., 1997, Estimating the crust permeability from fluid-injection-induced seismic emission at the KTB site: Geophysical Journal International, v. 131, no. 2, p. 15-18.

Shapiro, S.A., Krüger, O.S., Dinske, C., and Langenbruch, C., 2011, Magnitudes of induced earthquakes and geometric scales of fluid-stimulated rock volumes: Geophysics, v. 76, no. 6, p. WC55-WC63.

Shapiro, S.A., Patzig, R., Rothert, E., and Rindschwentner, J., 2003, Triggering of Seismicity by Pore-pressure Perturbations: Permeability-related Signatures of the Phenomenon: Pure and Applied Geophysics, v. 160, no. 5-6, p. 1051-1066.

Shapiro, S.A., Rentsch, S., and Rothert, E., 2005, Characterization of hydraulic properties of rocks using probability of fluid-induced microearthquakes: Geophysics, v. 70, no. 2, p. F27-F33.

Shapiro, S.A., Rothert, E., Rath, V., and Rindschwentner, J., 2002, Characterization of fluid transport properties of reservoirs using induced microseismicity, *in* Shapiro Serge, A., and Gurevich, B., eds., Seismic signatures of fluid transport.: Society of Exploration Geophysicists. Tulsa, OK, United States. 2002.

Shaw, B.E., 2009, Constant Stress Drop from Small to Great Earthquakes in Magnitude-Area Scaling: Bulletin of the Seismological Society of America, v. 99, no. 2A, p. 871-875.

Shi, Y., and Bolt, B.A., 1982, The standard error of the magnitude-frequency b value: Bulletin of the Seismological Society of America, v. 72, no. 5, p. 1677-1687.

Siskind, D.E., Stagg, M.S., Kopp, J.W., and Dowding, C.H., 1980, Structure Response and Damage Produced by Ground Vibration From Surface Mine Blasting: U. S. Department of the Interior, Office of Surface Mining, Reclamation and Enforcement, 83 p.

Subsurface Technology, 2001, Report of Operations: Houston, no. 60D5207, p. 24 p. .

Tinti, S., and Mulargia, F., 1987, Confidence intervals of b values for grouped magnitudes: Bulletin of the Seismological Society of America, v. 77, no. 6, p. 2125-2134.

Utsu, T., 1966, A Statistical Significance Test of the Difference in b-value between Two Earthquake Groups: Journal of Physics of the Earth, v. 14, no. 2, p. 37-40.

Wang, H., 2000, Theory of linear poroelasticity with applications to geomechanics and hydrogeology: Princeton, NJ, Princeton University Press.

Wang, X., and Ghassemi, A., 2012, A 3 D Thermal-poroelastic Model for Geothermal Reservoir Stimulation, Stanford Geothermal Workshop.

Wang, Y.C., 2008, Discrete element simulation of hydraulic fracturing and induced seismicity in engineered geothermal systems, *in* Gurgenci, H., and Budd, A., eds., Proceedings of the Sir Mark Oliphant international frontiers of science and technology Australian geothermal energy conference.: Geoscience Australia. Canberra, A.C.T., Australia. 2008.

Wells, D.L., and Coppersmith, K.J., 1994, New empirical relationships among magnitude, rupture length, rupture width, rupture area, and surface displacement: Bulletin of the Seismological Society of America, v. 84, no. 4, p. 974-1002.

Yeck, W.L., Block, L.V., Wood, C.K., and King, V.M., 2014, Maximum magnitude estimations of induced earthquakes at Paradox Valley, Colorado, from cumulative injection volume and geometry of seismicity clusters: Geophysical Journal International, v. 200, no. 1, p. 322-336.

Appendix A Earthquake Catalog

The earthquake catalog used for the analyses presented in this report is provided in the attached file “TM 86-68330-2013-12 earthquake catalog.csv”. This comma-delimited ascii file contains a catalog of earthquakes that occurred within approximately 10 km of the perimeter of the Paradox Valley Seismic Network (PVSN) from 1985 through July, 2013 (Figure A-1). The earthquakes were detected and their locations computed primarily using data from PVSN. Data from the nearby Ridgway Seismic Network, also operated by Reclamation, supplemented the PVSN data for some of the events that occurred from 1985 to 2007. Identified explosions are excluded from the catalog.

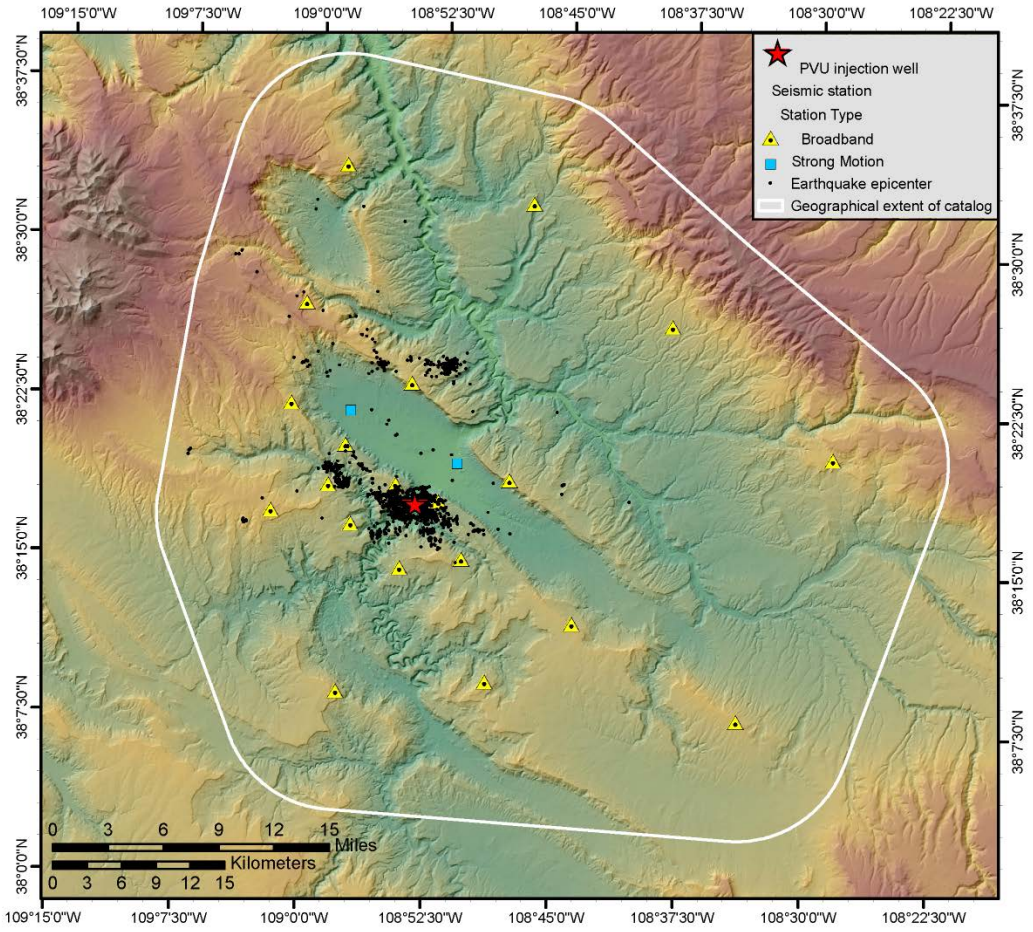

Figure A-1. Geographical extent of PVSN earthquake catalog.

A.1 Earthquake Location Methods

This catalog contains one hypocenter for each earthquake. The hypocenter was computed using either a relative event location procedure or an absolute event location method. The following description of the event location methods is taken from Block et al. (2015):

> We calculate two sets of hypocenters from the PVSN data. Initially, we compute absolute earthquake locations using manually-determined P-wave and S-wave arrival times. These hypocenters are computed using three-dimensional (3-D) P-wave and S-wave velocity models developed from hypocenter-velocity-station correction inversions of data from naturally-occurring and induced local earthquakes and explosions recorded by PVSN. Both the hypocenter-velocity inversion and earthquake location software we use were developed in-house and represent an extension of the work of Block (1991). We subsequently compute precise relative event locations from inversion of arrival time differences obtained from cross-correlations of P-wave and S-wave arrivals extracted from waveforms recorded at the same station for pairs of events. No time differences from manual time picks are included, with the exception of data from the five events with magnitude of 3.5 or greater. Because most of the waveforms for these events are clipped but many of the first breaks are clear, we incorporate them into the event relative location using differences of high-quality manually picked arrival times.
>
> For the relative location inversion, we use a double-difference-type algorithm. The 3-D velocity models described above are used and remain fixed during the relative location inversion. No event clustering is performed, so an event may tie to any other event in the dataset. Data from event pairs with small separation distances are weighted most strongly in the inversion; data from event pairs with larger separation distances (as a fraction of the event-to-station distance) are down-weighted or eliminated from the inversion to reduce potential bias from unmodeled velocity variations in the source regions. Because the absolute earthquake locations are not well-constrained by the time difference data alone, we keep the locations of a few widely-spaced (> ~3 km apart) events with well-constrained absolute locations fixed during the relative location inversion. An earthquake must tie, either directly or indirectly (possibly through multiple event pairs), to an event with a fixed location to be retained in the relative location inversion.
>
> Approximately 87% of all induced earthquakes and 93% of induced earthquakes with duration magnitude (M_D) ≥ 0 occurring within 10 km of the PVU injection well are considered well-constrained in the relative location inversion. We assign these hypocenters a quality factor of ‘a’. For the remaining events, we retain the absolute locations and assign a hypocenter quality factor of ‘b’.

Both the absolute and relative location uncertainties affect the reliability of the seismicity patterns produced. When considering the relative locations of widely spaced earthquakes, the absolute location uncertainties of the events fixed during the hypocenter relative location are the most important factor. The standard errors of the absolute locations of these fixed events vary from 50 to 100 meters horizontally and 70 to 150 meters vertically. When considering the spatial distribution of closely spaced events (< ~ 3 km apart), the relative location uncertainties control the spatial resolution of the hypocenter patterns. Preliminary analysis of the relative location errors indicates that the error of an individual earthquake with respect to all other tied events is generally less than 50 meters horizontally and 100 meters vertically. Relative location errors of earthquakes in close proximity to each other are likely less, but a detailed analysis of the relative location errors as a function of event separation distance is still in progress. The absolute errors of the events that do not tie into the relative location procedure (the b-quality events) have significantly higher errors, with average standard errors of approximately 500 meters horizontally and 800 meters vertically.

A.2 Description of Data Columns

The earthquake catalog file contains the following columns:

Event_ID: Identification number of event

Year: Earthquake origin time year
Month: Earthquake origin time month
Day: Earthquake origin time day
Hour: Earthquake origin time hour
Minute: Earthquake origin time minute
Second: Earthquake origin time second

Latitude_(deg): Hypocenter latitude in decimal degrees North.
Longitude_(deg): Hypocenter longitude in decimal degrees; negative values are West
Elevation_(m): Hypocenter elevation in meters with respect to mean sea level

Magnitude: Earthquake magnitude.
Magnitude_type: Type of magnitude calculation. Magnitudes < **M** 3.5 are duration magnitudes (MD). Magnitudes ≥ **M** 3.5 are local magnitudes (ML).
Magnitude_source: Organization that computed the magnitude. Duration magnitudes were computed by the Bureau of Reclamation (USBR). Local magnitudes were obtained from the U.S. Geological Survey (USGS) or the University of Utah Seismograph Stations (UUSS).

Quality: Indicates whether the hypocenter was computed with a relative location method (quality = ‘a’) or an absolute location method (quality=’b’)

RMS_residual_(s): Root-mean-square (rms) time residual in seconds. For b-quality events, this is the rms of the absolute time residuals. For a-quality events, this is the rms of the time difference residuals.
Nabstimes: Number of arrival times used to compute the absolute location of b-quality events. (Zero for a-quality events.)
Neventpairs: Number of event pairs providing time differences for the relative location of a-quality events. (Zero for b-quality events.)
Ntimediffs: Number of time differences used to compute the relative location of a-quality events. (Zero for b-quality events.)
Nstations: Number of stations providing data for the hypocenter calculations, either in terms of absolute arrival times (for b-quality events) or time differences (for a-quality events).
Maxgap_(deg): Maximum azimuthal gap in ray coverage to the nearest integer degree. For the event relative location (a-quality events), this considers data for all event pairs.
Min_dist/depth: Horizontal distance to the closest seismic station providing data for the hypocenter calculation divided by the focal depth.

Focal_mechanism_category: Focal mechanism category for the events near the January 2013 M_L 4.4 earthquake for which focal mechanisms were analyzed, as described in section 2.4. Categories are: ‘1’ for strike-slip focal mechanisms, ‘2’ for oblique normal focal mechanisms, and ‘0’ for events not analyzed.

References:

Block, L.V., 1991. Joint hypocenter-velocity inversion of local earthquake arrival time data in two geothermal regions, Ph.D., Massachusetts Institute of Technology, Cambridge, MA.

Block, L.V., C. K. Wood, W. L. Yeck, and V. M. King, 2015, Induced seismicity constraints on subsurface geological structure, Paradox Valley, Colorado, *Geophysical Journal International*, 200, 1172-1195.